

August 2017

The Formation and Dynamics of Clouds in the Environment of Active Galactic Nuclei

Timothy Waters

University of Nevada, Las Vegas, waters@lanl.gov

Follow this and additional works at: <https://digitalscholarship.unlv.edu/thesesdissertations>



Part of the [Astrophysics and Astronomy Commons](#), and the [Physics Commons](#)

Repository Citation

Waters, Timothy, "The Formation and Dynamics of Clouds in the Environment of Active Galactic Nuclei" (2017). *UNLV Theses, Dissertations, Professional Papers, and Capstones*. 3106.

<https://digitalscholarship.unlv.edu/thesesdissertations/3106>

This Dissertation is protected by copyright and/or related rights. It has been brought to you by Digital Scholarship@UNLV with permission from the rights-holder(s). You are free to use this Dissertation in any way that is permitted by the copyright and related rights legislation that applies to your use. For other uses you need to obtain permission from the rights-holder(s) directly, unless additional rights are indicated by a Creative Commons license in the record and/or on the work itself.

This Dissertation has been accepted for inclusion in UNLV Theses, Dissertations, Professional Papers, and Capstones by an authorized administrator of Digital Scholarship@UNLV. For more information, please contact digitalscholarship@unlv.edu.

THE FORMATION AND DYNAMICS OF CLOUDS
IN THE ENVIRONMENT OF ACTIVE GALACTIC NUCLEI

By

Timothy R. Waters

Bachelor of Arts - Physics
Occidental College, Los Angeles
2006

Master of Science - Applied Mathematics
University of Nevada, Las Vegas
2009

Master of Science - Physics
University of Nevada, Las Vegas
2012

A dissertation submitted in partial fulfillment
of the requirements for the

Doctor of Philosophy - Physics

Department of Physics and Astronomy
College of Sciences
The Graduate College

University of Nevada, Las Vegas
August 2017



Dissertation Approval

The Graduate College
The University of Nevada, Las Vegas

August 18, 2017

This dissertation prepared by

Timothy R. Waters

entitled

The Formation and Dynamics of Clouds in The Environment of Active Galactic Nuclei

is approved in partial fulfillment of the requirements for the degree of

Doctor of Philosophy - Physics
Department of Physics and Astronomy

Daniel Proga, Ph.D.
Examination Committee Chair

Kathryn Hausbeck Korgan, Ph.D.
Graduate College Interim Dean

Bing Zhang, Ph.D.
Examination Committee Member

Stephen Lepp, Ph.D.
Examination Committee Member

Darrell Pepper, Ph.D.
Graduate College Faculty Representative

ABSTRACT

Active galactic nuclei (AGN) are among the most luminous objects in the universe and are known to be powered by accretion onto supermassive black holes in the centers of galaxies. AGN clouds are prominent components of successful models that attempt to unify the diversity of AGN. These clouds are often hypothesized to be the source of the broad and narrow line emission features seen in AGN spectra. Moreover, the high column densities of gas needed to account for broad absorption lines has been attributed to the same population of clouds, while the motion of AGN clouds has been invoked to explain the spectral variability observed in both broad absorption lines and warm absorbers.

Despite the importance of AGN clouds for explaining phenomena associated with AGN, we still lack a comprehensive understanding of the origin, dynamics, lifetime, and properties of these clouds. This thesis is an attempt to lay the groundwork for such a comprehensive model. After summarizing the known physics of AGN clouds and our modeling framework (i.e. the equations of hydrodynamics), we review the linear theory of the thermal instability (TI), which provides a natural mechanism to form clouds. We then extend this theory of cloud formation to account for the role of cloud acceleration, which must accompany the nonlinear regime of TI. After presenting hydrodynamical simulations that demonstrate how cloud formation and acceleration are intertwined processes, we explore how the efficiency of cloud acceleration is affected by the inclusion of flux variability. We find that the acceleration can more than double when the period of flux oscillations is longer than the thermal timescale of the gas. Next we calculate synthetic absorption line profiles to determine how clouds evolving along the line of sight would appear to a distant observer. We identify a spectral signature for cloud acceleration in the case of absorption line doublets. Finally, we show how global hydrodynamical simulations can be used to make predictions for the observables obtainable from reverberation mapping campaigns. We conclude with a summary of our findings and the next steps needed to further develop a comprehensive model of AGN clouds.

ACKNOWLEDGMENTS

This PhD would not have been possible without the guidance and expertise of my advisor, mentor, and friend, Daniel Proga. Besides an espresso addiction, I have acquired from Daniel most of my knowledge of hydrodynamics, a passion for AGN research, and a new outlook on science in general. His encouragement and optimism allowed me to become a researcher at a time in my life when I had almost given up on that dream. It is an honor to have him as my academic father, and I look forward to more fruitful collaborations together.

Daniel's past and present group members that I overlapped with have made a lasting impression on me. Monika Mościbrodzka and Ryuichi Kurosawa are role models and interactions with them motivated me to work harder. Nick Higginbottom's programming style taught me how fun it can be to read other people's code. Stefan Luketic was instrumental in testing my dedication to the pursuit of a research career in astrophysics. Sergei Dyda quickly became my friend and colleague. His innocent curiosity and enthusiasm for physics have helped me to think deeper, while his sense of humor kept me afloat the last couple of years. Last but not least, I am lucky to call Randall Dannen, who will now take my place as the senior graduate student, a friend and collaborator who I look forward to working and sharing some good laughs with in the future.

I also thank Daniel for sending me to many conferences — both domestic and international — as well as to Princeton, where Jim Stone graciously hosted me and let me present my first results on cloud dynamics to his group.

I've spent three summers now working at Los Alamos National Laboratory (LANL), each of them a great learning experience. I thank Sean Fu for coming up with an interesting introductory plasma physics project in the summer of 2014. Little did I know that he and his family would be neighbors and help raise my daughter a couple years later. I thank Wes Even, Brandon Wiggins, and Chris Fryer for mentoring me in the summer of 2015. And this summer I owe a debt of thanks to Josh Dolence for his mentorship, for giving me the opportunity to learn GRMHD, and for helping me secure a postdoc at LANL.

Much needed self-reflection arose out of many conversations with my good friend, Greg Colarch, especially those over a bowl of pho and a cup of boba. Greg and I began our graduate physics training in the Fall of 2009, each of us ended up with two Master's degrees we probably didn't need, and when life got in the way, we both managed to reassure each other that we'd be content without a

PhD in physics. And yet we endured.

The UNLV physics and astronomy department has been very supportive over the years. I thank Bernard Zygelman for being an excellent instructor, as he taught most of my graduate level physics classes. I especially thank Bing Zhang and Ken Nagamine for doing their best to teach me astronomy. I'm indebted to the newest astronomy faculty member, Zhaohuan Zhu, for helping me learn the new ATHENA++ code and putting in a good word for me at LANL. Jay Nietling deserves a special thanks for giving me the opportunity to learn some web programming and redo the department website. I was honored to receive a commemorative edition of the Feynman Lectures on Physics after finishing the site, for which I'm sure I also owe thanks to the department chair, Stephen Lepp. It was a pleasure getting to know Eunja Kim, with whom I shared many Allegiant and Southwest flights between Las Vegas and Albuquerque the past couple years, as well as Natasa Korceba, who never seems to lack kind words and helpful advice. Finally, I value the continued friendship and support of my colleague John Boisvert and his longtime girlfriend Mariela Preciado, as well as that of my colleague Jeremy Smallwood.

My best friend, confidant, and the mother of my children — my wife Jiajia — has sacrificed a lot for this PhD, as we have been living in separate cities for the past two years and my state of mind was often a state of grief when we were together. I thank her for many things, not least of all her strength and understanding, as well as for her mastery of advanced calculus and numerical methods, which I benefitted from more than once.

Above all, I must acknowledge the love, support, and advice of my mother, who I wish could have lived to see me complete my PhD. Her name, Nancy, means 'grace', and so I needed to look no further for a name for my daughter. My mother would have been overjoyed to know that Grace bears an uncanny resemblance to her, and that she has a grandson on the way.

In memory of my mother,
Nancy L. Andersen
May 14, 1948 - June 17, 2015

TABLE OF CONTENTS

ABSTRACT	iii
ACKNOWLEDGMENTS	iv
LIST OF FIGURES	xii
Chapter 1 INTRODUCTION.	1
1.1 AGN classification and unification	3
1.2 The supermassive black hole paradigm	4
1.2.1 Accretion power	4
1.2.2 Broad and narrow line regions	5
1.2.3 The mass budget	6
1.3 The debated origins of AGN line emission/absorption	7
1.3.1 Problems with pressure confined clouds	8
1.3.2 The inadequacy of accretion disks	9
1.3.3 The plausibility of accretion disk winds	9
1.3.4 Persistent notions of discrete clouds	10
1.3.5 Clouds + winds = clumpy winds	11
1.4 AGN clouds: theoretical background	12
1.4.1 Thermal instability criteria	12
1.4.2 Understanding cloud formation	13
1.4.3 Equilibria and evaporation of static AGN clouds	15
1.4.4 Destruction of accelerated AGN clouds	17
1.5 Thesis summary	18
Chapter 2 THE EQUATIONS OF GAS DYNAMICS	20
2.1 Newtonian equations of hydrodynamics	22

2.1.1	Mass conservation	22
2.1.2	Momentum conservation	23
2.1.3	Energy conservation	25
2.1.4	Equation of state	27
2.1.5	Entropy generation	29
2.1.6	Vorticity generation	30
2.1.7	Eulerian equations summarized	31
2.2	Gas dynamics of clouds: simple examples	32
2.2.1	A Parabolic PDE: cloud equilibria	32
2.2.2	A Hyperbolic PDE: cloud formation	33
2.2.3	An Elliptic PDE: cloud evaporation	34
2.2.4	Summary	36
Chapter 3 RADIATION SOURCE TERMS		37
3.1	Derivation using radiative transfer theory	37
3.1.1	Radiation moment equations	38
3.1.2	The body force due to radiation	40
3.1.3	Heating and cooling term	41
3.2	Sources of opacity	42
3.2.1	Free-free	42
3.2.2	Bound-free	43
3.2.3	Bound-bound	43
Chapter 4 LINEAR THEORY		44
4.1	Eulerian perturbations	45
4.2	Lagrangian perturbations	46
4.3	Informal Lagrangian analysis of TI	48
4.4	Formal Eulerian analysis of TI	49
4.4.1	Dispersion relation in a stationary medium	52

4.4.2	Instability criteria	53
4.4.3	Recovering Balbus' and Field's criterion	54
4.4.4	Generalized stability criterion	55
4.4.5	Dispersion relation in a uniformly moving medium	56
4.5	Numerical simulations of TI	56
4.5.1	Initial conditions for cloud simulations	56
4.5.2	Cloud tracking and a bound for the density perturbation	58
Chapter 5	CLOUD FORMATION AND ACCELERATION	60
5.1	Theory and expectations	61
5.2	Governing equations	63
5.3	Methods and results	64
5.3.1	Initial and boundary conditions	65
5.3.2	Simulations	66
5.3.3	Results of 1-D Simulations	68
5.3.4	Results of 2-D Simulations	69
5.4	Discussion	74
Chapter 6	EFFECTS OF FLUX VARIABILITY	77
6.1	Introduction	77
6.2	Methods	77
6.3	Results	80
6.3.1	1D Simulations	80
6.3.2	2D Simulations	82
6.4	Discussion	84
Chapter 7	SYNTHETIC ABSORPTION LINES AND A SPECTRAL SIGNATURE FOR CLOUD ACCELERATION	86
7.1	Introduction	86
7.2	Methods	87
7.2.1	Hydrodynamical simulations	87

7.2.2	Photoionization calculations	88
7.2.3	Absorption line profiles	91
7.2.4	Doublet lines and the PPC model	92
7.3	Results	93
7.3.1	Synthetic absorption lines	95
7.3.2	A spectral diagnostic for cloud acceleration	101
7.3.3	Partial covering analysis	103
7.3.4	Line profile variability	104
7.4	Discussion	105
7.5	Conclusions	108
Chapter 8	APPLICATION TO REVERBERATION MAPPING	110
8.1	Introduction	110
8.2	Formalism	111
8.2.1	Derivation of the impulse response function	111
8.2.2	Responsivity and opacity distributions	114
8.2.3	The escape probability	117
8.2.4	The resonance condition	118
8.2.5	Echo image sketches	120
8.2.6	Transfer functions and line profiles	121
8.3	Methods	121
8.3.1	Formal evaluation of the impulse response function	122
8.3.2	Numerical evaluation of the impulse response function	123
8.3.3	Direct vs. indirect calculation of the transfer function and line profile	124
8.3.4	Incorporating photoionization modeling results and accounting for time-dependent effects	125
8.4	Example calculation: the Chiang & Murray disk wind solution	126
Chapter 9	CONCLUSIONS	130

Appendix A EXPRESSIONS FOR HEATING AND COOLING134
Appendix B EXPRESSIONS FOR LINE DRIVING135
Appendix C A MODIFIED DOUBLET SOLUTION136
REFERENCES 138
CURRICULUM VITAE 146

LIST OF FIGURES

Figure	Page
1.1 A visualization of the Virgo Supercluster, showing two famous active galaxies in relation to The Local Group.	2
1.2 Figure from Krolik et al. (1981) summarizing the formation mechanism of clouds via the nonlinear saturation of the thermal instability.	14
1.3 Schematic of both a large and small AGN cloud, depicting the physics taking place in cloud interfaces (yellow layer).	15
1.4 Figure 1 from Proga et al. 2014.	17
4.1 Analytic plane-wave solutions of the linearized equations of gas dynamics.	44
5.1 Temperature and opacity dependence on the photoionization parameter expected in an AGN environment.	62
5.2 Profiles of run RFLDX in 1-D at time $120 t_{sc}$	67
5.3 Comparison of all runs in 1-D and 2-D.	70
5.4 Density snapshots of run RFLDX in 2-D in units of ρ_{eq}	71
5.5 Mass fractions for run RFLDX in 2-D at four different resolutions.	72
6.1 Temporal properties of 1D simulations.	78
6.2 Spatial profiles in the comoving frame of the cloud.	79
6.3 Same as Figure 6.1, but for 2D simulations run for 155 thermal times.	80
6.4 Density maps of our 2D runs.	83
7.1 Illustrative calculation of the optical depth at line center, $\tau_{\nu_0}(x)$	94
7.2 Density maps and corresponding synthetic absorption line profiles for a constant flux run (first row of panels) and a variable flux run (second row of panels).	96

7.3	Same as Figure 7.2 but for the slab geometry.	97
7.4	Temporal analysis linking cloud acceleration with the expected absorption properties.	98
7.5	Method to calculate representative values of τ_ν and C_ν in order to assess the PPC model.	99
7.6	Comparison between the doublet solution of the PPC model (thick black curves) and the exact solutions for τ_ν (top panel) and C_ν (middle panel).	100
8.1	Echo image sketches of the PK04 solution.	119
8.2	A benchmark calculation using the analytic solution from CM96.	127
9.1	SEDs of Type I and Type II AGN, solid blue and dashed green line, respectively.	133
C.1	Modified doublet solutions.	137

Chapter 1

INTRODUCTION

Active galactic nuclei (AGN) are, as the name suggests, the central regions of active galaxies, with the qualifier ‘active’ serving to denote an abnormally large luminosity compared to the nuclei of typical galaxies. Astronomers have already detected on the order of 1 million high luminosity AGN (e.g., Richards et al. 2009). This seems like an enormous number for a seemingly rare phenomenon, until one realizes that there are about 200 billion galaxies that are currently observable in the universe, a figure which represents roughly 2% of the inferred total number (i.e. ~ 10 trillion; Conselice et al. 2016). An estimate based on the current surface density of observed AGN on the sky indicates that there are ~ 1 billion active galaxies (e.g., Padovani et al. 2017), thereby making the ratio of active to typical galaxies about 1%. The above high luminosity AGN tally, i.e. ~ 1 million in the SDSS catalog, therefore represents only 0.1% of the full population that can in principle be detected with current technology.

Nearby AGN¹ are considered those with redshift $z \lesssim 0.1$. For context, the closest galaxy to earth hosting an AGN is NGC 5128 and is about 4 megaparsecs (Mpc) away, with a redshift of $z \approx 0.002$. This is located in the Centaurus A galaxy group, one of the closest groups of galaxies outside of our local group. In other words, there are no AGN in our own local group, which is composed of mainly many small satellite galaxies to our own galaxy and its massive companion, Andromeda (a.k.a. M31), as well as many dwarf galaxies. To put these distances into perspective, Figure 1 shows a map of the Virgo Supercluster, of which our local group is a member. One of the most massive galaxies in our local universe is M87, a famous AGN 16.4 Mpc away in the center of the Virgo cluster that features a prominent relativistic jet extending 1.5 kpc beyond its nucleus. It is at a redshift of $z \approx 0.004$, while the brightest galaxy in the Fornax cluster, located 19 Mpc away, has a redshift much smaller than this due to its local motion toward us. Thus, we can roughly think of local AGN as those with $z \lesssim 0.01$, whereas ‘nearby’ AGN with $0.01 \lesssim z \lesssim 0.1$ are already in active galaxies at cosmological distances beyond our local supercluster of galaxies, where the concept of redshift becomes a useful distance indicator.

¹While the term ‘AGN’ refers specifically to the nuclei of galaxies, it is common to refer the entire galaxy as simply an AGN rather than an ‘active galaxy’, a practice that makes sense in cases where the host galaxy is unresolved.

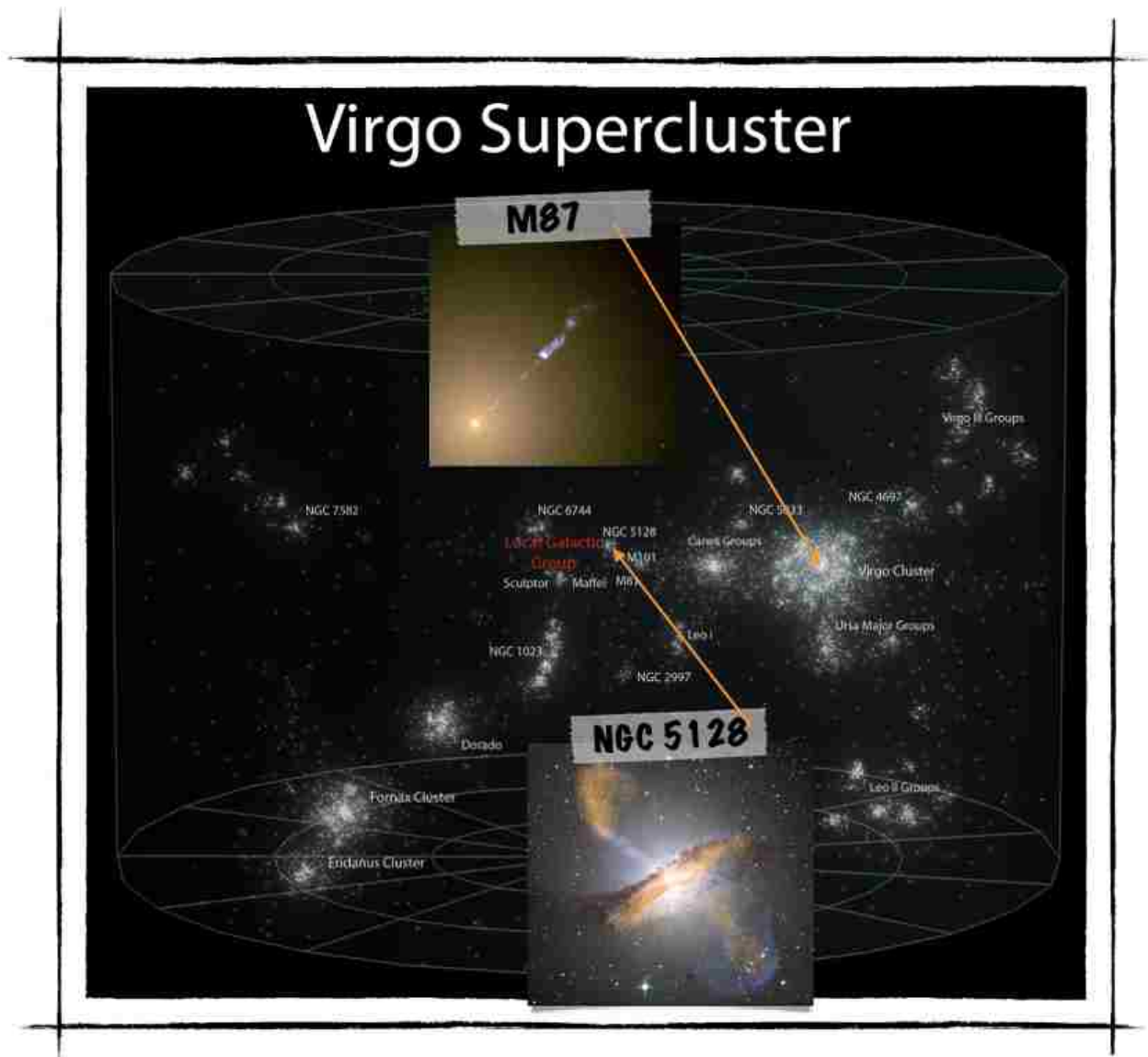


Figure 1.1: A visualization of the Virgo Supercluster, showing two famous active galaxies in relation to The Local Group. The nearest luminous AGN is NGC 5128, and M87 (a.k.a. NGC 4486) is the largest AGN (by volume) in the local universe. The image of NGC 5128 is a composite showing infrared data obtained from the Large APEX Bolometer Camera (LABOCA) in orange (APEX is an acronym for the Atacama Pathfinder Experiment), X-ray emission in blue (from the Chandra X-ray Observatory), and the rest is optical data in near true colors (from the ESO 2.2 m telescope in Chile). The image of M87 is an HST photograph. Image credits: Virgo Supercluster rendering from Wikimedia Commons user Andrew Z. Colvin; inset images taken from Wikipedia.

1.1 AGN classification and unification

The literature on AGN typically divides them into two main classes, either Seyfert galaxies or quasars. This division is based on both luminosity and distance, as almost all Seyfert galaxies are nearby AGN and have a low luminosity compared to quasars. While the name ‘quasar’ derives from the acronym QSO (for quasi stellar object), the term quasar is often used to denote an AGN that appears optically as a point source with no visible extended emission from the galaxy disk. ‘QSO’ is typically reserved to describe quasars that are radio faint, while the highly used designations of radio loud (RL) and radio quiet (RQ) apply to both quasars and Seyferts.

The other main division of AGN is based not on distance and luminosity but rather on spectral properties and luminosity. AGN are classified as either Type I or Type II based on an examination of the line widths of their emission lines, a comparison of the widths of forbidden lines to permitted lines, and the overall strength of various lines, as measured by the line equivalent width (EW). Type I AGN generally show very broad emission lines with FWHM at least $1,500 \text{ km s}^{-1}$ and up to about $10,000 \text{ km s}^{-1}$, while their forbidden lines are considerably more narrow, and they have relatively small EWs because these lines are seen against a strong background continuum. That is, compared to Type II AGN, Type I AGN are generally much more luminous, so the strength of the continuum is a factor in making this division. The spectra of Type II AGN generically lack broad emission lines and their forbidden and permitted lines have similar widths. Their EWs are larger than Type I AGN because, due to their overall lower luminosities, their emission lines stand out more against the background continuum.

The development orientation-based unification models (e.g., Antonucci, 1993; Urry & Padovani, 1995) represented a breakthrough in our understanding of AGN, as this provided a geometrical interpretation of the Type I/II division. Type I AGN present an unobscured view of the nucleus, i.e. are viewed nearly face on, while Type II AGN are viewed closer to edge on. These models also informed other classification schemes, as the RQ and RL designations only apply to Type I AGN, the interpretation being that the radio emission is associated with the base of a relativistic jet that is obscured in Type II AGN. Due to this physical association with the jet, Padovani (2017) has recently made a convincing plea to abandon the RL and RQ labels, replacing them with ‘jetted’ and ‘non-jetted’. The argument is that RL and RQ objects are intrinsically different, with RL AGN emitting a much larger fraction of energy as non-thermal emission arising from with the jet, whereas RQ AGN feature mostly thermal emission associated with the accretion disk.

There are many subclassifications used to group individual AGN appropriately, which is important for statistical studies of their properties. We will not describe the terminology used any further, referring instead to the many textbooks (e.g., Krolik 1999, Peterson 2000, Osterbrock & Ferland 2005, Beckmann & Shrader 2012, Netzer 2013) and reviews (e.g., Sulentic et al. 2000, Ho 2008, Netzer 2015, Padovani et al. 2017). It should be mentioned, however, that orientation-based unification models have evolved into weak/evolution-based unification models (e.g., Netzer 2015). Orientation-based unification relies on only two parameters to understand the observed classes of AGN: orientation and luminosity (i.e. accretion rate). In addition to these parameters, weak/evolution-based unification models attempt to supplement our physical understanding of AGN phenomena by incorporating new information from studies focusing on the absorption properties (i.e. the covering fraction is an important parameter), the merger history (i.e. redshift is an important parameter), and the time variability of AGN.

1.2 The supermassive black hole paradigm

While AGN are defined and classified based on observational criteria, there is a perfectly good physical definition: any galaxy containing an actively accreting supermassive black hole (SMBH) qualifies as an AGN (Netzer 2013). The modern paradigm is that all massive galaxies host central SMBHs, and moreover that most small galaxies — perhaps all of those that have bulges — also contain central SMBHs. There is even strong evidence that these galaxies and their black holes co-evolved, this conclusion accompanying the realization that the masses of SMBHs and the properties of their host galaxies are intimately related (e.g., Magorrian et al. 1998; Ferrarese & Merritt 2000; Gebhardt et al. 2000). The profound implication is that $\sim 99\%$ of typical galaxies, or whatever large percentage of them host a SMBH, do not accrete enough gas to become classified as ‘active’ galaxies. However, they in fact do accrete gas — one case in point is our own galactic center — but they do so in a decisively unspectacular fashion by appearing exceptionally dim. Such *low luminosity* AGN (LLAGN) likely constitute a rather large percentage of the galaxy population.

1.2.1 Accretion power

The dimness of LLAGN are counter to expectations based on classical thin disk accretion theory and this constitutes a luminosity deficit problem as noted by Fabian & Canizares (1988). To quote Ho (2008), “when quasars were first discovered, the challenge then was to explain their tremendous

luminosities. Ironically, more than four decades later, the problem has been reversed: the challenge now is to explain how dead quasars can remain so dormant.” This ‘luminosity paradox’ arises due to the enormous efficiency of the accretion process in converting gravitational potential energy into luminosity. Some fraction of the gravitational binding energy of gas accreting at a rate \dot{M} onto a SMBH will be radiated away. If \dot{M} can be inferred, a direct estimate of the AGN luminosity is

$$L_{\text{AGN}} = \eta \dot{M} c^2, \quad (1.1)$$

where η is the radiative efficiency, which is typically assumed to be about 10% but can be as high as 42% for maximally spinning black holes that convert all of their binding energy into radiation. Proposed resolutions to this paradox necessarily focus on how either η or \dot{M} can be exceptionally small in LLAGN (see Ho 2008 for a summary).

This thesis is focused on phenomena associated with luminous AGN, in which it is assumed that η does not vary dramatically from source to source, the diversity of AGN instead being mainly attributable to \dot{M} , orientation effects, and the other parameters discussed above. The physical basis for this assumption is that high luminosities imply high accretion rates, which according to the standard model of thin disks results in matter forming a geometrically thin, optically thick accretion disk that then has time to liberate its gravitational binding energy. To extract more and more binding energy from an annulus of disk matter, that annulus must continuously accrete inward. The mechanism by which this occurs is thought to be magnetohydrodynamical (MHD) turbulence, which provides an effective viscosity strong enough to account for the observed luminosity. The origin of the MHD turbulence, in turn, is thought to be the nonlinear saturation of the magnetorotational instability (MRI; Balbus & Hawley 1990, 1998).

1.2.2 Broad and narrow line regions

Luminous AGN are host to phenomena not detectable in LLAGN, in particular the broad and narrow emission line regions — BLRs and NLRs, respectively. While some NLRs extend to kiloparsec scale distances that can be spatially resolved in nearby AGN, the BLRs are within about 0.1-1 parsec of the central engine. Information about the BLR can thus only be obtained by analyzing spectra. In addition to emission, each of these regions also give rise to absorption lines. Explaining the physical origins and dynamics of the BLR and NLR is one of the primary focuses of decades of AGN research. A summary of our understanding of this aspect of AGN physics was succinctly stated in Krolik’s

1999 textbook:

What we know for certain about the history and dynamics of AGN emission line matter is very limited: it exists; it moves with a range of line-of-sight velocities generally a few times 10^3 km s^{-1} in the broad line region, and a factor of ten smaller in the narrow line region; and in a few cases reverberation mapping studies provide constraints on the kinematics of the broad line region. All else is speculation.

Since then, great strides have been made on the observational front, as we now live in the age of multi-wavelength astronomy with dedicated reverberation mapping campaigns and massive all-sky surveys providing a wealth of data on AGN. The difficulty on the theory side is that it is not possible to simultaneously simulate the dynamics of the mass reservoir beyond the sphere of influence of the SMBH and the gas dynamics in the vicinity of the central engine, as the Schwarzschild radius is $r_s \approx 10^{-5} (M_{SMBH}/10^8 M_\odot) \text{ pc}$ whereas the Bondi radius is $r_B \approx 150 (M_{SMBH}/10^8 M_\odot)(T_\infty/10^5 \text{ K}) \text{ pc}$. Nevertheless, significant progress has been made on the theoretical front as well, with many studies showing that multi-phase structures appear in both accretion flows and outflows (e.g., Barai et al. 2012; Nayakshin & Zubovas 2012; Mościbrodzka & Proga 2013; Gaspari et al. 2013; Nayakshin 2014). It seems likely that multi-phase structures such as those found numerically will ultimately account for the existence of the BLR and the NLR.

1.2.3 The mass budget

The dominant process responsible for ionizing the BLR and NLR gas is thought to be photoionization. A central parameter in AGN physics is therefore the ‘photoionization parameter’, and there are several definitions for this quantity. One of the most commonly used is

$$\xi = \frac{L_{\text{ion}}}{n_H r^2}, \quad (1.2)$$

where L_{ion} denotes the ionizing luminosity ($> 13.6\text{eV}$), n_H is the number density of hydrogen atoms, and r is the distance from the central engine. Clearly, this can also be expressed as $\xi = 4\pi F_{\text{ion}}/n_H$, where F_{ion} is the ionizing flux, which is an observable quantity. Various line diagnostics can be used to determine n_H . Thus, ξ is known and is typically inferred to occupy values between 0.1 and 1000.

One use of ξ is as a proxy for the distance to the line-emitting gas. If we knew the volume filling factor of this gas, f , then an estimate for how much mass of material is required to account for the

total line emission is $M_{\text{gas}} \sim f m_H n_H r^3$, where m_H is the mass of a hydrogen atom. Estimating the filling factor of the gas requires knowledge of the gas emissivity and the total line luminosity. Rather than determining those, we can approximate $f n_H$ as $C N_H / r$, where C is the global covering fraction and N_H is the gas column density, another observable quantity. Thus $M_{\text{gas}} \sim C m_H N_H r^2 = C m_H N_H L_{\text{ion}} / (\xi n_H)$, or plugging in fiducial values for the BLR,

$$M_{\text{gas,BLR}} = 0.2 \left(\frac{C}{0.1} \right) \left(\frac{N_H}{10^{22}} \right) \left(\frac{L_{\text{ion}}}{10^{45}} \right) \left(\frac{\xi}{20} \right)^{-1} n_{H,9}^{-1} M_{\odot}. \quad (1.3)$$

Similarly, fiducial values for the NLR gives

$$M_{\text{gas,NLR}} = 1.6 \times 10^3 \left(\frac{C}{0.1} \right) \left(\frac{N_H}{10^{21}} \right) \left(\frac{L_{\text{ion}}}{10^{45}} \right) \left(\frac{\xi}{20} \right)^{-1} n_{H,4}^{-1} M_{\odot}. \quad (1.4)$$

Here $n_{H,10}^{-1}$ and $n_{H,4}^{-1}$ denotes number density in units of 10^{10} and 10^4 cm^{-3} , respectively. This estimate of the amount of line emitting gas does not depend on the line luminosity because it is simply the mass associated with a given column density and ionization parameter. We conclude that the mass budget is rather modest and hence the origin of this gas can be explained in a number of ways. As discussed in more detail below, there are two dominant and competing physical pictures of the AGN environment: discrete BLR/NLR clouds versus an accretion disk wind. In the former scenario, the small covering fraction is attributable to there being a population of clouds that only partially cover the central engine, while in the disk wind picture, the small covering fraction can be explained as the small solid angle subtended by the outflow (Murray et al. 1995).

1.3 The debated origins of AGN line emission/absorption

In some sense, the idea of discrete clouds in AGN was the natural outpouring of models that astrophysicists had already developed to understand the nebular physics of HII regions. The notion of a ‘cloud’ as the basic line-emitting entity accompanies the very tool first used to model line emission processes in AGN, namely photoionization modeling (e.g., Davidson 1972). As in calculations still routinely performed today, those first calculations adopted a spherically symmetric gas distribution surrounding a point source of radiation. For example, Bachall & Kozlovsky (1969) introduce their photoionization method with the description “Our models . . . presume a small central object that emits a strong continuum flux and a large gas cloud that surrounds the central source.” Moreover, discrete clouds were hypothesized as the most likely of several explanations for the broad emission

lines by Bachall a few years earlier; here is an excerpt from §4 of Bachall (1966):

If one assumes that the emission lines of a QSS originate in a collection of turbulently moving elements (gas clumps or filaments), then the predicted widths are in agreement with observation if the average turbulent speeds are of the order of a few thousand kilometers per second.

Here, ‘QSS’ stands for quasi-stellar source (as quasars had only been discovered a few years prior), and we should note that similar models invoking ‘microturbulence’ are still being used (e.g., Horne 1995; Bottorff et al. 2000; Bottorff & Ferland 2002; Baldwin et al. 2004; Kraemer et al. 2007), although it is unclear how such supersonic motions can arise and persist (e.g., Kraemer et al. 2012).

1.3.1 Problems with pressure confined clouds

The discrete cloud idea was first given physical credibility in early papers exploring their kinematics and interaction with their local environment (e.g., Mathews 1974; McKee & Tarter 1975; Blumenthal & Mathews 1975; Weynman 1976). In particular, the need for clouds to be pressure confined in order to be long lived and accelerated was pointed out. Even earlier papers had shown that AGN radiation fields supplied enough radiation pressure to accelerate clouds to velocities that could explain the observed blueshifted absorption and the enormous velocities inferred from the widths of emission lines (Mushotzky et al. 1972; Tarter & McKee 1973). However, there was an immediate concern about the stability of radiation pressure accelerated clouds (Williams 1972). A number of authors further explored the issue of stability as it pertains to radiatively accelerated clouds (e.g., Tarter & McKee 1973; Mathews 1974; McKee & Tarter 1975; Krolik 1979; Mathews & Blumenthal 1977; Blumenthal & Mathews 1979). These works unveiled some serious shortcomings in attributing the observed emission and absorption to discrete clouds, even if the right conditions for confinement can be established (see Osterbrock & Mathews 1986 for an early review). Radiation forces generically tend to disrupt clouds on short timescales, by heating and dispersing them or by compressing them, for example, and it was unclear if a mechanism to continuously form new clouds existed.

In this thesis, we confirm that clouds are indeed unstable to radiation forces. This need not preclude their viability as the source of line emission and absorption in AGN, however, for we also find that the natural mechanism invoked to form clouds, namely the thermal instability (TI), can also continually regenerate clouds. This is because cloud acceleration leads to a turbulent medium that then supplies perturbations to the flow that can retrigger TI, leading to an endless cycle of

cloud formation and disruption.

1.3.2 The inadequacy of accretion disks

The cloud idea has persisted, despite the obvious shortcomings related to concerns over their stability, due in part to the inability of accretion disks to explain the broad line emission. The standard model of thin accretion disks predicts a definite radial temperature profile along the disk, with each annulus emitting continuum radiation at a different temperature, thereby forming a multi-blackbody SED. If it is supposed that the broad line profiles are formed in the optically thin atmospheres of these disks, then there will be a definite testable prediction for the widths and shapes of different lines. Lower ionization lines are formed at lower temperatures and thus at larger radii, and they should therefore always be substantially less broad than higher ionization lines since they presumably share the local Keplerian velocity of the optically thick gas in the disk. Typical line widths in the BLR, however, show differences of only a factor of about 2 for low and high-ionization lines, in violation of the predictions for thin accretion disks.

A way around this dilemma is to presume a highly flared outer disk that can intercept ionizing radiation from the inner disk and thus become ionized enough to host emission lines. However, this scenario faces difficulty accounting for the observed widths of emission lines due to the small velocities at large radii. Moreover, it fails to account for the observed absorption lines if the flared region is still optically thick.

The shapes of emission line profiles are equally problematic, as disks are predicted to give rise to double peaked line profiles with very little emission at line center (e.g., Horne & Marsh 1986). This is only observed in a small fraction of AGN (e.g., Eracleous & Halpern 1994).

Finally, accretion disks fail to account for the narrow line emission. This is because in the basic unification scheme, the accretion disk and its atmosphere is entirely obscured by the dusty torus in Type II AGN, yet by definition these objects mainly show emission from a narrow line region. Thus, narrow line regions are often envisioned to host a distinct cloud population of their own.

1.3.3 The plausibility of accretion disk winds

The cloud picture can almost be done away with entirely by attributing the line emission to large scale outflows driven off of the accretion disk by some source of energy that is still hotly debated. The accretion energy can only be converted into thermal, radiative, and/or magnetic

energy sources, hence the three candidate wind launching mechanisms: thermal heating, radiation pressure on resonance lines, and magnetocentrifugal wind launching.

We say ‘almost’ because disk winds are popularly envisioned to be continuous flows, a consequence of analytic studies of winds necessarily being confined to finding steady, smooth flow solutions. Such solutions face an obvious difficulty: radiation can penetrate the entire wind and over-ionize the gas, leaving few lines capable of reproducing the observed line emission. A possible solution to this over-ionization problem was put forth by Murray et al. (1995), who postulated the existence of a layer of self-shielding gas that could filter the ionizing radiation from reaching large parts of the wind. Such a layer showed up naturally in the time-dependent numerical solutions of line-driven winds found by Proga, Stone, & Kallman (2000) and Proga & Kallman (2004). Several followup studies focused on computing synthetic spectra for these solutions have confirmed that this remains a viable model for explaining the origin of the line emission in AGN (e.g., Schurch et al. 2009; Sim et al. 2010).

1.3.4 Persistent notions of discrete clouds

Further developments of the discrete cloud picture proceeded almost in parallel with models of AGN winds and have been met with more success in explaining observations. This is due in large part to the rise of sophisticated photoionization modeling codes such as CLOUDY and XSTAR that are designed to enable modelers to perform spectral fits with observational data. The now widely used locally optimally emitting cloud (LOC; Baldwin et al. 1995) model offers a remarkably good reproduction of observed line strengths. LOC-type models utilize a large grid of photoionization calculations sampling several orders of magnitude in column density and temperature. The accompanying physical picture is that of many clouds with a correspondingly large range of physical properties coexisting in the same region of space. These clouds are also typically envisioned to orbit the central engine at near-Keplerian velocities. This picture overcomes the above mentioned inadequacy of accretion disks atmospheres, as at every velocity, there is now matter with the right physical properties needed to produce line emission from ions with vastly different ionization and excitation energies.

More physically based scenarios invoking discrete clouds to explain the physical nature of the BLR are still considered in the literature. Prominent among these are the bloated star models, in which a population of evolved stars, possibly born within the AGN accretion disk at large radii

where the disk becomes self-gravitating, serve as a vast reservoir of matter capable of forming the BLR. Recent work envisions the clouds to be ultimately produced by thermal instability, the source of the hot gas being the outer layers of the stars that are irradiated by the central engine and thereby lifted off (e.g., Wang et al. 2015). Perhaps more plausible is the ‘failed radiatively accelerated dusty outflow’ (FRADO) model developed by B. Czerny and collaborators (e.g., Czerny & Hryniewicz 2011; Czerny et al. 2015; Czerny et al. 2017). In this scenario, the dust sublimation radius serves as the inner radius of the BLR, and gas at this radius can easily be driven off the accretion disk due to the sudden appearance of dust opacity. At small heights above the disk, these dusty clouds can be too cool to host any ions, but as they get pushed to higher altitudes and become exposed to the radiation field of the AGN, they become sufficiently ionized. Lacking their original dust opacity, they then fall back down. For this model to work, this process would need to happen continuously, and this may indeed be possible judging by recent radiation hydrodynamical simulations that use the most advanced algorithms that accurately treat the radiative transfer problem (e.g., Zhang & Davis 2017). The main weakness of both the bloated star and FRADO models is that the radius of the BLR must be far outside the fiducial radius of 100 – 1000 light days measured by reverberation mapping studies. These models are therefore more appealing to explain phenomena associated with the dusty torus and NLR.

1.3.5 Clouds + winds = clumpy winds

Some of the most recent observational findings have been interpreted as supporting a ‘clumpy wind’ scenario, which rather ironically, is a unification of the competing continuous wind and discrete cloud pictures. Clumpy winds naturally explain observations showing *absorption line variability*. Broad, blueshifted absorption lines provide the clearest evidence of AGN winds, and because they are seen in UV and X-ray spectra, there is a clear association with the nuclear region (e.g., Reeves et al. 2009; Kaastra et al. 2014). Strong variability in these lines is unexpected if the winds are smooth, so this is often taken to be evidence in support of the self-shielding gas at the base of the radiatively driven outflows discussed above (e.g., Ebrero et al. 2015; Mehdipour et al. 2017). The warm absorber phenomenon indicates that the self-shielding layer is not the full story, as warm absorbers are seen at parsec scales (e.g. Kaastra et al. 2012), suggesting that outflows are not just clumpy near their launching radii. There is some evidence in support of the hypothesis of discrete clumps embedded in the wind at both small and large distances (e.g., Mizumoto & Ebisawa 2017).

1.4 AGN clouds: theoretical background

We move on now to discussing the known physics of AGN clouds. Unlike giant molecular clouds found in the interstellar medium, self-gravity is not important for BLR and NLR clouds (for they would then be too heavy to be radiatively accelerated; Mathews 1974), implying that their internal structure is very simple, trivial compared to that of stars and planets. However, self-gravity and the near-vacuum environments surrounding stars and planets typically allows them to be modeled globally as point sources evolving under the laws of classical mechanics. The dynamics of AGN clouds, however, is governed by the equations of hydrodynamics both on small and large scales, and this makes it much more challenging to predict how a population of such clouds evolves globally.

Setting aside that problem, it is first important to understand how AGN clouds form, i.e. how relatively cool condensations can arise within a hot gas bathed in high energy photons, and this much we understand in the context of thermal instability. Regardless of the formation pathway, once a two-phase medium is created, we also know the physics governing the interaction of the cloud with its local surroundings. Here we summarize this known physics, which serves as the theoretical foundation on which our work is based.

1.4.1 Thermal instability criteria

Eugene Parker, a leading pioneer in solar physics and space science who discovered the solar wind by solving the equations of gas dynamics, appears to be the first person to conceive of a condensation process occurring via thermal instability (TI; Parker 1953). Parker considered temperature perturbations, δT , in a diffuse gas whose thermal equilibrium state is set by a balance between T -independent energy gains and T -dependent radiative losses, $\mathcal{L}(\rho, T)$. He reasoned that in a parcel of gas with fixed density, instability results if radiative losses increase ($\delta\mathcal{L} > 0$) as the gas cools ($\delta T < 0$). Runaway cooling results, and today we recognize this as the isochoric criterion for TI,

$$\left(\frac{\partial\mathcal{L}}{\partial T}\right)_\rho < 0. \quad (1.5)$$

It was George Field who in 1965 first rigorously developed the linear theory of thermal instability, pointing out that Parker's isochoric criterion is much more difficult to trigger for common astrophysical cooling functions, since a perturbed gas parcel has a strong tendency to maintain its pressure (through the mediation of sound waves) not its density (Zanstra 1955). The theory of

cloud formation discussed in this thesis is based on Field’s isobaric criterion for TI,

$$\left(\frac{\partial \mathcal{L}}{\partial T}\right)_p < 0. \quad (1.6)$$

1.4.2 Understanding cloud formation

Once it was appreciated that TI is a robust linear instability, it became clear that the saturation of this instability would lead to a multi-phase medium (e.g., Zanstra 1955; Field et al. 1969). Phase diagrams were introduced in the early two-phase models applied to clouds in the interstellar medium (e.g., Shu et al. 1972). Two-phase models appear to have first been applied to AGN by Army (1970) and Wolfe (1974), while the ‘standard two-phase model’ for AGN came out of the work of Krolik et al. (1981), who introduced a specific variety of phase diagram commonly called the S-curve. It was made clear from these works and others (e.g., Lepp et al 1985; Kallman & Mushotzky 1985) that the heating and cooling processes expected in an AGN radiation field generically satisfy the conditions necessary for TI. Moreover, the S-curve proved to be a useful visual tool for gauging whether or not a given net cooling function \mathcal{L} features a thermally unstable zone.

Figure 1.2 is fig. 6 from Krolik et al. (1981) showing a schematic of an S-curve, so-called because typical radiative equilibrium curves, defined as the $\mathcal{L} = 0$ contour, have this ‘S’ shape when plotted in $\log(T) - \log(\Xi)$ space. The ‘pressure’ photoionization parameter $\Xi = (F_X/c)/p$ is essentially the ratio of the energy density of photons, F_X/c , to the energy density of the gas. As asserted in the figure caption, stability results when $d(\ln T)/d(\ln \Xi) > 0$, meaning that an alternative isobaric criterion for TI is

$$\frac{d(\ln T)}{d(\ln \Xi)} < 0. \quad (1.7)$$

This has the simple geometric interpretation that portions of the S-curve with a negative slope are thermally unstable regions of parameter space. Gas in a single phase will occupy only 1 point on this phase diagram, but if this point ever reaches one of the two vertical slope regions (marked by asterisks in Figure 1.2), TI will occur and the gas will trace one of the two dashed lines on this phase diagram. Since $\Xi \propto p^{-1}$, isobaric processes follow vertical trajectories on this phase diagram — the deviations from constant pressure shown are likely exaggerated. In any case, a two-phase medium results; the dashed line on the left is the pathway typically associated with cloud formation, where the nonlinear saturation of TI produces a relatively cool cloud appearing within a hot intercloud

medium.

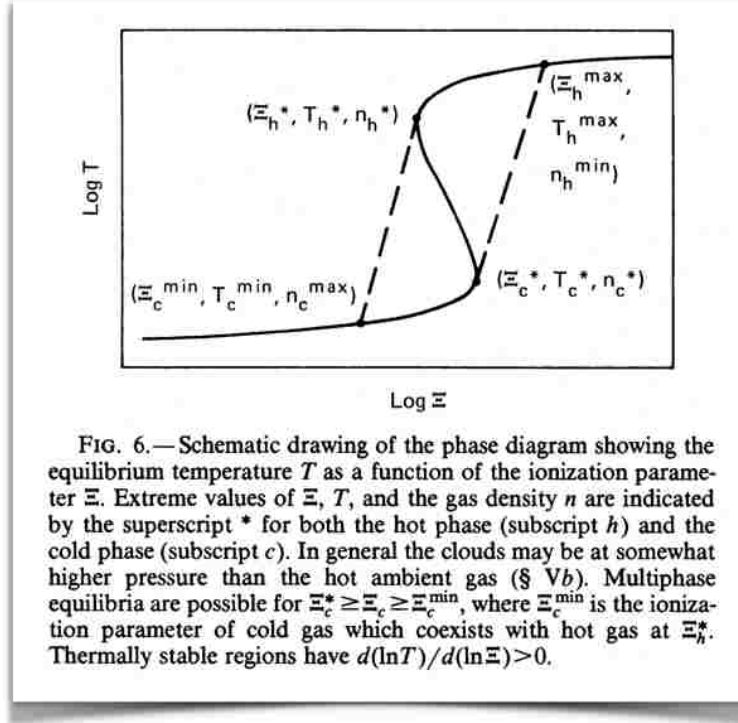


Figure 1.2: Figure from Krolik et al. (1981) summarizing the formation mechanism of clouds via the nonlinear saturation of the thermal instability.

To see that (1.7) is equivalent to Field's isobaric criterion for TI requires a bit of effort, starting with this calculus identity,

$$\left(\frac{\partial y}{\partial x}\right)_z \left(\frac{\partial z}{\partial y}\right)_x \left(\frac{\partial x}{\partial z}\right)_y = -1. \quad (1.8)$$

Applying this identity to relate the cooling function \mathcal{L} to the pressure p and temperature T gives

$$-\left(\frac{\partial T}{\partial p}\right)_{\mathcal{L}} = \frac{(\partial \mathcal{L}/\partial p)_T}{(\partial \mathcal{L}/\partial T)_p}. \quad (1.9)$$

Exchanging p in favor of Ξ on the l.h.s and using some algebra to introduce logarithms gives

$$\left(\frac{\partial \ln T}{\partial \ln \Xi}\right)_{\mathcal{L}} = \frac{p}{T} \frac{(\partial \mathcal{L}/\partial p)_T}{(\partial \mathcal{L}/\partial T)_p}. \quad (1.10)$$

The l.h.s is our alternative criterion, while Field's criterion shows up in the denominator of the r.h.s. Therefore, these criteria are indeed equivalent provided that $(\partial \mathcal{L}/\partial p)_T > 0$. For an ideal gas law,

$p = (\rho/m)kT$, we can exchange p for ρ since T is held constant,

$$\left(\frac{\partial \mathcal{L}}{\partial p}\right)_T = \left(\frac{\partial \mathcal{L}}{\partial \rho} \frac{\partial \rho}{\partial p}\right)_T = \frac{m}{kT} \left(\frac{\partial \mathcal{L}}{\partial \rho}\right)_T. \quad (1.11)$$

Now it happens that $(\partial \mathcal{L}/\partial \rho)_T \geq 0$ for all cooling functions relevant in AGN because cooling rates vary as ρ^2 , whereas heating rates are weakly dependent on density (see also the appendix of Balbus & Soker 1989). Thus, in practice, the equivalence of these instability criteria holds true.

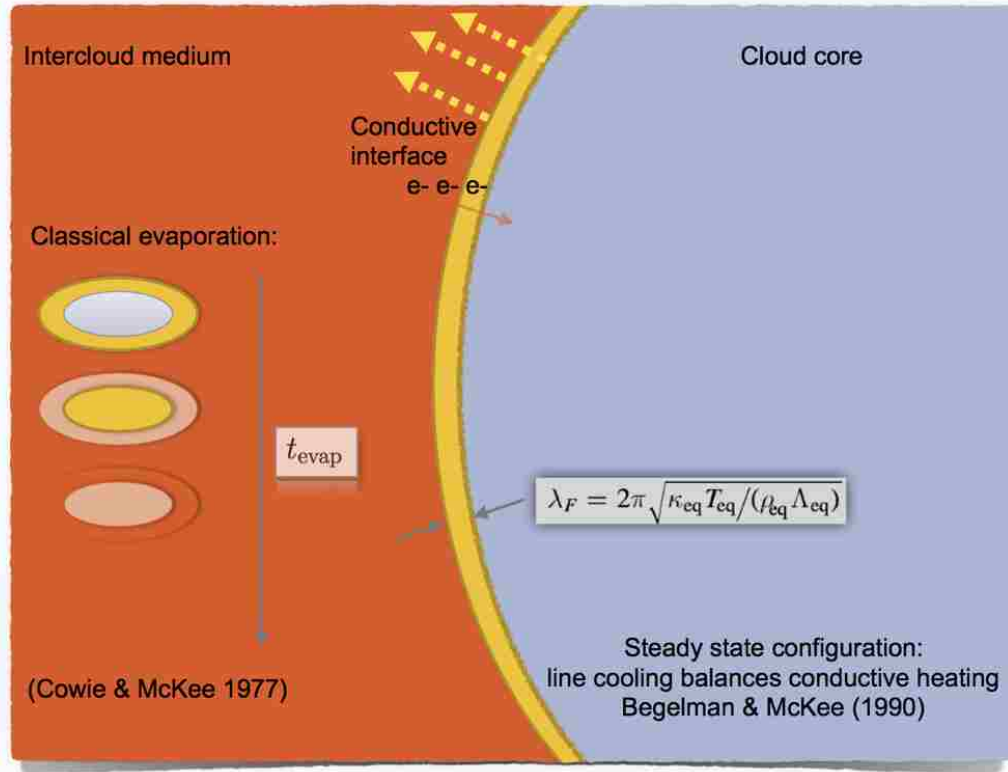


Figure 1.3: Schematic of both a large and small AGN cloud, depicting the physics taking place in cloud interfaces (yellow layer). Clouds are held in pressure equilibrium by the surrounding intercloud medium and a conductive interface bridges these two regions. Large clouds radiate away enough line photons to balance heat diffusion through the interface. Small clouds evaporate when their characteristic dimension approaches the width of the interface, the Field length, λ_F .

1.4.3 Equilibria and evaporation of static AGN clouds

The multi-phase picture just described offers little insight into the dynamics and stability of newly formed clouds. Moreover, one can imagine other cloud formation pathways, such as blobs uplifted for the surface of an accretion disk or condensations forming as the result of shocks. Regardless of how a cloud forms, how does it then evolve?

Implicit in the two-phase model is confinement by a hot intercloud medium, as the hot and cold

phases are in a near-perfect pressure balance. This is the first basic requirement for an equilibrium to be reached, for if the clouds were over (under) pressurized, they would expand (be squeezed) on a sound crossing timescale until pressure forces do balance. These isobaric conditions should apply to all clouds, independent of how they formed.

Once warmer gas is in thermal contact with cooler gas, conduction will act to smooth out any temperature gradients. This is why the internal structure of a static cloud is exceedingly simple: electrons will diffuse about until the entire core of the cloud has the same temperature. Likewise, heat diffusion will drive the intercloud medium into thermal equilibrium at a lower temperature than before the cloud existed. How about at the cloud’s interface — will conduction always act to eliminate this temperature gradient? The process of gradually heating the cloud through its interface is known as evaporation and was first explored by Cowie & McKee (1977). However, this question was not definitively addressed for a couple decades until the work of Begelman & McKee (1990).

The essential logic handed down by Begelman & McKee (1990) is the following. If clouds are ultimately the source of line emission in AGN, it means that line cooling is an important process in determining their overall thermal equilibria. Yet, the two-phase model leads us to believe that heating and cooling are in balance both in the cloud core and in the intercloud gas, since each phase occupies a point on the contour $\mathcal{L} = 0$. If the cloud interfaces were also in radiative equilibrium, then thermal conduction would proceed unimpeded, always acting to heat up the cloud. We conclude, therefore, that an equilibrium state is possible if evaporative heating can be offset by increased line emission in the cloud interfaces. Indeed, Figure 1.2 shows that for the left dashed line relevant for condensation, the region between the points on the S-curve has $\mathcal{L} > 0$. Evidently, the cloud interfaces occupy this range of parameter space, bridging the two phases, a numerical finding made by Proga & Waters (2015).

Begelman & McKee (1990) further showed that striking a balance between line cooling and conductive heating is not possible for small clouds. Specifically, they identified the critical length scale below which clouds will always undergo evaporation. They termed this the Field length, defined as²

$$\lambda_F = 2\pi\sqrt{\frac{\kappa T}{\rho\Lambda}}, \quad (1.12)$$

In particular, notice that λ_F is a local property of the radiative environment and therefore does not

²Begelman & McKee (1990) defined the Field length as $\lambda_F = \sqrt{\kappa T/\rho\Lambda}$. We present a physical argument in Chapter 4 for why it is important to include the 2π , and this is also supported by numerical findings.

depend on the size of the cloud (here, Λ is the total cooling rate, related to \mathcal{L} through $\mathcal{L} = \Lambda - \Gamma$, with Γ the total heating rate). We can now arrive at the physical picture illustrated in Figure 1.3. Clouds can be assigned a characteristic dimension $R_c = V_c^{1/3}$, where V_c is the volume of the cloud, whereas λ_F determines the width of their interfaces. When $R_c \gg \lambda_F$, clouds are long lived, at least from an energetics standpoint, in part because their surface areas are large and they can easily offset conductive heat fluxes through their interfaces by radiatively cooling. When $R_c \lesssim \lambda_F$, on the other hand, clouds undergo classical evaporation in the manner identified by Cowie & McKee (1977).

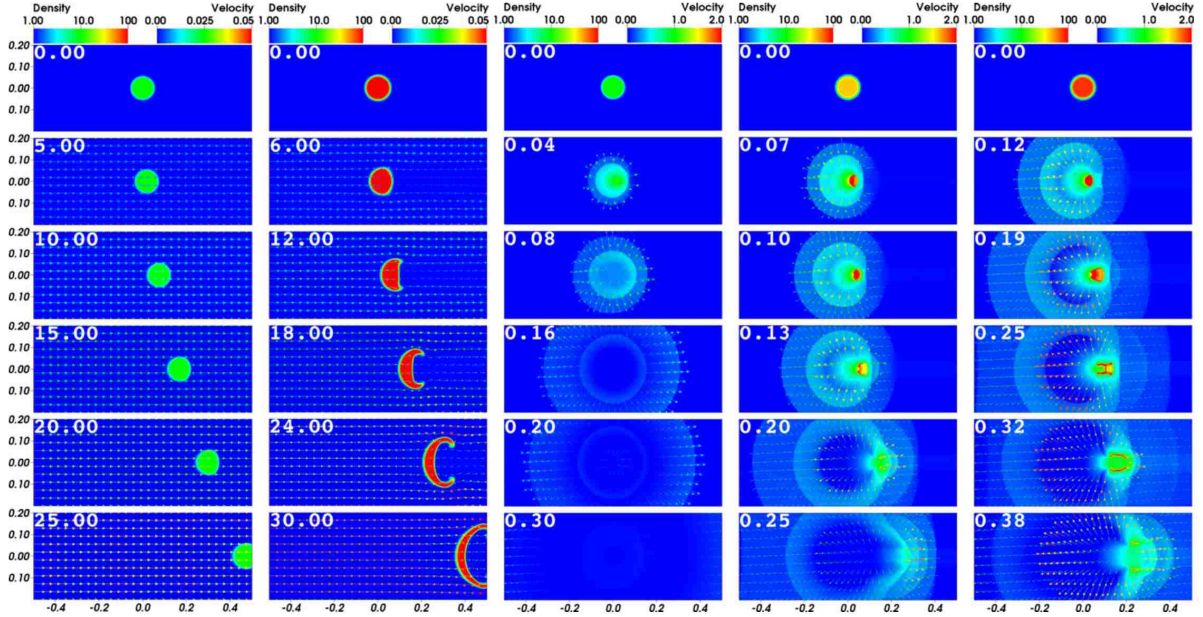


Figure 1. Sequences of density maps overlplotted with the velocity fields for runs S10, S200, A10, A40, and A80 (left to right) at five different times, shown at upper left in each panel.

Figure 1.4: Figure 1 from Proga et al. 2014. Their figure caption describes what run is shown in each column, and their naming convention uses ‘S’ to denote pure scattering opacity and ‘A’ to denote pure absorption opacity. The number after this label is the optical depth of the initial cloud. Thus, clouds in the first and third column are mildly optically thick, and we see that such a cloud dominated by scattering opacity can accelerate uniformly, while one dominated by absorption opacity will be quickly heated and dispersed. Optically thick clouds will be destroyed by both types of opacity on similar timescales but in characteristically different ways.

1.4.4 Destruction of accelerated AGN clouds

The physics represented in Figure 1.3 merely demonstrates that large clouds can be long lived from a consideration of their thermodynamics. When the forces acting on AGN clouds are examined instead, it is readily shown the radiation field is powerful enough to accelerate clouds to velocities that would explain the widths of broad emission lines (e.g., Mathews 1974). However, the ability of clouds to undergo a prolonged period of acceleration hinges on their stability when subjected to

these radiation forces. Pioneering efforts to understand the possibility of cloud destruction from radiation forces identified Rayleigh-Taylor type instabilities, the details of which depend on the opacity. Mathews & Blumenthal (1977, 1979) investigated the role of continuum opacity and found relatively small growth rates for optically thin clouds, and an overstability for optically thick clouds. Krolik (1979) identified a Rayleigh-Taylor instability driven by radiation pressure from line photons, mainly Ly α photons in optically thin clouds and possibly Mg II photons in more opaque clouds. McKee (1975) suggested that there is a strong tendency for initially optically thick clouds to become optically thin due to various destruction mechanisms that would break up the clouds into smaller clumps. Radiation forces, the Kelvin-Helmholtz instability, cloud-cloud collisions, and issues with confinement could all conceivably contribute to this.

Owing to advances in algorithms to solve the equations of radiation hydrodynamics (RHD), it has recently become possible to explore cloud destruction numerically. Proga et al. (2014) presented RHD simulations revealing how AGN clouds of differing optical depths evolve when their opacity is due either to pure scattering or pure absorption processes. Figure 1.4 is a plot from their paper illustrating various cases. Mildly optically thick clouds dominated by absorption opacity tend to rapidly and uniformly heat, causing them to expand almost like a balloon before they can significantly accelerate. Optically thick clouds dominated by scattering opacity, on the other hand, permits rapid acceleration but also leads to rapid destruction. This study concluded that a promising approach that could lead to more efficient acceleration may be found by first letting clouds form via thermal instability. This idea constitutes the basis for the work presented here.

1.5 Thesis summary

The goal of this thesis is to add several important contributions to the above basic understanding of cloud dynamics. Namely, we will present a comprehensive theory of cloud formation and acceleration including an exploration of the effects of flux variability, as well as methods to calculate both synthetic absorption and emission lines from numerical simulation data — a technique that will hopefully allow detailed comparisons with observations in the future. As for the origin of line emission in AGN, i.e. whether it originates in discrete clouds, continuous self-shielded winds, or clumpy winds, we prefer to remain open-minded, although there seems a clear path forward in how to ultimately address this question. We touch on this in the introduction to the next chapter, and present a few ideas for making the first steps toward this goal in our conclusions.

This thesis is organized as follows. In Chapter 2, we derive the equations of gas dynamics, which will be referred to throughout, and we further apply these equations to simple examples of clouds in order to motivate subsequent chapters. In Chapter 3, we derive the radiation source terms appearing in the hydrodynamic equations using radiative transfer theory. In Chapter 4, we linearize the equations of gas dynamics, which allows us to derive the instability criteria for TI stated above, as well as to arrive at initial conditions for our cloud simulations. In Chapter 5, we present results of the first simulations that considered the dynamics of cloud formation and acceleration simultaneously and self-consistently, work that was published by Proga & Waters (2015). In Chapter 6, we present the work of Waters & Proga (2016), which further considered the role of flux variability on the cloud formation and acceleration process. In Chapter 7, we present the work of Waters et al. (2017), where self-consistent calculations of synthetic absorption line profiles of the simulations were presented. In Chapter 8, we review the basic principles of reverberation mapping as it relates to AGN clouds, summarizing the related work of Waters et al. (2016). Finally, in Chapter 9 we conclude by summarizing our results as well as our approach for generalizing the methods presented herein to further explore cloud dynamics using models tailored for Type I and Type II AGN SEDs.

Chapter 2

THE EQUATIONS OF GAS DYNAMICS

In this chapter we discuss the simplest equations governing the dynamics of gas in AGN, namely the basic equations of hydrodynamics. By ‘simplest’ equations, we mean that it is likely the case that a much more complicated set of equations, namely that of multi-group radiation magnetohydrodynamics coupled with the non-LTE statistical rate equations, eventually needs to be solved to obtain a complete model of the AGN environment. Let us briefly consider why this may be.

Gas in AGN is observed to be partially ionized—the spectra show prominent emission and absorption lines, ionization edges, etc. Partially ionized gas is prone to being magnetized, as currents can easily be supported by the existence of free electrons. Magnetic fields can arise locally via a dynamo process or be advected inward from plasma originating in the interstellar medium of the galaxy. In the presence of magnetic fields, electrons cannot flow freely across magnetic field lines. In general, therefore, the equations of magnetohydrodynamics with anisotropic conduction must be solved. Moreover, since AGN are by definition copious emitters of continuum radiation, the forces due to radiation can be dominant over all others. If the gas responsible for the observed line emission in AGN is truly in the form of optically thick clumps, then the dynamics of these clumps is governed by the equations of radiation hydrodynamics. Solving these entails accounting for how the gas is coupled to the radiation field, i.e. identifying opacities and solving the radiative transfer problem. Realistic opacities can be sensitive functions of frequency, so in general a multi-group approach is needed to include different opacities for different parts of the spectral energy distribution (SED). For a detailed exposition of these techniques see Mihalas & Mihalas (1984).

Now, unless the number densities are high enough that collisional processes dominate the radiative ones for populating and depopulating excited states, the gas will not be in local thermodynamic equilibrium (LTE) and the ionization structure of the gas can only be determined by solving kinetic rate equations. The non-LTE problem is both difficult, requiring extensive atomic databases, and computationally expensive, involving iteration on very large matrices. Hence, modeling efforts tend to make very simplifying assumptions, such as neglecting the gas dynamics altogether by assuming static slabs of gas, as well as invoking the optically thin assumption to make the radiative transfer problem tractable. This is the approach taken by most photoionization codes, e.g. CLOUDY and

XSTAR.

The situation can become even more complex than this if the ionizing radiation field is sufficiently shielded or diluted in some regions, as ‘dust’ (that is, grains of solid material) can form. This dust need not be strongly coupled with the gas, especially in low density environments such as the narrow line region, thereby invalidating the single fluid approximation. In this circumstance, a multi-fluid approach would need to be taken and the non-LTE rate equations would need to account for the various dust formation and destruction pathways.

Finally, to model gas dynamics down to the smallest scales, say within $100 GM/c^2$ of the SMBH, the above modeling approach must be applied in a fully general relativistic framework. In particular, the accretion disk that gives rise to the immense ionizing continuum radiation field should ultimately be modeled by solving all these complicated equations. Doing so may be the only way to properly address fundamental problems in accretion theory such as the overall lifetime, structure, evolutionary state, and stability of the disk, as well as the relative importance of MRI turbulence in the presence of powerful radiation fields and strong gravity. The development of these models should be guided by the need to explain phenomena that show up in X-ray observations, such as strong flux variability and ultra fast outflows.

Alas, it should be clear from this discussion that a modeling approach based on solutions to the Newtonian equations of hydrodynamics represents a significant simplification to what may one day be achievable. Nevertheless, the basic Newtonian hydrodynamics framework is very powerful in that by solving these equations, we are likely modeling the true dynamics to a good first approximation. In this sense, these models for clouds can be considered ‘realistic’, as they do represent self-consistent solutions of essentially Newton’s second law and the first law of thermodynamics applied to the flow. In other words, we consider a parcel of gas, try to identify the most important forces acting on it and the dominant means by which it can exchange heat with the environment, and then we identify how this parcel evolves in time as a result. The only way that solving the full complicated set of equations described above is going to qualitatively alter this ‘0th’ order solution is if we are totally missing or misrepresenting an important force or thermodynamic process. We avoid this by explicitly limiting our attention to optically thin, unmagnetized clouds, in which case we are able to properly include the relevant radiation forces. To paraphrase a famous quote by Albert Einstein, “make things as simple as possible, but not simpler.” That has been the guiding philosophy here.

2.1 Newtonian equations of hydrodynamics

There are many excellent texts that rigorously derive the equations of hydrodynamics. Our favorite presentations are those of Shu (1992), Castor (2004), Mihalas & Mihalas (1984), Zel'dovich & Raizer (1966), Rezzola & Zannotti (2013), and Poisson & Will (2014). Here we take as a starting point the simplest notion of mass conservation as well as Newton's second law and the first law of thermodynamics, and from these derive the equations of hydrodynamics in conservative form, as it is in this form that we will solve these equations numerically. Along the way we will attempt to point out several conceptual subtleties, referring the interested reader to specific sections of the above texts for further details.

A note on terminology: below we refer repeatedly to the comoving frame and the fixed frame. The latter is the same as the Eulerian frame, while the former denotes a Lagrangian perspective and may also be referred to as the fluid element's rest frame.

2.1.1 Mass conservation

Mass conservation is most simply and intuitively represented in the comoving frame of a fluid element that has mass density $\rho = \rho(\mathbf{x}, t)$, bounding volume \mathcal{V} , and total mass $M = \int_{\mathcal{V}} \rho dV$:

$$\frac{DM}{Dt} = 0. \quad (2.1)$$

The advective derivative operator, D/Dt , defined as

$$\frac{Df}{Dt} \equiv \frac{\partial f}{\partial t} + \mathbf{v} \cdot \nabla f \quad (2.2)$$

for any function f , where $\mathbf{v} = \mathbf{v}(\mathbf{x}, t)$ is the fluid element's velocity, translates between the comoving frame and the Eulerian frame. The subtlety here is how to rigorously go from the intuitive statement $DM/Dt = 0$ to the conservative form of the mass continuity equation,

$$\frac{\partial \rho}{\partial t} + \nabla \cdot (\rho \mathbf{v}) = 0. \quad (2.3)$$

Simply expanding the divergence term in (2.3) and using (2.2), followed by multiplying by dV and integrating gives

$$\int_{\mathcal{V}} \left(\frac{D\rho}{Dt} + \rho \nabla \cdot \mathbf{v} \right) dV = 0. \quad (2.4)$$

Incidentally, this equation provides two equivalent notions of incompressibility, i.e. constant density in the comoving frame, $D\rho/Dt = 0$, implies $\nabla \cdot \mathbf{v} = 0$ and vice versa. How, though, do we recognize that the full left hand side equals DM/Dt , as it must? The rigorous result that makes the connection is known as the Reynolds transport theorem (for a derivation, see e.g., §18 of Mihalas & Mihalas 1984) and takes several forms:

$$\begin{aligned} \frac{D\mathcal{F}}{Dt} &= \int_{\mathcal{V}} \left(\frac{Df}{Dt} + f\nabla \cdot \mathbf{v} \right) dV; \\ &= \int_{\mathcal{V}} \left[\frac{\partial f}{\partial t} + \nabla \cdot f\mathbf{v} \right] dV; \\ &= \int_{\mathcal{V}} \frac{\partial f}{\partial t} dV + \int_S f\mathbf{v} \cdot dS. \end{aligned} \tag{2.5}$$

Here, S is the surface bounding the volume \mathcal{V} and the two functions \mathcal{F} and f are related as $\mathcal{F}(t) = \int_{\mathcal{V}} f(\mathbf{x}, t) dV$. It is to be emphasized that $f(\mathbf{x}, t)$ can represent a scalar, vector, or tensor field. The first form with $f(\mathbf{x}, t) = \rho(\mathbf{x}, t)$ answers the question just posed, while the second establishes the desired conservative equation, (2.3). The third form of this theorem directly links the comoving and fixed frame notions of mass conservation.

2.1.2 Momentum conservation

A statement for momentum conservation follows indirectly from applying Newton's second law to the fluid element,

$$\rho \frac{D\mathbf{v}}{Dt} = -\nabla p + \rho \sum_i \mathbf{f}_i. \tag{2.6}$$

This equation applies to the rest frame of the fluid element (hence the \mathbf{a} of $m\mathbf{a} = \sum_i \mathbf{F}_i$ is appropriately $D\mathbf{v}/Dt$) and the forces consist of that due to the pressure as well as any body forces \mathbf{f}_i , each representing a force per unit mass. Plugging in the definition of the advective derivative gives Euler's equation,

$$\frac{\partial \mathbf{v}}{\partial t} + \mathbf{v} \cdot \nabla \mathbf{v} = -\frac{1}{\rho} \nabla p + \sum_i \mathbf{f}_i. \tag{2.7}$$

The only subtlety is recognizing that while this a vector equation, its conservation form requires working with tensors. There is really hidden microphysics at play here: in identifying the specific pressure force as $-\nabla p/\rho$, we have implicitly assumed an isotropic pressure field. That is, we take the stress tensor of the flow field to be

$$\mathbb{T} = p\mathbb{I}, \tag{2.8}$$

where \mathbb{I} is just the unit tensor, which in component form is just δ_{ik} . Note also that we have confined our attention to inviscid fluids, meaning that the viscous stress tensor that would make (2.7) the Navier-Stokes equation is absent.

We have introduced the stress tensor because it is clear from the second relation in (2.5) that a conservation law in which f represents the momentum, $\rho\mathbf{v}$,¹ will involve the divergence of a tensor quantity, namely the momentum flux density, $\rho\mathbf{v}\mathbf{v}$. In component form this is $\rho v_i v_k$ and is understood as the flux of the i -th component of the momentum in the k -th direction. Its divergence satisfies $\partial_i \rho v_i v_k = v_k \partial_i \rho v_i + \rho v_i \partial_i v_k$, where repeated indices imply summation over all components, or in vector notation,

$$\nabla \cdot (\rho\mathbf{v}\mathbf{v}) = \mathbf{v}[\nabla \cdot (\rho\mathbf{v})] + (\rho\mathbf{v} \cdot \nabla)\mathbf{v}. \quad (2.9)$$

Now, if we multiply (2.7) by ρ and then add it to (2.3) multiplied by \mathbf{v} , we immediately obtain both terms on the right hand side of (2.9). This allows us to almost arrive at a conservation form of the momentum equation, as we have

$$\frac{\partial \rho\mathbf{v}}{\partial t} + \nabla \cdot (\rho\mathbf{v}\mathbf{v}) = -\nabla p + \sum_i \mathbf{f}_i. \quad (2.10)$$

The actual conservation form,

$$\frac{\partial \rho\mathbf{v}}{\partial t} + \nabla \cdot (\rho\mathbf{v}\mathbf{v} + p\mathbb{I}) = \sum_i \mathbf{f}_i, \quad (2.11)$$

results by recognizing that

$$\nabla p = \nabla \cdot \mathbb{T}. \quad (2.12)$$

It is easiest to see this in component form, as $\partial_i T_{ik} = \partial_i p \delta_{ik} = p \partial_i \delta_{ik} + \delta_{ik} \partial_i p$, but $\partial_i \delta_{ik} = 0$ and $\delta_{ik} \partial_i p = \partial_k p$, which in vector notation is indeed ∇p .

That (2.10) and (2.11) both embody statements of momentum conservation is seen with the help of the Reynolds Transport Theorem. A Lagrangian viewpoint is implied by (2.10) upon looking to the second relation in (2.5) with $f = \rho\mathbf{v}$. We have

$$\frac{D}{Dt} \int_{\mathcal{V}} \rho\mathbf{v} dV = \int_{\mathcal{V}} \left[-\nabla p + \sum_i \mathbf{f}_i \right] dV. \quad (2.13)$$

In words, the change of a fluid element's total momentum with time, when measured in that

¹More precisely, $\rho\mathbf{v}$ is mass flux density or equivalently, momentum density.

element's rest frame, is found by determining the net force acting on the element. If instead we prefer to track momentum conservation in the Eulerian frame, we look to (2.11) and imagine a surface S bounding a fixed region of space, such as a single zone in a finite volume simulation. The flux of momentum in and out of S is $\rho \mathbf{v} \mathbf{v} + p \mathbb{I}$ and if there were no body forces, the net change in momentum within the volume \mathcal{V} bound by that surface per unit time would be entirely due to this flux. The quantity $\rho \mathbf{v} \mathbf{v}$ is the advection of the momentum through S due to the bulk flow (both from within and outside \mathcal{V}), while p measures the momentum change due to the force arising from the pressure field.

2.1.3 Energy conservation

The 1st law of thermodynamics states that when an amount of heat, δQ , is added to a fluid element, some of it will be used for expansion by performing $p d\mathcal{V}$ work and the remainder will increase its internal energy, $d\mathcal{E}$, i.e.

$$\delta Q = d\mathcal{E} + p d\mathcal{V}. \quad (2.14)$$

Here, each term has units of energy per unit mass. The heat differential δQ can be quantified by identifying all heating/cooling rates, which are ultimately due to either internal processes (e.g., absorption or emission) or external heat fluxes (e.g., conduction). That is, heat can either be deposited or lost locally at some rate \dot{q} (the net energy gain per unit mass per unit time) or transported in/out of the fluid element from/to neighboring elements at some rate that can be quantified as the divergence of a heat flux vector \mathcal{H} (the energy per unit area per unit time; see, for example, §1.4 of Poisson & Will 2014 for a derivation):

$$\delta Q = \mathcal{V} (\rho \dot{q} dt - \nabla \cdot \mathcal{H} dt). \quad (2.15)$$

In a gas dynamics context, the first law applies in the comoving frame as the flow evolves in time. Therefore, we should write (2.14) as

$$\frac{1}{\mathcal{V}} \frac{D\mathcal{E}}{Dt} + \frac{p}{\mathcal{V}} \frac{D\mathcal{V}}{Dt} = \frac{\delta \dot{Q}}{\mathcal{V}}, \quad (2.16)$$

where $\delta \dot{Q}/\mathcal{V} = \rho \dot{q} - \nabla \cdot \mathcal{H}$ from (2.15). Noting that for $p d\mathcal{V}$ to have units of energy per unit mass, \mathcal{V} must be the specific volume of the fluid element (volume per unit mass), which means $\mathcal{V} = 1/\rho$.

Manipulating the pressure work term gives

$$\frac{p}{\mathcal{V}} \frac{D\mathcal{V}}{Dt} = \rho p \frac{D\rho^{-1}}{Dt} = -\frac{p}{\rho} \frac{D\rho}{Dt} = p \nabla \cdot \mathbf{v}, \quad (2.17)$$

where in the last equality we used the continuity equation in the form $D\rho/Dt = -\rho \nabla \cdot \mathbf{v}$. Also, since we will later attribute \dot{q} solely to radiative processes (see Chapter 3), in which context the convention is to define a *net cooling* function \mathcal{L} , we will exchange \dot{q} in favor of $-\mathcal{L}$. We can finally cast the 1st law as it is commonly written for hydrodynamics,

$$\rho \frac{D\mathcal{E}}{Dt} = -p \nabla \cdot \mathbf{v} - \rho \mathcal{L} - \nabla \cdot \mathcal{H}. \quad (2.18)$$

Arriving at the conservation form of the Eulerian energy equation first requires realizing that the body forces \mathbf{f}_i appearing in (2.11) will each do work on the gas according to $\mathbf{f}_i \cdot \mathbf{v}$. The conserved energy is therefore the total energy, which is the sum of (2.18) and the mechanical energy, given by the force equation dotted with \mathbf{v} . It is simplest to dot \mathbf{v} with (2.6), as we readily see that $\rho \mathbf{v} \cdot D\mathbf{v}/Dt$ can be rewritten in terms of the kinetic energy density, $\rho v^2/2$, because

$$\frac{D}{Dt} \frac{\rho v^2}{2} = \frac{\rho}{2} \frac{D\mathbf{v} \cdot \mathbf{v}}{Dt} + \frac{v^2}{2} \frac{D\rho}{Dt} = \rho \mathbf{v} \cdot \frac{D\mathbf{v}}{Dt} - \frac{\rho v^2}{2} \nabla \cdot \mathbf{v}, \quad (2.19)$$

where in the second equality we have again employed the continuity equation in the form $D\rho/Dt = -\rho \nabla \cdot \mathbf{v}$. Writing out $D(\rho v^2/2)/Dt$ using (2.2), we find the mechanical energy equation,

$$\frac{\partial}{\partial t} \frac{\rho v^2}{2} + \mathbf{v} \cdot \nabla \frac{\rho v^2}{2} + \frac{\rho v^2}{2} \nabla \cdot \mathbf{v} = -\mathbf{v} \cdot \nabla p + \sum_i \mathbf{f}_i \cdot \mathbf{v}. \quad (2.20)$$

Recognizing a product rule of a divergence term on the l.h.s brings us closer to conservation form,

$$\frac{\partial}{\partial t} \frac{\rho v^2}{2} + \nabla \cdot \left(\frac{\rho v^2}{2} \mathbf{v} \right) = -\mathbf{v} \cdot \nabla p + \sum_i \mathbf{f}_i \cdot \mathbf{v}. \quad (2.21)$$

We further recognize a piece of a product rule from the divergence term $\nabla \cdot \rho \mathbf{v}$ on the r.h.s. The other piece comes from the first term on the r.h.s of (2.18); before adding these equations, we must address the remaining Lagrangian term, $\rho D\mathcal{E}/Dt$. This is aided by the following identity that applies to any function f ,

$$\rho \frac{Df}{Dt} = \frac{\partial \rho f}{\partial t} + \nabla \cdot \rho \mathbf{v} f; \quad (2.22)$$

it is easily proved by expanding out the divergence and using (2.3). Employing this identity leaves only partial time derivative and divergence terms upon finally adding together (2.21) and (2.18). We have therefore arrived at the total energy equation in conservation form,

$$\frac{\partial}{\partial t} \left(\rho \mathcal{E} + \frac{\rho v^2}{2} \right) + \nabla \cdot \left[\left(\rho \mathcal{E} + \frac{\rho v^2}{2} + p \right) \mathbf{v} \right] = -\rho \mathcal{L} - \nabla \cdot \mathcal{H} + \sum_i \mathbf{f}_i \cdot \mathbf{v}. \quad (2.23)$$

We emphasize again that $-\rho \mathcal{L}$ denotes a generic volumetric source term that besides radiative heating and cooling, can include both heating gains and losses due to magnetic dissipation, shock heating, cosmic ray heating, etc.

2.1.4 Equation of state

The above derivations provide five equations (1 for mass, 1 for total energy, and 3 for each component of the momentum) for seven unknowns — five primitive variables (ρ, \mathbf{v}, p) , the specific internal energy, \mathcal{E} , and the temperature T , as \mathcal{L} and \mathcal{H} are both functions of T . We therefore need to look to kinetic theory for an equation of state relating T , \mathcal{E} , and p and therefore providing a closure condition for this set of equations. With the exception of environments involving degenerate matter (e.g. the interiors of neutron stars and white dwarfs or their ejecta upon merger), astrophysical fluids almost always behave as an ideal gas with equation of state $p = nkT$. The individual particles in a fluid element, while highly collisional to justify a fluid treatment, are nevertheless non-interacting (namely, their kinetic energies are large compared to their interaction energy) unlike the particles in degenerate matter. This includes fluids in non-relativistic, relativistic, and ultra-relativistic (e.g., neutrino or photon fluids) regimes (see Ch. 2 in Rezzolla & Zanotti 2013).

At this point, we should take care to draw the distinction between perfect fluids and ideal fluids, as they mean totally different things, and yet not all authors adhere to the same definitions. When both viscosity and thermal conduction are absent, the fluid is labeled perfect. Since we account for the latter but neglect the former, we are considering a non-perfect, albeit inviscid fluid. An ideal fluid is often taken to be defined as any fluid with an equation of state satisfying

$$\rho \mathcal{E} = \frac{p}{\gamma - 1}. \quad (2.24)$$

This terminology seems to be the more intuitive but is precisely opposite to that used by Mihalas & Mihalas (1984)!

Here we collect some results for fully ionized gases, where each species making up the plasma — free electrons and various ions — behaves as a classical monatomic ideal gas.

- The partial pressures $p_i = n_i kT$ due to each species simply add to yield the total hydrodynamic pressure $p = nkT$, with $n = \sum_i n_i$. The ideal gas law can be expressed in terms of the hydrodynamic mass density ρ as

$$p = \frac{\rho}{\bar{m}} kT, \quad (2.25)$$

where $\bar{m} = n^{-1} \sum_i m_i n_i$ is the mean particle mass of all plasma species, each species having a number density n_i and mass m_i .

- The enthalpy is given by

$$h = \frac{\gamma}{\gamma - 1} \frac{p}{\rho} = \frac{\gamma}{\gamma - 1} \frac{kT}{\bar{m}} = c_p T. \quad (2.26)$$

The first equality follows from the thermodynamic definition of enthalpy, $h \equiv \mathcal{E} + p/\rho$, and the ideal fluid equation of state, (2.24), the second equality from the previous bullet, and the third equality from the next bullet.

- The adiabatic index, γ , is the ratio of specific heats, c_p and c_v , which are both constant. That c_v is constant follows from its thermodynamic definition, $c_v \equiv (\partial \mathcal{E} / \partial T)_V$, since as a result of the first bullet and (2.24), $\mathcal{E} = (kT/\bar{m})/(\gamma - 1)$, giving $c_v = (\partial \mathcal{E} / \partial T)_V = (k/\bar{m})/(\gamma - 1)$. Similarly, c_p is constant because from (2.26) and its thermodynamic definition, $c_p \equiv (\partial h / \partial T)_p$, we have $c_p = [\gamma/(\gamma - 1)]k/\bar{m}$. Their ratio is therefore $c_p/c_v = \gamma$.
- While this follows from the previous bullet, it is worth pointing out separately that since $c_v = (\partial \mathcal{E} / \partial T)_V$ is constant,

$$\mathcal{E} = c_v T. \quad (2.27)$$

- Monatomic gases have $\gamma = 5/3$. From statistical physics we know that each degree of freedom has $kT/2$ units of energy, so every particle in the fluid element has internal energy per unit mass $\mathcal{E} = (3/2)kT/\bar{m}$. Equating $c_v = (3/2)k/\bar{m}$ with the relation found in the third bullet, $c_v = (k/\bar{m})/(\gamma - 1)$, we obtain $\gamma = 5/3$.

The partially ionized gases considered in this work will be modeled assuming these relations for a fully ionized gas hold. We therefore briefly comment on what this assumption entails. First, in the presence of multiple transient species (created as the result of photoionizations and recombinations,

for example), the 1st law of thermodynamics is really

$$\delta Q = d\mathcal{E} + p d\mathcal{V} + \sum_i \alpha_i dN_i, \quad (2.28)$$

where α_i is the chemical potential and N_i the number of particles of each species in the fluid element. There are two justifications for neglecting the contribution of $\alpha_i dN_i$ to the energy balance: (i) since AGN gas is mostly hydrogen, this contribution for each newly excited/ionized species of metal ion will be small owing to their small abundance; (ii) because photoionization equilibrium likely holds to a good approximation, the N_i of the dominant species (i.e. hydrogen nuclei and free electrons) should be nearly constant owing to a detailed balance argument and thus $dN_i \approx 0$.

Second, referring to the last bulleted property for a monatomic gas, a partially ionized gas will have $\gamma < 5/3$. This is because the internal energy per unit mass is greater than $(3/2)kT/\bar{m}$ due to the internal degrees of freedom associated with excitation and ionization. For this reason, we will retain γ in all of our expressions, although our numerical results have been calculated assuming $\gamma = 5/3$. Since it is possible to show that partially ionized gases obey $\gamma > 4/3$, there is only a small range of parameter space to explore and our results will not qualitatively change in this range.

2.1.5 Entropy generation

Notice that the energy equation was derived without reference to entropy, which enters from the 2nd law of thermodynamics, $\delta Q = T ds$, where s is the entropy per unit mass of the fluid element. We can write two equations for entropy, and they have entirely different meanings. From the 1st law of thermodynamics, (2.14), we have

$$T ds = d\mathcal{E} + p d(1/\rho). \quad (2.29)$$

From (2.15), meanwhile,

$$\rho T ds = (\rho \dot{q} - \nabla \cdot \mathcal{H}) dt. \quad (2.30)$$

The second equation is an evolution equation for entropy, and ds/dt should be associated with the comoving frame derivative. Using again $\dot{q} = -\mathcal{L}$, we have

$$\rho T \frac{Ds}{Dt} = -\rho \mathcal{L} - \nabla \cdot \mathcal{H}. \quad (2.31)$$

Clearly, the flow can evolve adiabatically only if $\rho\mathcal{L} = -\nabla \cdot \mathcal{H}$ everywhere, and in an idealized steady state case this can occur for clouds, as discussed below in §2.2.1. In general, however, the r.h.s heating terms act as sources of entropy.

The first equation relates entropy to our hydrodynamic variables. Using the results derived above in §2.1.4, we can arrive at $s = c_v \ln(p/\rho^\gamma) + s_0$ (with s_0 a constant) as follows:

$$\begin{aligned}
ds &= c_v \frac{dT}{T} - \frac{p}{\rho T} \frac{d\rho}{\rho} \\
&= c_v d \ln T - \frac{k}{m} d \ln \rho \\
&= c_v (d \ln p - d \ln \rho) - c_v (\gamma - 1) d \ln \rho \\
&= c_v [d \ln p - d \ln \rho^\gamma] \\
\Rightarrow s &= c_v \ln(p/\rho^\gamma) + s_0.
\end{aligned} \tag{2.32}$$

This relationship, combined with the above found relation for c_v , allows (2.30) to be expressed instead as,

$$\frac{P}{\gamma - 1} \frac{D}{Dt} \ln \left(\frac{P}{\rho^\gamma} \right) = -\rho\mathcal{L} - \nabla \cdot \mathcal{H}, \tag{2.33}$$

a form of the energy equation that commonly appears in analytic investigations in the literature.

Solving for pressure in terms of entropy gives

$$p = \exp \left(\frac{s - s_0}{c_v} \right) \rho^\gamma = K(s) \rho^\gamma. \tag{2.34}$$

Incidentally, the second equality shows that for adiabatic flow, an ideal equation of state has the form of a polytropic equation of state, $p = K\rho^\gamma$. We report this equation because it allows us to evaluate the adiabatic sound speed in an ideal gas, whose thermodynamic definition is $c_s^2 \equiv (\partial p / \partial \rho)_s$. Thus,

$$c_s = \sqrt{\frac{\gamma p}{\rho}}. \tag{2.35}$$

We will return to discussing entropy in Chapter 4 when we examine Balbus' criterion for thermal instability.

2.1.6 Vorticity generation

No chapter discussing multi-dimensional gas dynamics would be complete without some discussion of vorticity, which is just the curl of the velocity field, $\boldsymbol{\omega} = \nabla \times \boldsymbol{v}$. That this quantity is so basic

to fluid dynamics becomes apparent upon recognizing that the nonlinear term in Euler's equation, $\mathbf{v} \cdot \nabla \mathbf{v}$, can be decomposed into a 'potential flow' term and a term involving vorticity:

$$\mathbf{v} \cdot \nabla \mathbf{v} = \nabla \frac{v^2}{2} + (\nabla \times \mathbf{v}) \times \mathbf{v}. \quad (2.36)$$

Most analytic investigations have not probed deeply enough into the nonlinear regime for vorticity to play a central role in how clouds evolve, but our numerical results will reveal that vorticity governs cloud dynamics. An evolution equation for $\boldsymbol{\omega}$ is found by taking the curl of (2.7) after substituting in (2.36):

$$\begin{aligned} \frac{\partial \boldsymbol{\omega}}{\partial t} + \nabla \times (\boldsymbol{\omega} \times \mathbf{v}) &= -\nabla \times \left(\frac{\nabla p}{\rho} \right) + \sum_i \nabla \times \mathbf{f}_i \\ &= \frac{\nabla \rho \times \nabla p}{\rho^2} + \sum_i \nabla \times \mathbf{f}_i. \end{aligned} \quad (2.37)$$

The terms on the r.h.s are sources of vorticity, since we know by Kelvin's circulation theorem that the vortex lines threading a fluid element are conserved with time when the r.h.s is 0. For compressible flow subject to body forces, therefore, the only way to *not* generate vorticity with time is if all body forces are derivable from a potential ($\mathbf{f}_i = \nabla \phi_i$) and either one of the following two special conditions holds: (i) the flow is barotropic with $p = p(\rho)$ only, in which case ∇p is parallel to $\nabla \rho$; (ii) the r.h.s of (2.31) is zero, so the flow is isentropic with $Ds/Dt = 0$, which implies $\nabla h = \rho^{-1} \nabla p$ and hence that $\nabla \times (\rho^{-1} \nabla p) = 0$ in the first equality above. That isentropic flows obey $\nabla h = \rho^{-1} \nabla p$ can be shown by noting that $dh = d\mathcal{E} + dp/\rho - (p/\rho^2)d\rho$ by its definition (see the third bullet above), which means $dh = T ds + dp/\rho$ by (2.29).

In general, the heating terms will not balance to make the flow isentropic and (2.18) shows that $\mathcal{E} \neq \mathcal{E}(\rho)$ only and hence $p \neq p(\rho)$ by (2.24). Moreover, radiation forces cannot be expressed as the gradient of a potential. The inescapable conclusion is that vorticity generation will lead to a turbulent flow regime as clouds evolve under the influence of a realistic AGN radiation field.

2.1.7 Eulerian equations summarized

To summarize, we began with a Lagrangian viewpoint, writing down the governing equations in the comoving frame of a fluid element, and then derived the Eulerian equations of hydrodynamics in conservation form:

$$\frac{\partial \rho}{\partial t} + \nabla \cdot (\rho \mathbf{v}) = 0 \quad (2.38)$$

$$\frac{\partial \rho \mathbf{v}}{\partial t} + \nabla \cdot (\rho \mathbf{v} \mathbf{v} + p \mathbb{I}) = \sum_i \mathbf{f}_i \quad (2.39)$$

$$\frac{\partial}{\partial t} \left(\rho \mathcal{E} + \frac{\rho v^2}{2} \right) + \nabla \cdot \left[\left(\rho \mathcal{E} + \frac{\rho v^2}{2} + p \right) \mathbf{v} \right] = -\rho \mathcal{L} - \nabla \cdot \mathcal{H} + \sum_i \mathbf{f}_i \cdot \mathbf{v}. \quad (2.40)$$

The presence of the conduction term means that we are considering a non-perfect fluid, the absence of viscosity signifies an inviscid fluid, and the equation of state $p = \rho \mathcal{E}(\gamma - 1)$ is that for an ideal fluid. We will solve these equations assuming a monatomic ideal gas, which has $p = nkT$, $\mathcal{E} = c_v T$, and $\gamma = 5/3$.

2.2 Gas dynamics of clouds: simple examples

To illustrate that the subject of AGN clouds offers a fascinating glimpse into the physics emerging from the equations of gas dynamics, consider the fact that the three most famous partial differential equations (PDEs) of mathematical physics (i.e. parabolic, hyperbolic, and elliptic PDEs) all readily appear when studying clouds in various simplified contexts.

2.2.1 A Parabolic PDE: cloud equilibria

Recall from §1.4.3 Begelman & McKee's (1990) basic result that large clouds, those with a characteristic size $R_C \gg \lambda_F$, are not subject to evaporation. The cold gas can reach a thermal equilibrium state with its surrounding warmer environment when radiative losses balance the diffusive flow of heat through the cloud interfaces. Assuming a perfectly static cloud, the approach to equilibrium is governed only by (2.40), which is reduced to

$$\frac{\partial \mathcal{E}}{\partial t} = -\rho \mathcal{L} - \nabla \cdot \mathcal{H}. \quad (2.41)$$

Using $\mathcal{E} = c_v T$ and Fourier's law for the heat flux, $\mathcal{H} = -\kappa(T) \nabla T$, (2.41) becomes the inhomogeneous heat equation,

$$\frac{\partial T}{\partial t} - \frac{1}{c_v} \nabla \cdot [\kappa(T) \nabla T] = -\frac{\rho \mathcal{L}}{c_v}. \quad (2.42)$$

This is a nonlinear parabolic PDE in general due to the dependence of κ on temperature. Deep in the core of the cloud, the net radiative losses can be negligible ($\mathcal{L} \approx 0$), as cooling is strong only in the cloud interfaces. The approach to equilibrium is then solely done through heat diffusion, and in the steady state ($\partial T / \partial t = 0$) the cloud core will reach a constant temperature. Out in the intercloud

medium, however, radiative heating typically still takes place, and in the steady state $\nabla \cdot \mathcal{H} = -\rho\mathcal{L}$ instead. This balance stands in contrast to the assumption made in the standard two-phase model that radiative equilibrium ($\mathcal{L} = 0$) is reached by the hot phase (recall §1.4.2). It therefore has implications for the temperature of any confining medium in AGN, as radiative equilibrium leads to Compton temperatures being reached, but lower temperatures result from $\nabla \cdot \mathcal{H} = -\rho\mathcal{L}$.

2.2.2 A Hyperbolic PDE: cloud formation

This next example is borrowed from problem set 3 in Shu's text on gas dynamics (Shu 1991). Linearizing equations (2.38)-(2.40) (as carried out in Chapter 4) followed by some further manipulations outlined in the problem set brings one to

$$\frac{\partial}{\partial t} \left(\frac{\partial^2 \rho_1}{\partial t^2} - c_{s,0}^2 \nabla^2 \rho_1 \right) = N_p c_{s,0}^2 \nabla^2 \rho_1 - N_v \frac{\partial^2 \rho_1}{\partial t^2}, \quad (2.43)$$

where ρ_1 is the density perturbation, $c_{s,0} = \sqrt{\gamma p_0 / \rho_0}$ is the sound speed in the unperturbed flow, and we have denoted

$$N_p \equiv \frac{1}{c_p} \left(\frac{\partial \mathcal{L}}{\partial T} \right)_p, \quad N_v \equiv \frac{1}{c_v} \left(\frac{\partial \mathcal{L}}{\partial T} \right)_\rho. \quad (2.44)$$

Equation (2.43) is a 3rd order homogenous PDE and constitutes a generalized wave equation governing the behavior of waves in a perfect fluid (we are neglecting the conduction term here) subject to bulk heating and cooling. This PDE is nonlinear since realistic cooling functions make N_p and N_v nonlinear functions of T and ρ , but we recover the classic 2nd order, linear wave equation describing adiabatic sound waves when the r.h.s is zero. In reality sound waves do not remain adiabatic; they lose energy and damp out somewhat as they propagate, and this is captured by (2.43). The N 's are inverse cooling timescales. The larger these timescales are, the longer it takes the waves to dissipate.

Thus far we have not made the connection to thermal instability and therefore cloud formation. Notice that there are two instances in which the sound speed drops out of (2.43), leaving only non-propagating disturbances: (i) when $\nabla \rho_1$ is very small, corresponding to spatially large disturbances over which density changes gradually and (ii) the opposite case with very large $\nabla \rho_1$, meaning small scale disturbances. In case (i), sound waves will not be able to propagate across the disturbance to maintain pressure equilibrium and we are left with an equation involving the cooling time at constant volume, $1/N_v$,

$$\frac{\partial \rho_1}{\partial t} + N_v \rho_1 = 0. \quad (2.45)$$

The solution to this equation, $\rho_1 = \exp(-N_v t)$, shows that the perturbation grows exponentially with time when $N_v < 0$, i.e. when $(\partial\mathcal{L}/\partial T)_\rho < 0$. This is the isochoric version of thermal instability first identified by Parker (recall the discussion in Chapter 1).

In case (ii), sound waves can maintain pressure equilibrium across the disturbance and the equation this time,

$$\frac{\partial\rho_1}{\partial t} + N_p\rho_1 = 0, \quad (2.46)$$

has a solution that again grows exponentially, $\rho_1 = \exp(-N_p t)$, but now corresponds to Field's criterion for isobaric thermal instability, $(\partial\mathcal{L}/\partial T)_p < 0$. In either case the disturbances will become clouds once their amplitudes become nonlinear, at which point (the linearized equation) (2.43) no longer applies to determine their evolution. Chapter 5 is dedicated to understanding the outcome of this case.

It has recently been shown that the nonlinear evolution of case (i) is also quite interesting, as this one very large disturbance that is out of pressure equilibrium may, after becoming a large cloud, 'shatter' into a 'mist' of very small clouds (McCourt et al. 2016). Each one would have a size on the order of c_s/N_v (with c_s being the sound speed inside the cloud), so that pressure equilibrium can now be maintained. The subsequent evolution of the individual clouds resulting from this fragmentation process should then suffer the same general fate as the case (i) clouds discussed in Chapter 5.

2.2.3 An Elliptic PDE: cloud evaporation

The final example is taken from Balbus (1985). We seek a global steady state solution consisting of hot gas in pressure equilibrium with a possibly large number of small embedded cool clouds of arbitrary shape. As discussed in Chapter 1, for clouds smaller than the Field length, the conduction term will dominate the cooling term on the r.h.s of (2.40). Then the Eulerian equations reduce to

$$\begin{aligned} \nabla \cdot (\rho \mathbf{v}) &= 0, \\ \mathbf{v} \cdot \nabla \mathbf{v} &= 0, \\ \nabla \cdot \left[\left(\mathcal{E} + \frac{1}{2}\rho v^2 + p \right) \mathbf{v} + \mathcal{H} \right] &= 0. \end{aligned} \quad (2.47)$$

For an ideal fluid equation of state with $\gamma = 5/3$ and a realistic conductivity, $\kappa = \chi T^{5/2}$, with χ a constant, we can write the energy equation as

$$\nabla \cdot \left[\left(\frac{5}{2}p + \frac{1}{2}\rho v^2 \right) \mathbf{v} - \chi T^{5/2} \nabla T \right] = 0. \quad (2.48)$$

The ratio of the two terms in parenthesis is $v^2/(5p/\rho) = M^2/3$, where $M = v/c_s$ is the Mach number. If we therefore restrict our attention to highly subsonic flow, then this equation is a statement of balance between thermal expansion (i.e. adiabatic cooling) and conductive heating. Since we assumed $p = \text{constant}$, we can write

$$\nabla \cdot \left[\mathbf{v} - \frac{2\chi}{5p} T^{5/2} \nabla T \right] = 0. \quad (2.49)$$

We have therefore found a global solution to the velocity field in terms of the temperature,

$$\begin{aligned} \mathbf{v} &= \frac{2\chi}{5p} T^{5/2} \nabla T + \nabla \times \boldsymbol{\alpha} \\ &= \frac{4}{25} \frac{\chi}{p} T \nabla T^{5/2} + \nabla \times \boldsymbol{\alpha}, \end{aligned} \quad (2.50)$$

where in general, this velocity field can have vorticity $\boldsymbol{\omega} = \nabla \times \boldsymbol{\alpha}$ and still satisfy (2.49). Considering only irrotational flow, we notice by the second equality above that multiplying \mathbf{v} by ρ cancels the factor of T , giving the mass flux,

$$\rho \mathbf{v} = \frac{4}{25} \frac{\bar{m}}{k} \chi \nabla T^{5/2}. \quad (2.51)$$

The continuity equation then reveals that the temperature distribution satisfies a Laplace equation,

$$\nabla^2 T^{5/2} = 0. \quad (2.52)$$

Thus, $T^{5/2}$ behaves like a potential, Φ . Exploiting the analogy with electrostatics, we see that $\rho \mathbf{v} \propto \nabla T^{5/2}$ plays the role of an electric field, $\mathbf{E} = -\nabla \Phi$. Hence, Gauss' law can be used to determine the mass flux, i.e. the evaporation rate, from this arbitrary cloud distribution. Specific examples and further analogies with electrostatics are presented by Balbus & Potter (2016).

2.2.4 Summary

These simple examples serve to make several points. First, well designed thought experiments can probe individual aspects of the gas dynamics of clouds. Historically, this is how our understanding has developed. Second, the dynamics of real AGN clouds is necessarily complicated, as one can easily imagine a scenario in which clouds form, equilibrate, and evaporate in an evolving, time-dependent fashion. Indeed, the solutions we find in Chapter 5 and 6 demonstrating the role of cloud acceleration is a realization of such a scenario. Our third point is simply to assert that a complete theory of the gas dynamics in AGN, despite being complicated, is encapsulated by the equations of hydrodynamics. These are, of course, coupled sets of nonlinear PDEs of mixed type, and the complexity of their solutions automatically suggests that AGN clouds are highly dynamical entities. As we mentioned at the beginning of this chapter, a truly comprehensive model of AGN gas dynamics may possibly require solving a much more complicated set of equations. Even so, the solutions presented in this thesis represent the groundwork and are necessary stepping stones to finding and understanding such advanced solutions.

Chapter 3

RADIATION SOURCE TERMS

In the previous chapter we derived the conservation form of the Eulerian equations of hydrodynamics including energy and momentum source terms. Specifically, we allowed for an arbitrary number of body forces in the momentum equation (and their contribution to the energy equation), a conductive heat flux, and a generic volumetric energy deposition (or loss) function, $\dot{q} = -\mathcal{L}$, in the energy equation. The conduction term is needed to account for the flow of heat (mediated by free electrons) from the hot intercloud medium through the interfaces of the cloud. In this chapter we derive the radiative source terms — the body force and the individual contributions to \mathcal{L} — associated with the matter interactions with the radiation field.

3.1 Derivation using radiative transfer theory

We picture a parcel of gas located very far from the central engine so that we can consider the background source of radiation to be plane parallel. In the absence of matter, the radiation field due to the AGN is therefore highly anisotropic. In the presence of matter, the radiation field is unknown but can be determined by solving the radiation transport equation. Both the frequency-dependent absorptivity of the gas, k_ν (with units cm^{-1}), and the emissivity of the gas, j_ν (with units $\text{erg cm}^{-3} \text{s}^{-1} \text{rad}^{-1} \text{Hz}^{-1}$), must be given. The resulting radiation field, characterized by its specific intensity, I_ν (with units $\text{erg cm}^{-2} \text{s}^{-1} \text{rad}^{-1} \text{Hz}^{-1}$), then gives rise to both a body force and volumetric heating and cooling rates.

A formal development of these source terms proceeds not by accounting for the energy gains and losses to the parcel of gas but rather to the radiation field itself. Namely, the absorptivity and the emissivity serve to track the intensity removed from or added to a beam of radiation that would otherwise maintain its specific intensity in passing through the matter. This is the essence of the radiation transport equation,

$$\frac{1}{c} \frac{\partial I_\nu}{\partial t} + \mathbf{n} \cdot \nabla I_\nu = j_\nu - k_\nu I_\nu. \quad (3.1)$$

The factor of $1/c$ in this equation appears because, if it were possible to boost into the comoving frame of the radiation (a purely non-relativistic notion), (3.1) could be written $DI_\nu/Dt = 0$ when

$j_\nu = k_\nu = 0$ since $D/Dt = \partial/\partial t + c \mathbf{n} \cdot \nabla$ for radiation.

The specific intensity is defined in terms of the energy ΔE of a small parcel of radiation (i.e. a bundle of photons) within the entire radiation field,

$$\Delta E = I_\nu A \Delta \Omega \Delta t \Delta \nu, \quad (3.2)$$

where A is the cross-sectional area of the parcel. This is equivalent to

$$\frac{\Delta E}{V} = \frac{I_\nu}{c} \Delta \Omega \Delta \nu, \quad (3.3)$$

where $V = A(c \Delta t)$ is the volume of the parcel, so that I_ν/c measures radiation *energy density* per unit solid angle, per unit frequency. The specific intensity is thus a seven-dimensional quantity, depending on three position coordinates for the location in question, two angular coordinates for the direction of propagation, time, and frequency. An eighth coordinate is needed to track polarization. Solving the full equations of radiation hydrodynamics (RHD) requires keeping track of at least 6 of these coordinates. That is, in the gray approximation, the frequency dependence is integrated out entirely, while in multi-group methods, only finite ‘groups’ of spectral bands, $\Delta \nu$, are considered. In coupling this equation with the Eulerian equations, however, the solid angle dependence can also be integrated out, for we can ignore the directions from which heat was deposited or flows out of our fluid elements when solving for the gas dynamics. The radiation source terms therefore arise by integrating (3.1) over solid angle, a procedure analogous to taking moments over the velocity distribution of particles to derive the fluid equations from kinetic theory.

3.1.1 Radiation moment equations

The subtleties involved in taking moments are well described in Castor’s text, which we follow here. We first make reference to a Cartesian coordinate system, in which the direction of propagation, \mathbf{n} , not only points in a fixed direction, but is also constant with respect to the coordinates. This allows us to invoke a product rule to exchange the dot product in (3.1) with a divergence term,

$$\frac{1}{c} \frac{\partial I_\nu}{\partial t} + \nabla \cdot (\mathbf{n} I_\nu) = j_\nu - k_\nu I_\nu. \quad (3.4)$$

The frequency-integrated zero-order moment of I_ν is found by first integrating this equation over the solid angle, Ω , and then over frequency:

$$\frac{\partial E}{\partial t} + \nabla \cdot \mathbf{F} = \int d\nu (4\pi j_\nu - k_\nu c E_\nu), \quad (3.5)$$

where $E = \int d\nu \int (I_\nu/c) d\Omega$ and $\mathbf{F} = \int d\nu \int \mathbf{n} I_\nu d\Omega$ are the total radiation energy density and the vector flux of radiation, respectively.¹ Here we have assumed that the emissivity and absorptivity are both isotropic. This explains the factor of 4π in front of j_ν , whereas there is no such factor for k_ν because $E_\nu = \int d\Omega (I_\nu/c)$ contains the solid angle integral. For a non-magnetized gas, there is no preferred orientation of the atoms, so the isotropy assumption for k_ν is easily justified for absorption by the continuum. The emissivity contribution from scattered radiation will be anisotropic if I_ν is anisotropic, and since line driving is a scattering process, the radiation force term derived below cannot describe the line force. We will therefore treat it separately in §3.2.3. Furthermore, note that Doppler shifts will also make the non-scattering (e.g., thermal emission) contributions to j_ν anisotropic in general. Since our results reveal that AGN clouds accelerate very slowly and move subsonically with respect to their surroundings, this anisotropy is likely negligible. In any case, the line profile calculations carried out in Chapter 7 account for Doppler shifts a posteriori.

The frequency-integrated first-order moment of I_ν follows by multiplying (3.4) by \mathbf{n} before integrating over solid angle and frequency. Noting that \mathbf{n} can be brought into the divergence term due to our implicit use of Cartesian coordinates, we have

$$\frac{1}{c} \frac{\partial \mathbf{F}}{\partial t} + c \nabla \cdot \mathbb{P} = - \int d\nu k_\nu \mathbf{F}_\nu, \quad (3.6)$$

where $\mathbb{P} = \int d\nu \int \mathbf{n} \mathbf{n} (I_\nu/c) d\Omega$ is the radiation pressure tensor and $\mathbf{F}_\nu = \int \mathbf{n} I_\nu d\Omega$. There is no term for j_ν on the r.h.s because $\int j_\nu \mathbf{n} d\Omega = j_\nu \int \mathbf{n} d\Omega = 0$, a result that again depends on j_ν being isotropic. In deriving the RHD equations, this moment equation gets added to the Eulerian momentum equation, but it does not yet have units of momentum density. Since \mathbf{F}/c has units of energy density, we must divide by another factor of c .

First, we need to formally manipulate the r.h.s to arrive at something that looks like a traditional radiation force. The standard approach is to define some type of mean opacity that contains the

¹Note that E is related to the mean intensity, $J = (4\pi)^{-1} \int d\nu \int I_\nu d\Omega$, as $E = 4\pi J/c$, and that the flux is often written as a scalar by measuring it with respect to the direction normal to the surface of the parcel of radiation, \mathbf{k} . That is, $F = \int d\nu \int \mathbf{k} \cdot \mathbf{n} I_\nu d\Omega = \int d\nu \int I_\nu \cos \theta d\Omega$, where θ is the direction between \mathbf{k} and \mathbf{n} .

integral over frequency, but this offers many possibilities because the flux is also frequency-dependent in general. Our approach is to split the radiation field into N groups such that in any group i , $\mathbf{F}_{\nu,i} = \mathbf{F}_i/\Delta\nu_i$ is a constant, allowing us to write

$$\int d\nu k_\nu \mathbf{F}_\nu = \sum_{i=1}^N \frac{1}{\Delta\nu_i} \mathbf{F}_i \left(\int d\nu k_\nu \right)_i. \quad (3.7)$$

By defining the mean opacity in each group as

$$\kappa_i = \frac{1}{\rho \Delta\nu_i} \left(\int k_\nu d\nu \right)_i, \quad (3.8)$$

where ρ is the mass density of the fluid, we obtain the radiation force in the form

$$\mathbf{f}_{rad} = \sum_{i=1}^N \frac{\kappa_i \rho \mathbf{F}_i}{c}. \quad (3.9)$$

With these definitions, our second moment equation becomes

$$\frac{\partial \mathbf{F}}{\partial t c^2} + \nabla \cdot \mathbb{P} = -\mathbf{f}_{rad}. \quad (3.10)$$

At this point, it is no longer necessary to implicitly consider Cartesian coordinates since the two moment equations (3.5) and (3.10) appear in coordinate-free form.

3.1.2 The body force due to radiation

Equation (3.9) provides our sought after body force. The negative sign in (3.10) arises because photons that are lost in imparting momentum to the gas constitute a sink for the radiation momentum density, \mathbf{F}/c^2 . Now, it was mentioned that the RHD momentum equation is derived by adding together (3.10) and (2.39), which would mean that the body force \mathbf{f}_{rad} on the r.h.s of (2.39) cancels with the r.h.s of (3.10), leaving

$$\frac{\partial}{\partial t} \left(\rho \mathbf{v} + \frac{\mathbf{F}}{c^2} \right) + \nabla \cdot (\rho \mathbf{v} \mathbf{v} + p \mathbb{I} + \mathbb{P}) = 0. \quad (3.11)$$

This is in fact the correct RHD momentum conservation equation. We therefore see what must be true if we are to recover the Eulerian momentum equation from (3.11): the radiation field must be time-independent (i.e. $\partial \mathbf{F}/\partial t = 0$), such that we can move $\nabla \cdot \mathbb{P}$ to the r.h.s and then use the fact

that $-\nabla \cdot \mathbb{P} = \mathbf{f}_{rad}$ according to (3.10).

Note again that the expression for \mathbf{f}_{rad} involves only absorption opacity, whereas there will also be a force contribution due to scattering opacity. While a more complicated derivation can account for scattering processes, we opted for the conventional treatment in which this force is calculated separately (see §3.2.3).

3.1.3 Heating and cooling term

The emissivity, which quantifies the rate at which gas radiatively cools, represents a source term for the radiation energy density according to the zero-order moment equation, (3.5), whereas the absorptivity (times the flux) determines the heating rate of the gas and is a sink term for the radiation field. We therefore recognize that the r.h.s of (3.5) represents a *net cooling* volumetric source term,

$$\rho\mathcal{L} = \int d\nu (4\pi j_\nu - k_\nu c E_\nu). \quad (3.12)$$

In the next section we will need the heating contribution to $\rho\mathcal{L}$, which we denote as $\rho\Gamma = \int d\nu k_\nu c E_\nu$. To be consistent with (3.7), we can break this heating rate up into that coming from many frequency groups:

$$\Gamma = \sum_{i=1}^N \Gamma_i = \rho^{-1} c \sum_{i=1}^N E_i \Delta\nu \left(\int d\nu k_\nu \right)_i = c \sum_{i=1}^N E_i \kappa_i = 4\pi \sum_{i=1}^N J_i \kappa_i, \quad (3.13)$$

where κ_i is the mean opacity defined in (3.8) and $J_i = E_i c/4\pi$ is the mean intensity (recall the footnote above). Note that Γ has units of $\text{erg g}^{-1} \text{s}^{-1}$.

As before, (3.5) gets coupled to the Eulerian energy equation by first identifying $\rho\mathcal{L}$ in (3.12) as being the same as the ‘ $\rho\mathcal{L}$ ’ in (2.40) (which recall represented a generic volumetric source term) and then adding together these equations. The source term is again cancelled out, giving the RHD energy equation in conservative form (including conduction) as

$$\frac{\partial}{\partial t} \left(\rho\mathcal{E} + \frac{\rho v^2}{2} + E \right) + \nabla \cdot \left[\left(\rho\mathcal{E} + \frac{\rho v^2}{2} + p \right) \mathbf{v} + \mathbf{F} \right] = -\nabla \cdot \mathcal{H} + \mathbf{f}_{rad} \cdot \mathbf{v}. \quad (3.14)$$

Notice that we are left with the work term due to the radiation force, $\mathbf{f}_{rad} \cdot \mathbf{v} = \sum_i \kappa_i \rho (\mathbf{F}_i \cdot \mathbf{v})/c$, on the r.h.s. To actually see this term arise from the moment equations (as here it came from the Eulerian equations) requires a more formal development of the RHD equations using the comoving frame

picture (see Ch. 6 of Castor’s text, for example). When the radiation field is time-independent, this term is negligible in subsonic flow under most circumstances, which is why it was not included in Proga & Waters (2015) — see Chapter 5. However, in Waters & Proga (2016) we considered a *time-dependent* radiation field and this work term was found to be non-negligible — see Chapter 6.

In a similar fashion to before, we formally recover the Eulerian energy equation by taking $\nabla \cdot \mathbf{F}$ to the r.h.s in (3.14) and letting the radiation field be time-independent ($\partial E/\partial t = 0$). Then from (3.5), we identify $-\nabla \cdot \mathbf{F} = -\rho\mathcal{L}$, as required.

3.2 Sources of opacity

The radiation force in (3.9) applies to both free-free and bound-free opacities, whereas we have emphasized that line scattering (a bound-bound process) is highly anisotropic and so we would need to return to (3.4) and drop the assumption of isotropy in j_ν to derive the force due to bound-bound opacity from first principles. We would find that the scattering contribution to j_ν is flux-dependent and can be grouped with k_ν , but being anisotropic it cannot be pulled outside the solid angle integral. This makes determining the line force very difficult in general, as the bound-bound opacity must be retained in all integrals over sources of continuum emission (for an example of computing the line force due to an accretion disk, see the appendix of Proga, Stone, & Drew 1998). Moreover, both the bound-free and bound-bound opacities themselves are difficult to obtain, as they depend on the level populations of the atoms or ions and on the individual ionization potentials/oscillator strengths of each of those levels. To estimate these opacities, the approach typically taken is to run separate photoionization calculations that provide all of the atomic data. Here we assume such data is given and proceed to identify these individual opacities.

3.2.1 Free-free

For the simple case of electron scattering involving non-relativistic electrons (i.e. for temperatures satisfying $kT \ll m_e c^2$), the only atomic data we need are the elemental abundances, as the cross section is given by the classical formula,

$$\sigma_e = \frac{8\pi}{3} r_e^2, \tag{3.15}$$

where $r_e = e^2/m_e c^2$ is the classical electron radius. The electron scattering opacity is related to σ_e as $\kappa_e = \sigma_e/\bar{m}$, where $\bar{m} = \mu m_p$ is the mean particle mass, which can easily be determined from the abundances.

3.2.2 Bound-free

The source of line emission in the broad and narrow line regions of AGN is photoionized gas. For a given temperature, photon flux, and number density, photoionization codes such as CLOUDY and XSTAR calculate the heating rate due to photoionization. This heating rate is typically output in the same units as the Γ we defined above ($\text{erg g}^{-1} \text{s}^{-1}$) or in units of $\text{erg cm}^3 \text{s}^{-1}$, in which case we label the rate as G . Equation (3.13) allows us to derive the opacity from this heating rate. If frequency dependent output can be extracted, then N can be chosen large enough so that the sum accurately captures the shape of the ionizing portion of the input SED. The bound-free opacity in each frequency group will then be given by

$$\kappa_i = \frac{\Gamma_i}{4\pi J_i} = \frac{n}{\bar{m}} \frac{G_i}{4\pi J_i}, \quad (3.16)$$

where n is the gas number density.

It should be remarked that this is not a fully self-consistent way to determine the bound-free opacity. The background radiation field is an input to CLOUDY or XSTAR and the local radiation field an output. The radiation transfer problem solved by these codes is decoupled from the hydrodynamics and therefore the level populations and heating rates are only approximations. Nevertheless, this approach allows us to proceed in investigating the gas dynamics.

3.2.3 Bound-bound

Line opacity is by far the most important source of opacity for temperatures permitting a few strong UV lines to exist (e.g., Gayley 1995). Resonance line opacity calculations, following the standard approach developed first by Castor, Abbot, & Klein (1975; CAK hereafter), are handled somewhat differently than standard continuum opacity calculations, but at the end of the day one is still left with an effective opacity when summing over all lines. This effective scattering opacity is encapsulated in the so-called force multiplier. We follow a modified CAK method to determine this force multiplier, as detailed in Chapter 5.

Chapter 4

LINEAR THEORY

In this chapter we present a local stability analysis of the equations of hydrodynamics, showing how thermal instability (TI) arises. A brief introduction to Lagrangian perturbations is provided, which we will use to understand the essence of TI and derive Balbus' generalization of Field's criterion. Using Eulerian perturbations, we uncover the dispersion relation for TI, generalizing the analysis of Field (1965) to allow for a background flow that is out of equilibrium or uniformly moving. We show how the resulting instability criterion reduces to that found by Balbus (1986).

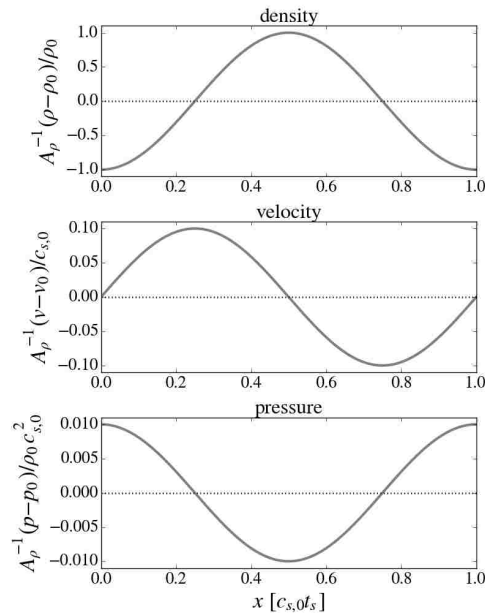


Figure 4.1: Analytic plane-wave solutions of the linearized equations of gas dynamics. Shown are profiles of the perturbations to a thermally unstable uniform background flow, which depend only on the amplitude of the density perturbation, A_ρ , and the ratio of the frequency (growth rate) and wavenumber, σ/k . Here $n/k' \equiv (\sigma/k)/c_{s,0} = 0.1$, where $c_{s,0}$ is the sound speed in the unperturbed flow. Notice the different vertical scales: the pressure perturbation amplitude is n/k' times smaller than that for velocity, which in turn is n/k' times smaller than A_ρ .

Before proceeding, it is useful to state the final results up front. What comes out of linear theory, besides instability criteria and the exponential growth rates, are solutions to the 1D equations of hydrodynamics describing precisely how a cloud can grow from a tiny perturbation. These solutions, namely the actual density, velocity, and pressure profiles, are shown in Figure 4.1. The density profile shows the shape of the perturbation itself, i.e. there is a denser core surrounded by lower density

gas; this profile was chosen to be a cosine function. Linear theory then dictates the waveforms of the velocity and pressure profiles — and they must support cloud growth. Physically, it is clear that for a cloud to grow, gas must be piling into the central density perturbation. Gas to the left must be flowing to the right, i.e. have a positive velocity, while gas to the right must be flowing to the left, i.e. have a negative velocity. The middle panel clearly shows that this physical expectation is indeed the solution. Likewise, the forces must be such to grow the cloud. The pressure force is just $f_{gas} = -dp/dx$ in 1D, and the gas on the left must feel a force to the right, meaning $f_{gas} > 0$ and $dp/dx < 0$, explaining the negative slope in the bottom panel. And vice versa for the gas to the right of the budding cloud.

These profiles maintain their shape as a function of time. The time-dependence in the linear regime is just an exponential growth factor tacked onto *the amplitude* of the spatial profiles because linear theory amounts to looking for such separable solutions. Soon enough the density enhancement becomes comparable to the background density and the neglected nonlinear terms become important. This leads to a *saturation* of the instability and an accompanying change in the profiles. Understanding the nonlinear phase of TI, and what physics must accompany this cloud formation process, is the focus of Chapter 5.

4.1 Eulerian perturbations

The idea behind a formal stability analysis is to linearize the equations of hydrodynamics and then look for instabilities by assuming plane wave solutions to these equations of the form $A \exp(\sigma t + i\mathbf{k} \cdot \mathbf{x})$, where A is the amplitude of the wave, σ is its frequency, and \mathbf{k} the wavenumber. Linear instabilities will appear in the dispersion relations thereby obtained. A dispersion relation relates the growth rate of the instability, now played by σ , to the wavelength of the perturbation $\lambda = 2\pi/k$, where k is the magnitude of \mathbf{k} . The famous classical instabilities of gas dynamics (e.g., Kelvin-Helmholtz, Rayleigh-Taylor, MRI) are all linear instabilities and reveal themselves using this procedure.

Recall that classical perturbation theory involves expanding some unknown quantity q as a perturbation series about some known quantity q_0

$$q = q_0 + \epsilon q_1 + \epsilon^2 q_2 + \dots, \quad (4.1)$$

where the ϵ 's keep track of the order of the approximation. A linear instability analysis will neces-

sarily only involve the $\mathcal{O}(\epsilon)$ terms. Since the ϵ 's are just place markers, we do not need to retain them for $\mathcal{O}(\epsilon)$, and to use notation suggestive of q_1 being a small perturbation we write instead

$$q(\mathbf{x}, t) = q_0(\mathbf{x}, t) + \delta q(\mathbf{x}, t). \quad (4.2)$$

We see that the plane wave ansatz conforms to this formalism if we treat $q_0(\mathbf{x}, t)$ as the ‘background flow’ solution, and $q_1 = \delta q(\mathbf{x}, t)$ contains our wave solution; for scalar fluid variables we write,

$$\delta q = A_q \exp(\sigma t + i\mathbf{k} \cdot \mathbf{x}), \quad (4.3)$$

whereas for vector variables we promote the amplitude to a vector,

$$\delta \mathbf{q} = \mathbf{A}_q \exp(\sigma t + i\mathbf{k} \cdot \mathbf{x}). \quad (4.4)$$

In words, A_q denotes the amplitude of the wave for variable q , while each component of \mathbf{q} will have a different amplitude in general, hence the vector \mathbf{A}_q . Eulerian perturbations commute with both partial time derivatives and the gradient/divergence operators. They do not commute with Lagrangian time derivatives, obeying instead

$$\delta \frac{D}{Dt} = \frac{D}{Dt} \delta + \frac{D}{Dt} (\boldsymbol{\xi} \cdot \boldsymbol{\nabla}) - (\boldsymbol{\xi} \cdot \boldsymbol{\nabla}) \frac{D}{Dt}, \quad (4.5)$$

where $\boldsymbol{\xi}$ is introduced below in §4.2.

4.2 Lagrangian perturbations

The above perturbative approach is an Eulerian one because we have chosen a fixed a position in space, \mathbf{x} , and are comparing the full perturbed solution $q(\mathbf{x}, t)$ with the background flow solution $q_0(\mathbf{x}, t)$, their difference being $\delta(\mathbf{x}, t)$. However, we can equally well consider a series expansion of the position variable (i.e. let $\mathbf{q} = \mathbf{x}$, $\mathbf{q}_0 = \mathbf{x}_0$, and $\mathbf{q}_1 = \boldsymbol{\xi}$),

$$\mathbf{x} = \mathbf{x}_0 + \boldsymbol{\xi}, \quad (4.6)$$

and visualize a fluid element displaced to $\mathbf{x}_0 + \boldsymbol{\xi}$ as a result of a perturbation applied *at an earlier moment in time*. Using a Taylor expansion, we can examine to 1st order the state of the fluid

element at its new position relative to \mathbf{x}_0 , the position it would have been at in the absence of the applied perturbation,

$$q(\mathbf{x}_0 + \boldsymbol{\xi}, t) = q(\mathbf{x}_0, t) + \nabla q(\mathbf{x}_0, t) \cdot \boldsymbol{\xi}. \quad (4.7)$$

Note that the difference $q(\mathbf{x}_0 + \boldsymbol{\xi}, t) - q(\mathbf{x}_0, t)$ is a comparison of *perturbed flow* at $\mathbf{x}_0 + \boldsymbol{\xi}$ with *perturbed flow* at \mathbf{x}_0 since the perturbation was applied in the past. Hence, to make a correspondence with (4.2), we should equate $q(\mathbf{x}_0, t)$ with the perturbed Eulerian solution to give

$$q(\mathbf{x}_0 + \boldsymbol{\xi}, t) = q_0(\mathbf{x}_0, t) + \delta q(\mathbf{x}_0, t) + \nabla q(\mathbf{x}_0, t) \cdot \boldsymbol{\xi}. \quad (4.8)$$

We then define a Lagrangian perturbation, Δq , as the difference between *perturbed flow* at $\mathbf{x}_0 + \boldsymbol{\xi}$ and *unperturbed flow* at \mathbf{x}_0 ,

$$\Delta q \equiv q(\mathbf{x}_0 + \boldsymbol{\xi}, t) - q_0(\mathbf{x}_0, t), \quad (4.9)$$

so that (4.8) becomes the defining relation between Lagrangian and Eulerian perturbations,

$$\Delta q = \delta q + \boldsymbol{\xi} \cdot \nabla q. \quad (4.10)$$

After any small time interval dt , the perturbed fluid element is displaced by a distance $d\boldsymbol{\xi} = \Delta \mathbf{v} dt$ relative to its previous location, meaning that we also have

$$\Delta \mathbf{v} = \frac{D\boldsymbol{\xi}}{Dt}. \quad (4.11)$$

Equating (4.10) and (4.11) reveals a complicated relationship between the Lagrangian displacement vector and the Eulerian velocity perturbation:

$$\delta \mathbf{v} = \frac{\partial \boldsymbol{\xi}}{\partial t} + \mathbf{v} \cdot \nabla \boldsymbol{\xi} - \boldsymbol{\xi} \cdot \nabla \mathbf{v}. \quad (4.12)$$

The Lagrangian approach has the advantage that the operator Δ commutes with the advective derivative, D/Dt (see Lynden-Bell & Ostriker 1967 for a proof), and consequently one can work with the simpler Lagrangian equations. The real power of the Lagrangian approach applied to TI is in its ability to assess local thermal instability in a dynamical setting (e.g., within winds or accretion flows), which often requires abandoning the use of plane wave solutions (Balbus 1988; Balbus & Soker 1989; Balbus 1995). In such dynamical settings where gravity is important, the

gas is stratified and TI becomes intimately connected with convective instability (e.g., Balbus 1995; Moscibrodzka & Proga 2013; Balbus & Potter 2016). These issues will all come into play when modeling cloud dynamics *globally*. For the local simulations developed in this thesis, it suffices to neglect gravity (since it is locally weak compared to radiation forces) and thus a stability analysis using Eulerian perturbations is sufficient for our purposes.

4.3 Informal Lagrangian analysis of TI

The following analysis, due to Balbus (1986; 1995), allows one to arrive at a generalization of Field's criterion for TI using the 2nd law of thermodynamics and Lagrangian perturbations. If we neglect the conduction term in (2.31), the 2nd law becomes simply

$$\frac{Ds}{Dt} = -\frac{\mathcal{L}}{T}. \quad (4.13)$$

Since Δ and D/Dt commute, its perturbed form reads

$$\frac{D\Delta s}{Dt} = -\Delta(\mathcal{L}/T). \quad (4.14)$$

This is equivalent to

$$\frac{D \ln |\Delta s|}{Dt} = -\frac{\Delta(\mathcal{L}/T)}{|\Delta s|}. \quad (4.15)$$

The r.h.s of this equation is ambiguous for sound waves and buoyant oscillations, since they are both adiabatic disturbances and thus $|\Delta s|$ vanishes to first order (see Balbus 1995 for details). For the non-propagating TI mode, however, the r.h.s immediately suggests the instability criterion,

$$\left[\frac{\partial(\mathcal{L}/T)}{\partial s} \right]_q < 0, \quad (4.16)$$

for when this is satisfied, the r.h.s of (4.15) is positive, and the entropy perturbation will grow with time. Here, q is the thermodynamic quantity that remains constant as the perturbation evolves. From Chapter 1, we know that this should be pressure for TI. By the thermodynamic definition of specific heat for constant pressure processes, $c_p \equiv (dq/dT)_p$, we have $Tds = c_p dT$, allowing us to

exchange ∂s for ∂T . This brings us to Balbus' criterion for thermal instability quoted in Chapter 1:

$$\left[\frac{\partial(\mathcal{L}/T)}{\partial T} \right]_p < 0. \quad (4.17)$$

Since kT/\mathcal{L} is a cooling timescale, its inverse is a cooling rate (with units $\text{s}^{-1} \text{g}^{-1}$) and the physical content of this criterion is simple: stability requires the cooling rate to increase as the gas heats up — otherwise TI results.

4.4 Formal Eulerian analysis of TI

The discussion at the end of §4.2 was presented so as to not confuse a dynamical setting — one with significant velocity gradients — with a local region in an outflow, as here we derive a dispersion relation that applies to gas that is potentially highly supersonic. Our generalized dispersion relation holds only for uniform regions of the flow on scales below that where geometrical ‘stretching’ terms caused the divergence of the flow become significant.

We begin by applying the Eulerian perturbation operator, δ , to the equations of gas dynamics. It is simplest to use momentum equation (2.10) and energy equation (2.18) after making use of identity (2.22). Then,

$$\frac{\partial \delta \rho}{\partial t} + \nabla \cdot (\mathbf{v} \delta \rho + \rho \delta \mathbf{v}) = 0 \quad (4.18)$$

$$\frac{\partial}{\partial t} (\mathbf{v} \delta \rho + \rho \delta \mathbf{v}) + \nabla \cdot (\mathbf{v} \mathbf{v} \delta \rho + 2\rho \mathbf{v} \delta \mathbf{v}) + \nabla \delta p = 0 \quad (4.19)$$

$$\begin{aligned} \frac{1}{\gamma - 1} \frac{\partial \delta p}{\partial t} + \frac{1}{\gamma - 1} \nabla \cdot (p \delta \mathbf{v} + \mathbf{v} \delta p) + p \nabla \cdot \delta \mathbf{v} \\ = -\mathcal{L} \delta \rho - \rho \delta \mathcal{L} - \nabla \cdot \delta \mathcal{H}. \end{aligned} \quad (4.20)$$

In (4.20), we have eliminated $\rho \mathcal{E}$ in favor of p using the equation of state. Also, we have neglected the body forces on physical grounds: our initial conditions will assume a highly ionized gas (i.e. gas that occupies the high temperature branch of the radiative equilibrium curve) and the main source of opacity is negligible in this regime, hence so too is the radiation force. Furthermore, with $\mathcal{H} = -\kappa \nabla T$ and assuming $\kappa = \chi T^{5/2}$ with χ a constant, we formally have

$$\delta \mathcal{H} = -\frac{5}{2} \frac{\kappa}{T} \nabla T \delta T - \kappa \nabla \delta T. \quad (4.21)$$

A simplification arises here too, as ∇T is 0 because we are perturbing a background flow with

a uniform temperature. This will be true even if the background flow is dynamic so long as the temperature scale height $T/|\nabla T|$ is much larger than the wavelength of the perturbation. This reasoning also lets us discard a term from $\nabla \cdot \delta \mathcal{H}$, leaving just

$$\nabla \cdot \delta \mathcal{H} = -\kappa \nabla^2 \delta T. \quad (4.22)$$

To close this set of equations, we need to write $\delta \mathcal{L}$, as well as the δT appearing in (4.22), in terms of δp and $\delta \rho$. The functional form of \mathcal{L} is $\mathcal{L} = \mathcal{L}(\rho, T)$, so we formally have

$$\delta \mathcal{L} = \frac{\partial \mathcal{L}}{\partial \rho} \delta \rho + \frac{\partial \mathcal{L}}{\partial T} \delta T. \quad (4.23)$$

We can eliminate δT in favor of δp and $\delta \rho$ by perturbing our equation of state to find,

$$\frac{\delta T}{T} = \frac{\delta p}{p} - \frac{\delta \rho}{\rho}. \quad (4.24)$$

Combining the previous two equations gives

$$\begin{aligned} \frac{\delta \mathcal{L}}{\Lambda} &= \frac{T}{\Lambda} \frac{\partial \mathcal{L}}{\partial T} \left[\frac{\delta p}{p} - \frac{\delta \rho}{\rho} \right] + \frac{\rho}{\Lambda} \frac{\partial \mathcal{L}}{\partial \rho} \frac{\delta \rho}{\rho} \\ &= L_T \left[\frac{\delta p}{p} - \frac{\delta \rho}{\rho} \right] + L_\rho \frac{\delta \rho}{\rho}, \end{aligned} \quad (4.25)$$

where we have introduced the total cooling rate Λ to normalize \mathcal{L} since we know from Chapter 3 that $\mathcal{L} = \Lambda - \Gamma$. In the second line we have defined the all important dimensionless quantities L_T and L_ρ that bear obvious resemblance to instability criteria, as indeed they will be seen to be. For use later on, we rewrite these definitions, explicitly highlighting the variables being held constant on the partial derivatives:

$$L_T \equiv \frac{T}{\Lambda} \left(\frac{\partial \mathcal{L}}{\partial T} \right)_\rho \quad \text{and} \quad L_\rho \equiv \frac{\rho}{\Lambda} \left(\frac{\partial \mathcal{L}}{\partial \rho} \right)_T. \quad (4.26)$$

Substituting in the plane wave perturbations in (4.3) and (4.4) exchanges the derivatives for σ and $i\mathbf{k}$:

$$\sigma A_\rho + i\mathbf{k} \cdot (A_\rho \mathbf{v} + \rho \mathbf{A}_v) = 0, \quad (4.27)$$

$$\sigma(A_\rho \mathbf{v} + \rho \mathbf{A}_v) + i\mathbf{k} \cdot (A_\rho \mathbf{v} \mathbf{v} + 2\mathbf{A}_v \rho \mathbf{v}) + i\mathbf{k} A_p = 0, \quad (4.28)$$

$$\begin{aligned}
& \frac{1}{\gamma-1}\sigma A_p + \frac{1}{\gamma-1}i\mathbf{k} \cdot (p\mathbf{A}_v + \mathbf{v}A_p) + ip\mathbf{k} \cdot \mathbf{A}_v \\
& = -A_\rho \mathcal{L} - \rho\Lambda L_T \left[\frac{A_p}{p} - \frac{A_\rho}{\rho} \right] - \rho\Lambda L_\rho \frac{A_\rho}{\rho} - k^2 \kappa T \left[\frac{A_p}{p} - \frac{A_\rho}{\rho} \right],
\end{aligned} \tag{4.29}$$

where $k^2 = \mathbf{k} \cdot \mathbf{k}$ in the last term of the last equation is a result of the ∇^2 operator. We now recast these equations by introducing a dimensionless growth rate and wave number,

$$n = \sigma t_s, \tag{4.30}$$

$$\mathbf{k}' = \mathbf{k} c_s t_s, \tag{4.31}$$

where t_s is a fiducial sound crossing timescale and $c_s t_s$ a corresponding length scale, $c_s = \sqrt{\gamma p/\rho}$ being the adiabatic sound speed in the background medium. The sound crossing timescale is actually a free parameter that is controlled by specifying t_s as some ratio of the characteristic cooling timescale t_{th} (defined below) associated with \mathcal{L} . We also define dimensionless amplitudes as

$$A'_q = \frac{A_q}{q_c}, \tag{4.32}$$

where q_c denotes the characteristic quantity used to normalize A_q ; we choose $q_c = (\rho, c_s, \rho c_s^2)$ for the amplitudes $A_q = (A_\rho, A_v, A_p)$ of the primitive variables. Then (4.27), (4.28), and (4.29) are made dimensionless by multiplying by t_s/ρ , $t_s/(\rho c_s)$, and $t_s/(\rho c_s^2)$, respectively, to give

$$nA'_\rho + i\mathbf{k}' \cdot (A'_\rho \mathbf{M} + \mathbf{A}'_v) = 0, \tag{4.33}$$

$$n(A'_\rho \mathbf{M} + \mathbf{A}'_v) + i\mathbf{k}' \cdot (A'_\rho \mathbf{M} \mathbf{M} + 2\mathbf{A}'_v \mathbf{M}) + i\mathbf{k}' A'_p = 0, \tag{4.34}$$

$$\begin{aligned}
& \frac{1}{\gamma-1}nA'_p + \frac{1}{\gamma-1}i\mathbf{k}' \cdot \left(\frac{1}{\gamma} \mathbf{A}'_v + \mathbf{M} A'_p \right) + \frac{i}{\gamma} \mathbf{k}' \cdot \mathbf{A}'_v \\
& = -t_s \frac{\Lambda}{c_s^2} \left(L_\rho + \frac{\mathcal{L}}{\Lambda} \right) A'_\rho - t_s \frac{\Lambda}{c_s^2} \left(L_T + k^2 \frac{\kappa T}{\rho \Lambda} \right) [A'_p - A'_\rho].
\end{aligned} \tag{4.35}$$

Here, $\mathbf{M} = \mathbf{v}/c_s$ is the vector Mach number and \mathcal{M} its magnitude. Notice that this normalization procedure has removed all background flow quantities from the l.h.s of the equations, save for \mathbf{M} . Where these background flow quantities appear on r.h.s of the energy equation reveals the characteristic length of time scales governing the problem. In particular, notice how the Field length introduced in Chapter 1 enters. Begelman and McKee (1990) defined this quantity as simply

$\sqrt{\kappa T/\rho\Lambda}$, whereas we defined $\lambda_F = 2\pi\sqrt{\kappa T/\rho\Lambda}$ in order to write

$$k^2 \frac{\kappa T}{\rho\Lambda} = \left(\frac{\lambda_f}{\lambda}\right)^2, \quad (4.36)$$

where $\lambda = 2\pi/k$ is the wavelength of the perturbation. In other words, our definition of λ_F is a direct comparison of the conduction length scale and the perturbation length — and thus eventual cloud size — which is why this definition of λ_F is comparable to the width of the cloud interfaces (while $\sqrt{\kappa T/\rho\Lambda}$ is an order of magnitude smaller).

We recognize Λ/c_s^2 as the inverse of a characteristic cooling timescale and define the thermal time introduced above as

$$t_{\text{th}} \equiv \frac{\mathcal{E}}{\Lambda}, \quad (4.37)$$

noting that $c_s^2 = \gamma(\gamma - 1)\mathcal{E}$. The r.h.s of (4.35) further suggests that we define the new quantities

$$L'_\rho \equiv L_\rho + \frac{\mathcal{L}}{\Lambda}, \quad (4.38)$$

and

$$L'_T \equiv L_T + \left(\frac{\lambda_f}{\lambda}\right)^2, \quad (4.39)$$

which are both physically significant: (4.38) will be seen to generalize the stability criterion to account for perturbations off the radiative equilibrium curve ($|\mathcal{L}| > 0$), while (4.39) contains the modifications due to conduction. Multiplying (4.35) by $\gamma(\gamma - 1)$ brings us to our final form for the perturbed energy equation,

$$\gamma n A'_p + i\gamma \mathbf{k}' \cdot \mathcal{M} A'_p + i\gamma \mathbf{k}' \cdot \mathbf{A}'_v = -\frac{L'_\rho A'_\rho + L'_T(A'_p - A'_\rho)}{t_{\text{th}}/t_s}. \quad (4.40)$$

4.4.1 Dispersion relation in a stationary medium

As will be shown later, a moving background medium has no effect on the growth rate of TI. Since the growth rate alone determines the instability criterion, we first present a detailed analysis of the results of linear theory for $\mathcal{M} = 0$. To derive a dispersion relation, we solve (4.33) for $i\mathbf{k}' \cdot \mathbf{A}'_v$,

$$i\mathbf{k}' \cdot \mathbf{A}'_v = -n A'_\rho, \quad (4.41)$$

and then use this relationship to solve both (4.34) and (4.40) for A'_p/A'_ρ . Dotted \mathbf{k}' into (4.34) gives

$$\frac{A'_p}{A'_\rho} = -\frac{n^2}{\mathbf{k}'^2}, \quad (4.42)$$

while (4.40) reveals

$$\frac{A'_p}{A'_\rho} = 1 - \frac{L'_\rho}{(t_{\text{th}}/t_s)\gamma n + L'_T}. \quad (4.43)$$

Equating these expressions yields the cubic dispersion relation

$$\frac{t_{\text{th}}/t_s}{\mathbf{k}'^2} n^3 + \frac{L'_T}{\mathbf{k}'^2} n^2 + (t_{\text{th}}/t_s)n = \frac{L'_\rho - L'_T}{\gamma}. \quad (4.44)$$

Only one of the roots is real valued and it corresponds to the TI mode. The other two are complex valued and correspond to forward and backward propagating sound waves (relative to \mathbf{k}'). We can therefore write $n = \pm i\omega'$ to determine their real-valued (dimensionless) frequencies ω' . Note that (4.44) has the same form as the cubic given by Field (1965) but now allows computing the growth rates for the TI mode when $|\mathcal{L}| > 0$.

4.4.2 Instability criteria

While the instability criteria for TI can be inferred from a deeper analysis of (4.44), it is more informative to step back and see where the isobaric TI mode originates. An analysis of the eigenstructure of the equations of hydrodynamics (e.g., Toro 2009) reveals that the non-propagating TI mode is associated with the ‘entropy mode’, suggesting its origin is in fact the energy equation. Indeed we can already see this by noting that the sound waves just uncovered came entirely from the momentum equation, as letting $n = \pm i\omega' = \pm i\omega t_s$ lets us rewrite (4.42) as

$$\frac{w^2}{\mathbf{k}^2} = c_s^2 \frac{A'_p}{A'_\rho}, \quad (4.45)$$

where we returned to dimensional units in which $\mathbf{k}' = (t_s c_s)\mathbf{k}$. This equation reveals the wave velocity $\omega/\mathbf{k} = c_s \sqrt{(A'_p/A'_\rho)}$. Notice from (4.43) that $A'_p/A'_\rho = 1$ when $t_{\text{th}} \gg t_s$, in which case the waves suffer no damping and propagate at the adiabatic speed of sound.

A different way to view this is found by examining the physical meaning of the ratio A'_p/A'_ρ , which in dimensional units is $(A_p/\rho c_s^2)/(A_\rho/\rho) = (c_s^2/\gamma)A_p/A_\rho$. Recall that the amplitude A_p is just the magnitude of the pressure perturbation δp , and likewise $A_\rho = |\delta\rho|$, so the statement $A'_p/A'_\rho = 1$

is equivalent to $\gamma\delta p/\delta\rho = c_s^2$. The isobaric TI mode, on the other hand, should have $\delta p \approx 0$ and therefore $A'_p/A'_\rho \approx 0$. By this logic, we see that the ratio A'_p/A'_ρ coming from the energy equation, (4.43), contains our instability criteria for TI in the regime where $t_{\text{th}} \sim t_s$. Solving this equation for n , we find

$$n \frac{t_{\text{th}}}{t_s} = \frac{L'_\rho(1 - A'_p/A'_\rho)^{-1} - L'_T}{\gamma}. \quad (4.46)$$

With $A'_p/A'_\rho \approx 0$, we express (4.46) as

$$\sigma t_{\text{th}} \approx \frac{L'_\rho - L'_T}{\gamma}, \quad (4.47)$$

where we have returned to our dimensional growth rate σ . Exponential growth requires $\sigma > 0$ from (4.3), so our instability criterion is

$$L'_\rho > L'_T. \quad (4.48)$$

Recalling the definitions of L'_T , we see that conduction has a stabilizing influence by increasing L'_T , thereby making it harder for this inequality to be satisfied. From (4.39), this can only happen for sufficiently small wavelengths. Very short wavelengths, $\lambda \ll \lambda_F$, will correspond to large damping rates (i.e. $\sigma < 0$) and this can be viewed as the evaporation of tiny perturbations.

Explicit in the definition of L_ρ from (4.26) is vertical movement on a phase diagram in (ρ, T) -space. From the definition of L'_ρ , we see that upon occupying an unstable location on the equilibrium curve, deviations above it into regions of net cooling has a destabilizing influence, while veering beneath it is stabilizing.

4.4.3 Recovering Balbus' and Field's criterion

Expanding the derivative in Balbus' criterion, (4.17), leads to

$$\left(\frac{\partial \mathcal{L}}{\partial T}\right)_p < \frac{\mathcal{L}}{T}, \quad (4.49)$$

and this reduces to Field's isobaric criterion for gas in radiative equilibrium with $\mathcal{L} = 0$. The equivalence of this expression with (4.48) is readily seen by using the definitions of L'_T and L'_ρ and the original definitions of L_T and L_ρ from (4.26) to arrive at

$$\left(\frac{\partial \mathcal{L}}{\partial T}\right)_\rho - \frac{\rho}{T} \left(\frac{\partial \mathcal{L}}{\partial \rho}\right)_T < \frac{\mathcal{L}}{T} - \frac{\Lambda}{T} \left(\frac{\lambda_F}{\lambda}\right)^2. \quad (4.50)$$

By the following thermodynamic identity,

$$\left(\frac{\partial \mathcal{L}}{\partial T}\right)_p = \left(\frac{\partial \mathcal{L}}{\partial T}\right)_\rho - \frac{\rho}{T} \left(\frac{\partial \mathcal{L}}{\partial \rho}\right)_T, \quad (4.51)$$

we recover, after neglecting conduction ($\lambda_F = 0$), Balbus' criterion for TI.

4.4.4 Generalized stability criterion

By expressing the growth rate in terms of Balbus' criterion using (4.47), a useful comparison can be made with the work of Kim & Narayan (2003), who carried out a full Lagrangian analysis including conduction. Utilizing the results of §4.4.3 and recalling our definition of the thermal time,

$$t_{\text{th}} = \frac{\mathcal{E}}{\Lambda} = \frac{P}{\rho(\gamma - 1)\Lambda}, \quad (4.52)$$

(4.47) becomes

$$\sigma = -\frac{\gamma - 1}{\gamma} \frac{\bar{m}}{k} T \left(\frac{\partial \mathcal{L}/T}{\partial T}\right)_p - \frac{\gamma - 1}{\gamma} \frac{\bar{m}\Lambda}{kT} \left(\frac{\lambda_F}{\lambda}\right)^2. \quad (4.53)$$

Accounting for a typo,¹ this expression is equivalent to that found in Kim & Narayan (2003), demonstrating that Lagrangian and Eulerian analyses do in fact agree.

By requiring $\sigma > 0$, we arrive at the following generalized stability criterion for TI that accounts for thermal conduction:

$$\left(\frac{\partial \mathcal{L}/T}{\partial T}\right)_p < -\frac{\Lambda}{T^2} \left(\frac{\lambda_F}{\lambda}\right)^2. \quad (4.54)$$

Note that this criterion is still based on the approximation (4.47), which neglects any pressure effects. The actual stability criterion from (4.46) is

$$L'_\rho > L'_T(1 - A'_p/A'_\rho), \quad (4.55)$$

but this is a priori unknown since A'_p/A'_ρ is found by evaluating (4.43) after solving for n . Since $A'_p/A'_\rho < 0$ by (4.42), pressure effects are seen to be stabilizing. To assess the presence of TI definitively, therefore, the dispersion relation must be solved to see if the growth rate is actually negative for the specific radiative cooling model underlying \mathcal{L} , which yields the parameters L'_T , L'_ρ , and t_{th} , and the actual perturbation, which is determined by \mathbf{k}' and A'_ρ . In practice, the approximation (4.47) only breaks down for parameters leading to very small growth rates (for only

¹There should be an additional factor of T in their equation 25.

then can the stabilizing influence of pressure have any effect), and therefore the interesting regime is always given by the analytic instability criterion, (4.54).

4.4.5 Dispersion relation in a uniformly moving medium

We stated earlier that a nonzero velocity of the background medium does not alter the growth rate of TI. This is because the dispersion relation with $\mathcal{M} = \text{constant}$ works out to be identical to (4.44) but with n changed to

$$n' \equiv n + i\mathbf{k}' \cdot \mathcal{M}. \quad (4.56)$$

Thus, there is only a phase modulation of the exponential. To arrive at this result, simply carry out the same procedure as before: first obtain an expression for $i\mathbf{k}' \cdot \mathbf{A}'_v$ from (4.33), and then use this to solve both (4.34) and (4.40) for A'_p/A'_ρ — equations identical to (4.42) and (4.43) are obtained, but with n' in place of n . This means that A'_p becomes a complex number, and the resulting waveforms are just shifted versions of Figure 4.1.

4.5 Numerical simulations of TI

Numerical simulations of cloud formation commonly seed the TI using a superposition of individual plane wave solutions to the $\mathcal{M} = 0$ dispersion relation (e.g., Koyama & Inutsuka 2004) or random perturbations (e.g., Choi & Stone 2012). Our goal is to study the nonlinear regime of TI in a very controlled means in order to investigate the effect of self-consistently including a radiation force. We therefore seed the TI using a single isobaric perturbation and then let it evolve.

4.5.1 Initial conditions for cloud simulations

The analytic waveforms in Figure 4.1 are the initial conditions for our numerical simulations. The definitions of our Eulerian perturbations from the beginning of the chapter become in dimensionless units

$$q(\mathbf{x}, t) = q_0(\mathbf{x}, t) + q_c A'_q \exp(n't' + i\mathbf{k}' \cdot \mathbf{x}). \quad (4.57)$$

Recall that $q_c = (\rho, c_s, \rho c_s^2)$ is the normalization corresponding the the respective variable $q = (\rho, v, p)$ and are taken in terms of initial values $q_0(\mathbf{x}, 0)$. The exponential is of course just a calculational device, as what we need are waveforms in terms of sine and cosine functions. These functions

are obtained by taking the real part of (4.57), but this requires a bit of effort since for $\mathcal{M} \neq 0$, both A_q and n' are complex valued. Let us therefore denote $A_q = a_R + ia_I$ and $n' = n_R + in_I = n + i\mathbf{k}' \cdot \mathcal{M}_0$ and consider the flow to be moving in the x -direction with Mach number \mathcal{M}_0 in the presence of a perturbation along x , i.e. $\mathbf{k}' = (k'_x, 0, 0)$. We have,

$$\begin{aligned} A'_q \exp(n't' + i\mathbf{k}' \cdot \mathbf{x}) &= (a_R + ia_I) e^{n_R t'} \exp[i(n_I + k'_x x)] \\ &= [a_R \cos(k'_x x + k'_x \mathcal{M}_0) - a_I \sin(k'_x x + k'_x \mathcal{M}_0)] e^{n't'} + \\ &\quad i[a_I \cos(k'_x x + k'_x \mathcal{M}_0) + a_R \sin(k'_x x + k'_x \mathcal{M}_0)] e^{n't'}, \end{aligned} \quad (4.58)$$

and taking only the real part gives the following analytic solution for the density along x , which has $a_R = A'_\rho$ and $a_I = 0$:

$$\rho(x, t) = \rho_0 + \rho_0 A'_\rho \cos[k'_x(x + \mathcal{M}_0)] e^{n't'}. \quad (4.59)$$

Since the superposition principle holds for the linearized equations, any perturbations along y or z will simply add on cosine factors, thereby fully determining $\rho(\mathbf{x}, t)$ in the linear regime. We limit ourselves to 2D simulations in this thesis, giving

$$\rho(\mathbf{x}, t) = \rho_0 + \rho_0 (A'_\rho)_x \cos[k'_x(x + \mathcal{M}_0)] e^{n_x t'} + \rho_0 (A'_\rho)_y \cos[k'_y y] e^{n_y t'}, \quad (4.60)$$

where we have allowed for different amplitudes, wavenumbers, and growth rates in each direction.

The perturbation amplitudes for density above are free parameters. The velocity and pressure amplitudes are given in terms of A'_ρ by (4.41) and (4.42). The solution for the velocity along x , which has $a_R = -\mathcal{M}_0 A'_\rho$ and $a_I = (n/k') A'_\rho$, reads

$$v(x, t) = v_0 - c_{s,0} A'_\rho \left[\frac{n}{k'} \sin[k'(x + \mathcal{M}_0)] + \mathcal{M}_0 \cos[k'(x + \mathcal{M}_0)] \right] e^{n't'}. \quad (4.61)$$

Pressure has $a_R = -n^2/k'^2 + \mathcal{M}_0^2$ and $a_I = -2\mathcal{M}_0 n/k'$ giving

$$p(x, t) = p_0 + \rho_0 c_{s,0}^2 A'_\rho \left[\left(-\frac{n^2}{k'^2} + \mathcal{M}_0^2 \right) \cos[k'(x + \mathcal{M}_0)] + 2\frac{n}{k'} \mathcal{M}_0 \sin[k'(x + \mathcal{M}_0)] \right] e^{n't'}. \quad (4.62)$$

For the y -direction, an analogous factor in brackets is added. Figure 4.1 is a plot of these 1D solutions for $\mathcal{M}_0 = 0$.

We note that in addition to serving as initial conditions (by neglecting the factors of $e^{n't'}$ above), these analytic solutions can be used for several different code tests. Since TI requires source terms for

both heating and cooling and conduction, these solutions can serve as benchmarks for those modules. They can additionally be used to assess advection errors, which increase with \mathcal{M}_0 ; Eulerian codes are highly susceptible to these errors.

4.5.2 Cloud tracking and a bound for the density perturbation

Here we mention two numerical considerations that are important for simulating TI. First, a technique to minimize advection errors, by keeping the velocity field small, was developed by Shin et al. (2008) and is commonly referred to as ‘cloud tracking’. It involves calculating the average cloud velocity at every timestep and subtracting this from the velocity field at every location. Without the use of cloud tracking in our simulations, the advection errors were found to be severe enough to affect the energy balance in the core of the cloud, likely attributable to numerical errors associated with the $\nabla \cdot \mathbf{v}$ (pressure work) term in (2.18).

Second, if the amplitude A'_ρ is not chosen small enough, nonlinear terms will prevent an exact match with the above analytic solutions. A bound on A'_ρ placing the initial conditions fully in the linear regime can be found by examining the perturbed ideal gas law to second order. A departure from an equilibrium state will always satisfy

$$\frac{p_0 + \delta p}{(\rho_0 + \delta\rho)(T_0 + \delta T)} = \frac{p_0}{\rho_0 T_0}, \quad (4.63)$$

which is the same as

$$\frac{\delta p}{p_0} = \frac{\delta\rho}{\rho_0} + \frac{\delta T}{T_0} + \frac{\delta\rho\delta T}{\rho_0 T_0}. \quad (4.64)$$

We require the nonlinear term to be very small, i.e.

$$\frac{\delta\rho}{\rho_0} \frac{\delta T}{T_0} \ll \frac{\delta p}{p_0}. \quad (4.65)$$

Now $\delta\rho/\rho_0$ is A'_ρ and $\delta p/p_0$ is $\gamma A'_p$, so we find the bound $A'_\rho \ll |\gamma A'_p/(\delta T/T_0)|$, which upon substituting in (4.24) and noting that $A'_p \ll 1$ gives, according to (4.42),

$$A'_\rho \ll \sqrt{\gamma} \left| \frac{n}{\mathbf{k}} \right|. \quad (4.66)$$

Moreover, it is seen that δT and A'_p/A'_ρ have the same sign, meaning $\delta T < 0$ for $\delta\rho > 0$, providing us with an expectation for when nonlinear terms begin to affect the solution: the pressure should

drop below the analytic solution according to (4.64). This effect is indeed seen while still in the linear (i.e. exponential) growth regime.

Chapter 5

CLOUD FORMATION AND ACCELERATION

Chapters 5-8 contain slightly modified versions of the published papers on which this thesis is based. The previous chapter presented the initial conditions used to evolve an isobaric TI mode into the nonlinear regime, while in Chapter 3 we derived a generic form for the radiation force, \mathbf{f}_{rad} , that we use to obtain the results presented in §5.3. Specifically, in Chapter 3 we divided the radiation field into N frequency groups, which allowed us to write \mathbf{f}_{rad} in the familiar form of (3.9). Here we arrive at an explicit expression for \mathbf{f}_{rad} by approximating the radiation field as consisting of only an ionizing X-ray flux F_X and a non-ionizing UV flux, F_{UV} . That is, we take $N = 2$, giving

$$\mathbf{f}_{rad} = \frac{\kappa_X \rho F_X}{c} \hat{x} + \frac{\kappa_{UV} \rho F_{UV}}{c} \hat{x}. \quad (5.1)$$

Here we have also made a ‘local simulation’ approximation, as we assume radiation free streaming through a local region of space that originated from a distant source, in which case we can align our simulation domain in the direction of the flux, taken to be \hat{x} .

We must now associate κ_X and κ_{UV} with the relevant sources of opacity identified in §3.2. Our designating F_{UV} as a non-ionizing flux implies that the UV photons will not heat the gas, and a bound-free opacity is therefore only associated with κ_X . The ions that are predominantly responsible for line-driving have resonance line transitions in the UV range, meaning that only κ_{UV} has a bound-bound opacity contribution. We thus rewrite (5.1) as

$$\mathbf{f}_{rad} = \left[\kappa_{X,ff} + \kappa_{X,bf} + (\kappa_{UV,ff} + \kappa_{UV,bb}) \frac{F_{UV}}{F_X} \right] \frac{\rho F_X}{c} \hat{x}. \quad (5.2)$$

Here we have included a free-free opacity for both F_X and F_{UV} , and since electron scattering is frequency independent, $\kappa_{X,ff} = \kappa_{UV,ff} = \kappa_e$. As described in §5.2, an effective bound-bound opacity is embodied by the force multiplier, which is denoted $M(t)$ (t is a dimensionless optical depth parameter) and quantifies the enhancement in scattering opacity due to lines compared with electron scattering, i.e. $\kappa_{UV,bb} = M(t)\kappa_e$. Defining the flux ratio $f_{UV} \equiv F_{UV}/F_X$ as well as

$\sigma_X \equiv \kappa_{X,bf}/\kappa_e$, we now have

$$\mathbf{f}_{rad} = (1 + \sigma_X + [1 + M(t)]f_{UV}) \frac{\kappa_e \rho F_X}{c} \hat{x}. \quad (5.3)$$

This is the final form of the radiation force we use. Note that in AGN, $f_{UV} > 1$.

5.1 Theory and expectations

To facilitate a simple comparison between our simulations and Field’s theory (i.e. the linear growth rates), we include thermal conduction, assume the gas to be initially stationary, homogenous, and non-magnetized, and we do not include gravity. We model the formation and evolution of optically thin clouds whose thermal equilibrium state is controlled by impinging radiation by adopting a realistic prescription for heating and cooling appropriate for gas in an AGN environment. Specifically, we use a net cooling function, \mathcal{L} , that includes the following radiative processes: (1) Compton and inverse-Compton scattering, (2) photoionization and recombination, (3) Bremsstrahlung, and (4) line-emission. In an optically thin case, \mathcal{L} depends on the gas temperature, T , and photoionization parameter, $\xi = 4\pi F_X/n$, where F_X is the X-ray flux and n is the gas number density.¹

The following theoretical picture forms the basis of our expectations and motivates our simulation setup. For a given ξ , gas in equilibrium at temperature T_{eq} will have heating balancing cooling [i.e., $\mathcal{L}(T_{eq}, \xi) = 0$]. Therefore, it will occupy one point on the radiative equilibrium curve (the solid line which is hereafter denoted the S-curve) shown in the top panel of Figure 5.1. Suppose that initially this point is at a stable location on the S-curve such as at position 1 in Figure 5.1, but some physical event transpires that results in a reduction of F_X so that the gas finds itself out of equilibrium at location 2 with, for example, $\xi_2 = 190$. It will quickly cool to reside on the S-curve at location 3 (with $\xi_3 = \xi_2$). However, at this position, gas is thermally unstable to perturbations with constant pressure p , as it violates Field’s criterion for stability, $[\partial\mathcal{L}/\partial T]_p > 0$. More generally, only the region below the dashed line is thermally stable according to Balbus’ criterion $[\partial(\mathcal{L}/T)/\partial T]_p > 0$, with the consequence that gas occupying the shaded grey region in Figure 5.1 will evolve to points on the S-curve outside of the grey region. Continuing with our example, the slightest density perturbation present in the gas at location 3 will grow exponentially at the linear theory rate and at nearly constant pressure until the perturbation becomes nonlinear. Rapid non-

¹The units for ξ are erg cm s^{-1} and we do not cite them hereafter.

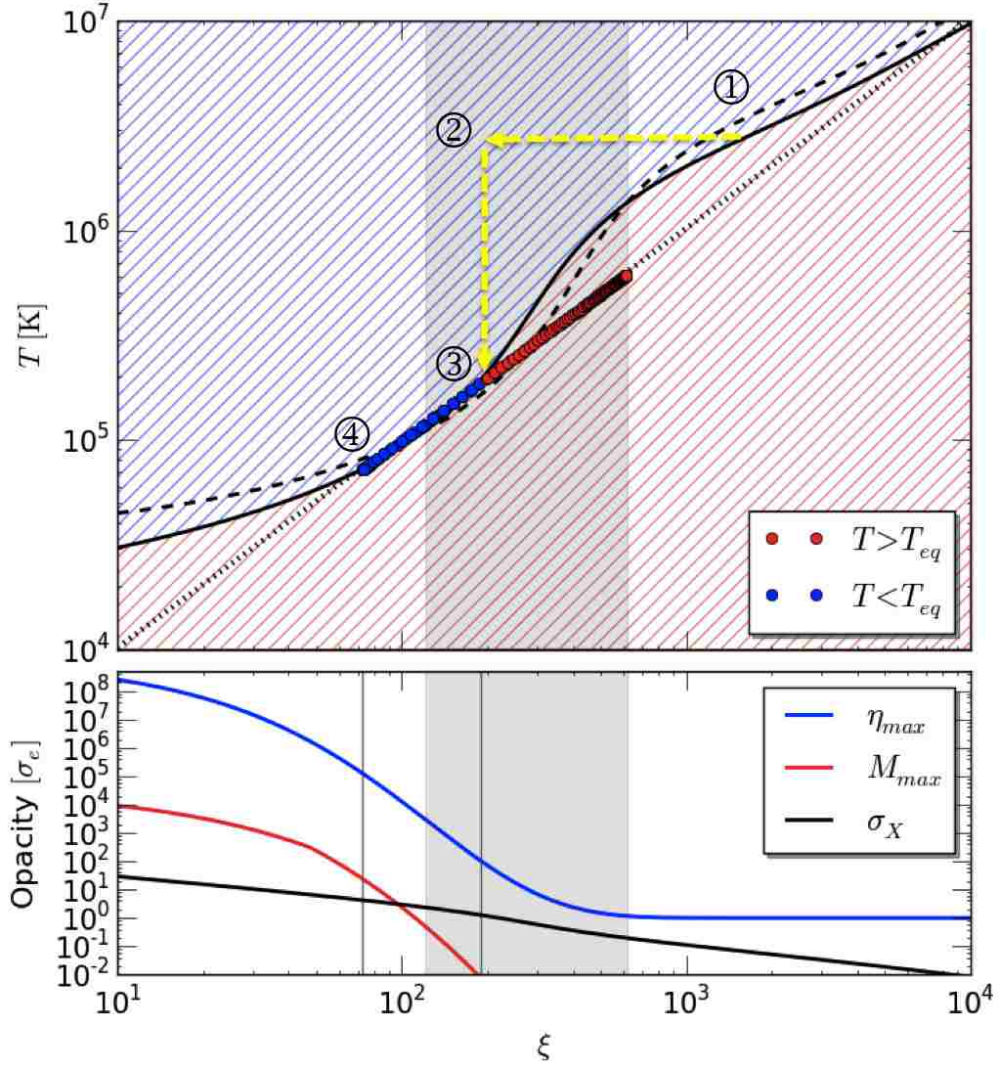


Figure 5.1: Temperature and opacity dependence on the photoionization parameter expected in an AGN environment. **Top panel:** The solid line is the S-curve found by solving $\mathcal{L}(T, \xi) = 0$. The region above (below) this line is patterned light blue (red) to denote cooling (heating), as gas in this region is above (below) the equilibrium temperature. The dashed curve (defined by $[\partial\mathcal{L}/T]/\partial T|_p = 0$) marks the isobaric instability criterion. Thermally stable gas must lie below this curve; gas anywhere in the grey region cannot settle on the S-curve in this region without being unstable. The dotted line shows a constant pressure slope. Stable gas at location (1) is envisioned to be suddenly subjected to a reduced flux, placing it at location (2), where it is unstable. This gas will rapidly cool (nearly isochorically) until it reaches a new thermal equilibrium which is now unstable [marked as location (3) on the equilibrium curve]. We begin our simulations at this new equilibrium to follow the growth of an isobaric perturbation. As one can anticipate, the perturbation grows maintaining pressure equilibrium even during the non-linear phase and the points representing gas move along the dotted line; in particular those representing the cold gas move toward yet another thermal equilibrium location (4) which is now stable. All points in the computational domain of 1-D run RFLDX (radiation force due to X-rays and lines) are over-plotted as blue ($T < T_{eq}$) and red ($T > T_{eq}$) dots to indicate the final state of the gas. **Bottom panel:** Gas opacity in the units of the Thomson opacity as a function of ξ . The solid red line represents bound-bound opacity, M_{max} . This opacity can become orders of magnitude larger than bound-free opacity σ_X (shown as the solid black line). The solid blue line represents the opacity of the most opaque line. To gauge the increase in opacity for the cloud formed in the top panel [location (4)], the two vertical lines mark the initial conditions ($\xi_3 = 190$) of the gas and the eventual location of the cloud core ($\xi_4 \approx 73$).

linear growth (still at nearly constant pressure) will then commence (e.g., Burkert & Lin 2000) and result in the formation of a cloud with a core density approximately determined by the intersection of the dotted line and the S-curve (position 4), which is where the gas in the core is stable.

The bottom panel of Figure 5.1 illustrates how various gas opacities depend on ξ . Solid black and red lines show the bound-free opacity, σ_X , and the total line opacity, M_{\max} , respectively. The solid blue line represents the opacity of the most opaque line. One can see that for ξ_3 , the bound-free and bound-bound opacity is negligible. (The vertical line in the grey region marks the location $\xi_3 = 190$.) However, once the thermally unstable gas forms a dense cloud, σ_X and M_{\max} are significantly increased, as indicated by the left vertical line at $\xi_4 \approx 73$. Therefore the cloud can be accelerated by the same source that heats it.

5.2 Governing equations

To confirm and quantify our expectations, we numerically solve the equations of hydrodynamics, (2.38) - (2.40). We denote the functional dependence of the net cooling function as $\mathcal{L} = \Lambda - \Gamma$, with

$$\Lambda = \frac{n}{\mu m_p} (L_{\text{ff}} + L_{\text{bb}}) [\text{erg g}^{-1} \text{s}^{-1}], \text{ and} \quad (5.4)$$

$$\Gamma = \frac{n}{\mu m_p} (G_C + G_X) [\text{erg g}^{-1} \text{s}^{-1}], \quad (5.5)$$

where μ is the mean molecular weight (set to 1.0 in this work) such that $n = \mu m_p \rho$ (with m_p the proton mass), L_{ff} and L_{bb} are the cooling rates due to free-free and bound-bound transitions, and G_C and G_X are the heating rates due to Compton and X-ray heating, respectively (all four rates are in units of $\text{erg cm}^3 \text{s}^{-1}$). For L_{ff} and G_C , we use the well-known analytic formulas based on atomic physics; see Appendix A. For L_{bb} and G_X , meanwhile, we use the analytical fits given by Blondin (1994), who found good agreement (to within 25%) between his approximate rates and those resulting from detailed photoionization calculations. Blondin's formulae, also provided in Appendix A, assume an optically thin gas of cosmic abundances illuminated by a $T_X = 10 \text{ keV}/k_B$ bremsstrahlung spectrum (with k_B Boltzmann's constant).

To evaluate \mathbf{f}_{rad} , we must specify F_X , σ_X , f_{UV} , and $M(t)$ in (5.3). The X-ray flux is set by the photoionization parameter ξ , so $F_X = n\xi/4\pi$. The quantity σ_X is an effective X-ray opacity in units of κ_e that we compute using (3.16) as $(4\pi G_{X,h}/\xi)/\kappa_e$, where $G_{X,h}$ is the heating part of G_X (see Appendix A). In the optically thin limit, $M(t)$ takes on its maximum value, M_{\max} , and is just

a sum of opacity contributions from all the lines. It depends on the gas composition, ionization, excitation and oscillator strengths [e.g., see eqs. 10 and 11 in Castor, Abbott, & Klein, (1975); CAK hereafter]. We evaluate M_{\max} following Stevens & Kallman (1990, SK90 hereafter) with a modification due to Owocki, Castor, & Rybicki (1988), who used

$$M_{\max} = k_{\text{CAK}}(1 - \alpha)\eta_{\max}^{\alpha}. \quad (5.6)$$

Here, k_{CAK} is proportional to the total number of lines, α is the ratio of strong to weak lines, and finally $\eta_{\max} = \kappa_{L,\max}/\kappa_e$ is a dimensionless measure of opacity of the most opaque line (with $\kappa_{L,\max}$ being the line opacity coefficient of the thickest line).

SK90 carried out detailed photoionization calculations for a radiative environment appropriate for X-ray sources and parametrized their results in terms of the above expression for M_{\max} by allowing k_{CAK} to be T -dependent and η_{\max} to be ξ -dependent. Instead of the fit for $k_{\text{CAK}}(T)$ from SK90, we use equation (17) of Proga (2007) due to Kallman (2006, private communication), as this may better represent the increase in the number of lines with decreasing temperature in AGN. This expression and that for $\eta_{\max}(\xi)$, which is equation (19) of SK90, are provided in Appendix B. Both of these fits were generated assuming $\alpha = 0.6$. In the bottom panel of Figure 5.1, we plot σ_X along with M_{\max} . Notice that M_{\max} can be roughly a few thousand for gas ionized by a weak radiation field, whereas it decreases asymptotically to zero for highly ionized gas as the radiation field becomes stronger.

5.3 Methods and results

We solve equations (2.3)-(2.40) in 1-D and 2-D using the CTU integrator, Roe flux, and explicit conduction module of the MHD code ATHENA (Stone et al. 2008). We modify the original version of the code by adding the momentum and heating and cooling source terms in the same way that ATHENA's built-in static gravitational potential source term is implemented to achieve 2nd order accuracy in both space and time. We use a less accurate method for integrating the conduction term in time in our 2-D simulations than in our 1-D simulations. Specifically, we use ATHENA's super time-stepping scheme (STS; see O'Sullivan & Downes 2006), although we note that a 2nd order accurate in time STS algorithm does exist (Meyer et al. 2012) and we are testing it for future use.

5.3.1 Initial and boundary conditions

Given the atomic physics behind our S-curve and the opacities in Figure 5.1, the following free parameters govern our problem: the wavenumber and density amplitude of the TI perturbation, k and $\delta\rho$, as well as the ratio of the initial sound crossing and thermal times t_{th}/t_{sc} , which together determine the number of clouds and their formation time; the initial photoionization parameter ξ_3 , which controls the intensity of the radiation field and the equilibrium temperature T_{eq} ; the equilibrium pressure, namely the product $n_{eq}T_{eq}$, which sets the physical units of the cloud and its environment; and finally f_{UV} , which parametrizes the shape of the spectral energy distribution in a simple way.

Our initial conditions are full wavelength profiles of the TI condensation mode, found from equations (11)-(14) in Field (1965), applied to density, velocity, and pressure. We adopt $n_{eq}T_{eq} = 10^{13} \text{ K cm}^{-3}$ in accordance with AGN observations and their modeling (e.g., Davidson & Netzer 1979; Krolik et al. 1981). The length scale of the perturbation is fixed by the adiabatic sound speed at position 3 in Figure 5.1, c_{eq} , and a choice for the initial sound crossing time, t_{sc} . We chose t_{sc} equal to the initial thermal time, $t_{th} = \mathcal{E}_{eq}/\Lambda_{eq}$, which results in near maximum linear growth rates for the condensation mode. These rates are obtained by solving the dispersion relation in Field (1965; eq. 15). For both 1-D and 2-D simulations, we use periodic boundary conditions and set the domain size in the x-direction, Δx , equal to the perturbation wavelength $\lambda_x = c_{eq}t_{sc}$. The amplitude of the density perturbation is $\delta\rho = 5.0 \times 10^{-5} \rho_{eq}$.

With this setup, the unstable region of Figure 5.1 is parametrized entirely by ξ_3 , and varying this parameter leads to the formation of clouds with substantially different properties. A realistic value for AGN is likely $\xi_3 = 500$, as this results in a pressure photoionization parameter $\Xi \equiv (F_X/c)/(n_{eq}k_B T_{eq}) \approx 9.0$, and the AGN environment is expected to be hospitable to clouds for $\Xi \lesssim 10$ (e.g., Krolik et al. 1981). For $\xi_3 = 500$, the linear growth rate of the TI is comparatively small, taking more than 400 days for the density of the cold gas to double, and estimates based on Figure 5.1 indicate that a 1-D (or 2-D planar) cloud will form at $\xi_c \approx 20$ with a width $l_c \sim 0.5 \text{ AU}$, a temperature $T_c \sim 4 \times 10^4 \text{ K}$, a number density $n_c \sim 3 \times 10^8 \text{ cm}^{-3}$, and a density contrast of $\chi \sim 30$. The radiation force due to lines can be very powerful, with M_{max} at least 10^3 .

This more realistic cloud is, however, very optically thick for many strong UV lines. (Moreover, as we discuss in §5, it is challenging to accurately resolve in multi-dimensions.) Our present simulations are designed to explore the optically thin regime, as this regime allows us to focus on the

purely hydrodynamical effects of cloud formation and acceleration without the further complications involved when solving the equations of radiation hydrodynamics (RHD; cf. Proga et al. 2014). This restricts ξ_3 to a very narrow range of values corresponding to larger, less realistic values of Ξ , as there is obviously an upper limit on the density of clouds whose acceleration we can accurately model without RHD.

To estimate this upper limit on the density, we assume the cloud forms with both a constant density ρ_c and width l_c (which will be seen to be very nearly the case here), so that we can write $\eta_{\max} = \tau_{L,\max}/\tau_s$, where $\tau_{L,\max} = \kappa_{L,\max}\rho_c l_c$ is optical depth of the thickest line and $\tau_s = \sigma_e \rho_c l_c$ is the electron scattering optical depth of the cloud. Demanding that the cloud to be optically thin to all bound-bound transitions (i.e. $\tau_{L,\max} < 1$) requires $\eta_{\max}\tau_s < 1$, or

$$\rho_c < (\sigma_e l_c \eta_{\max})^{-1}. \quad (5.7)$$

We chose the value $\xi_3 = 190$ since it produces a cloud with the highest density contrast that satisfies this inequality at all times in 1-D. (In §4.4, we verify our optically thin assumption in both 1-D and 2-D using a more accurate estimate.) For $\xi_3 = 190$, M_{\max} does not exceed 40. To explore the effects of the stronger line force, we set $f_{UV} = 10$, which is guided by observational results from Zheng et al. (1997) and Laor et al. (1997).

5.3.2 Simulations

We have performed over 30 simulations exploring a variety of parameters and numerical setups. Here we report in some detail on a set of four simulations that differ only by the applied radiation force: RF (electron scattering only), RFX (electron scattering plus X-ray absorption), RFLD (electron scattering plus line-driving), and RFLDX (electron scattering, line-driving, and X-ray absorption). We will especially focus on run RFLDX, as this case is most representative of the physical conditions in AGN. Compared to a more realistic AGN cloud described above, for our adopted value of $\xi_3 = 190$ the cloud growth is much faster, taking only 2.4 days to double in density, while $l_c \approx 6.5 \times 10^{10}$ cm (0.004 AU), $T_c \approx 7.0 \times 10^4$ K, $n_c \approx 1.4 \times 10^8$ cm $^{-3}$, $\chi \approx 8.0$, and $\Xi \approx 19$. The physical units corresponding to our numerical results are listed in Table 1.

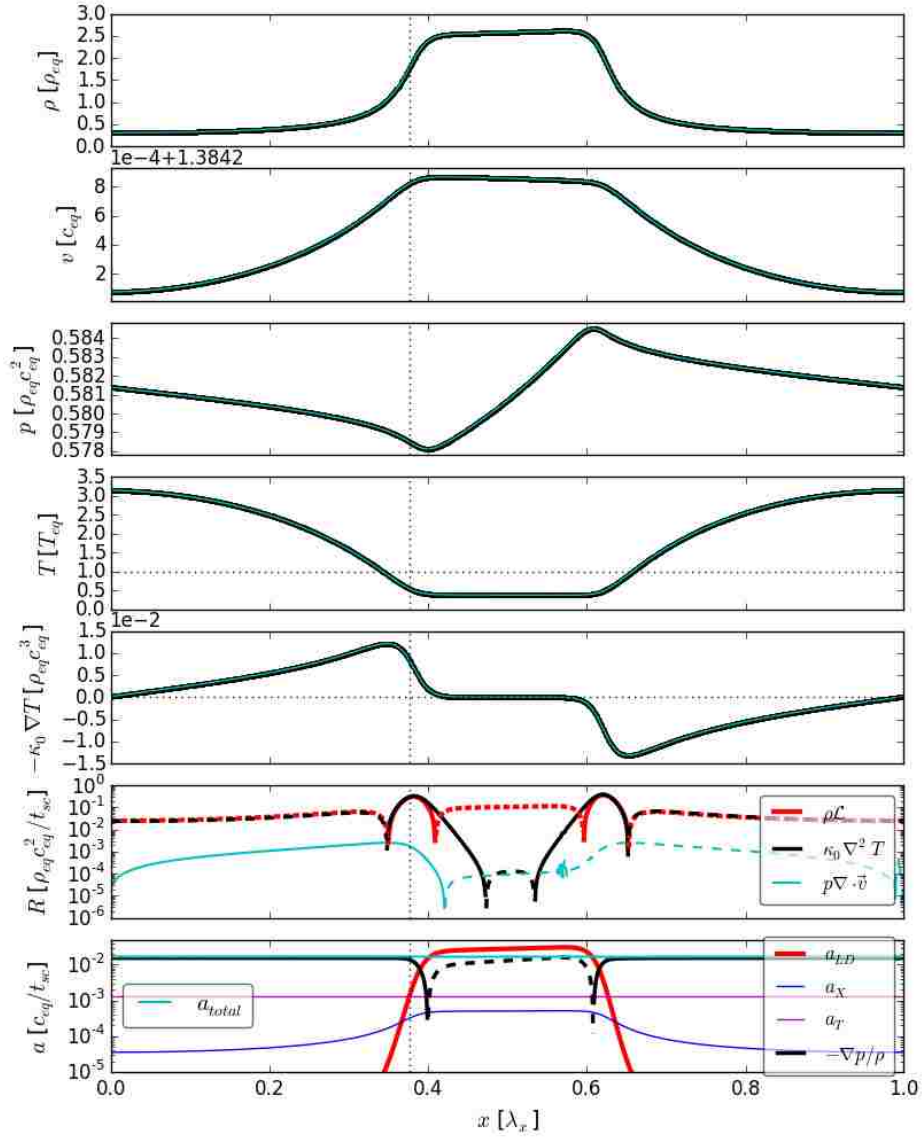


Figure 5.2: Profiles of run RFLDX in 1-D at time $120 t_{sc}$. The resolution is $N_x = 1024$ zones. Numbers above panels are offsets, e.g., the velocity ranges from about $1.3843 c_{eq}$ to $1.3851 c_{eq}$. The dotted vertical line indicates the position of the maximum density gradient. The 2nd from bottom panel compares the heating and cooling rates R in the energy equation, while the bottom panel compares the various accelerations. Solid (dashed) portions of lines in these panels indicate positive (negative) values, e.g. conduction transfers heat into the interfaces at the expense of the medium, while the specific pressure force points to the left (opposite the cloud motion) in the cloud core and to the right elsewhere.

Table 5.1: Physical units (corresponding to $\xi = 190$ & $t_{th}/t_{sc} = 1$)

Quantity	Value (cgs units)
ρ_{eq}	$8.65 \times 10^{-17} \text{ g cm}^{-3}$
n_{eq}	$5.17 \times 10^7 \text{ cm}^{-3}$
T_{eq}	$1.93 \times 10^5 \text{ K}$
c_{eq}	$5.16 \times 10^6 \text{ cm s}^{-1}$
t_{sc}	$6.03 \times 10^4 \text{ s}$
λ_x	$3.11 \times 10^{11} \text{ cm}$
F_X	$7.82 \times 10^8 \text{ erg s}^{-1} \text{ cm}^{-2}$
κ_0	$1.58 \times 10^7 \text{ erg s}^{-1} \text{ K}^{-1} \text{ cm}^{-1}$
Λ_{eq}	$3.97 \times 10^8 \text{ erg g}^{-1} \text{ s}^{-1}$

5.3.3 Results of 1-D Simulations

Despite the different radiation forces, the clouds in all four runs are formed at the same time and with the same density and temperature contrasts, and the gas therefore traces the same ‘tracks’ on the $T - \xi$ plot in Figure 5.1. The over-plotted red and blue dots in Figure 5.1 show the tracks for RFLDX at $t = 120 t_{sc}$, which represents the time where the flow reached a thermal steady state (see below for more details). Note that the red tracks do not reach the radiative equilibrium curve (i.e. $\mathcal{L} = 0$), but rather an equilibrium curve given by $\rho\mathcal{L} = \kappa_0\nabla^2T$.

Also note that there are tracks occupying an unstable (according to Balbus’ criterion) region in Figure 5.1, namely, the tracks within the grey region that are above the dashed line. Given that the gas in the cloud core occupies location 4 and is in pressure equilibrium with the medium, it must be the case that some portion of the gas occupies this unstable region in order for the density and temperature to be continuous everywhere. These tracks correspond to the gas in the conductive interfaces of the cloud. In Figure 5.2, we plot profiles of the solution overplotted in Figure 5.1, and the width of the interfaces can be judged from the density panel. The local Field length in the interfaces is close to the initial equilibrium value, $\lambda_F/\lambda_x = (2\pi/\lambda_x)\sqrt{\kappa_{eq}T_{eq}/(\rho_{eq}\Lambda_{eq})} \approx 0.19$, while the interface width is two or three times smaller than this. Interface gas is permitted to occupy parameter space that is thermally unstable according to Balbus’ criterion because regions smaller than the Field length are stabilized by thermal conduction (measured by the heat flux that is shown in the fifth panel of Fig. 2) and are formally stable to TI according to the generalized criterion (4.54).

We find that in all of these runs the gas arrives at a state of thermal equilibrium by $t = 90 t_{sc}$. The second from bottom panel in Figure 5.2 shows how this equilibrium state is possible. Both the net cooling function (red curve) and the conduction term (black curve) are positive at the interfaces

of the cloud and negative in the hot medium. These terms are of opposite sign in equation (2.40) and therefore balance each other. The compression term (cyan) is negligible at this time, but it was the dominant term when the cloud was forming.

The radiation force prevents the gas from reaching a mechanical equilibrium state. Rather, in each case the cloud core undergoes dynamical changes (i.e. the pressure and velocity profiles adjust) to permit nearly uniform acceleration. To show this, we plot the net flow acceleration in the bottom panel of Figure 5.2 (cyan line), which is the sum of the other curves displayed. Line driving operates almost uniformly throughout the cloud core. As can be seen by either the acceleration or the pressure panel, the response of the gas pressure is to exert a nearly constant drag force on the cloud to compensate for the driving force, while the medium is pushed along since it has nowhere else it can go in 1-D. The adjustment of the forces is obtained shortly after the cloud is formed, with the acceleration profiles resembling those shown in the bottom panel at around $t = 55 t_{sc}$ for runs RFLD and RFLDX. Some profiles (especially velocity) continue to undergo changes until $t = 120 t_{sc}$; the shapes shown in Figure 5.2 are maintained as the cloud continues to accelerate to high Mach numbers.

The results from our 1-D simulations confirm our basic picture for cloud formation and acceleration. As a next step, we perform 2-D simulations where destructive processes may change our results. Our primary concern is the Rayleigh-Taylor (RT) instability, and subsequently the Kelvin-Helmholtz (KH) instability. Figure 5.2 shows that the left interface is RT stable, as the density increases in the direction of acceleration. However, the right interface is likely unstable due to the adverse density arrangement (e.g., Krolik 1977, 1979; Mathews & Blumenthal 1977; Jacquet & Krumholz 2011; Jiang et al. 2013).

5.3.4 Results of 2-D Simulations

The simplest extension of our 1-D simulations to 2-D is to form a cloud with a planar slab configuration. The initial conditions and overall setup is as before. However, to fully explore 2-D effects, we now break the uniformity in the y-direction by introducing a perturbation with a wavelength the size of the domain in the y-direction (i.e. $\lambda_y = \lambda_x/2$) and $\delta\rho = 5 \times 10^{-7} \rho_{eq}$.

In Figure 5.3, we present a comparison of our four 1-D runs and their 2-D counterparts, and we also verify our optically thin assumption. The maximum density of the cloud versus time is plotted in the top panel. It is clear that there is no significant difference in any of the runs during the cloud

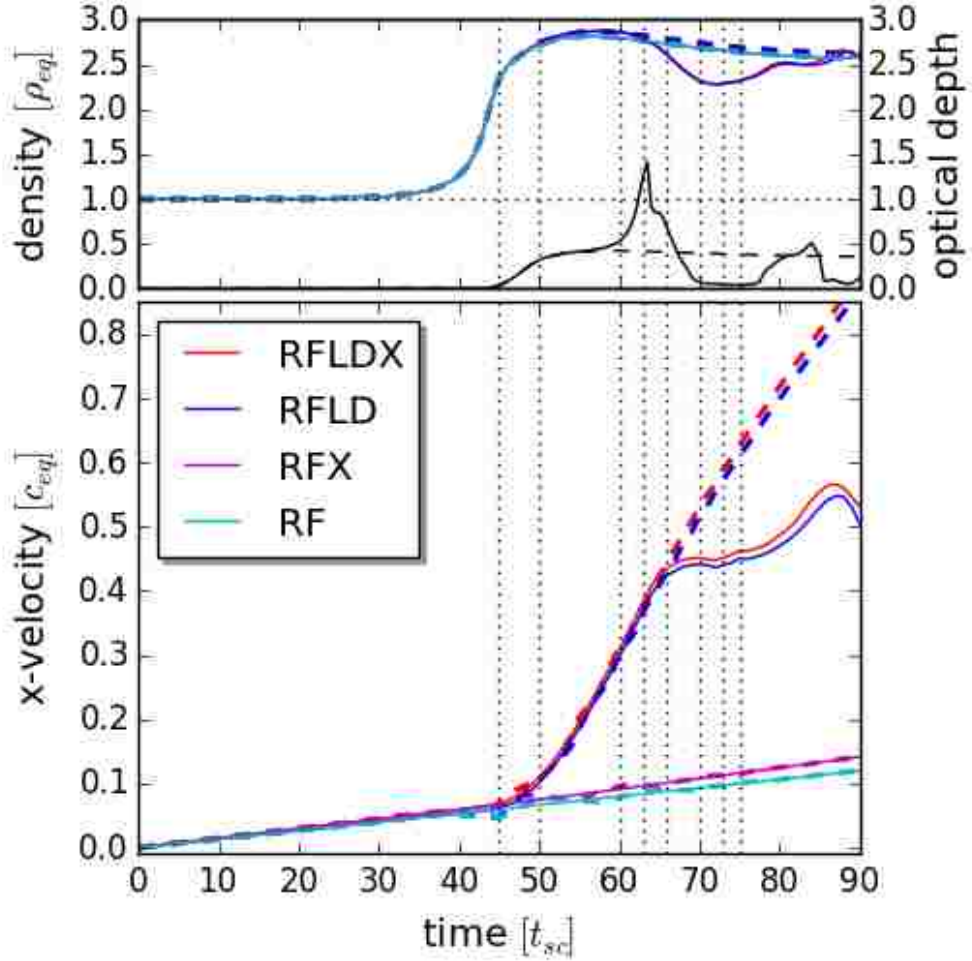


Figure 5.3: Comparison of all runs in 1-D and 2-D. Dashed (solid) lines denote 1-D (2-D) runs. In both panels, all curves nearly overlap during the nonlinear cloud formation process, which completes at time $\approx 50 t_{sc}$. In the top panel, we also verify that the cloud in run RFLDX is optically thin to UV radiation by calculating an estimate to the optical depth using equation (5.8). This estimate in 1-D (2-D) is given by the dashed (solid) black line. The dotted vertical lines mark the times corresponding to the snapshots in Figure 5.4.

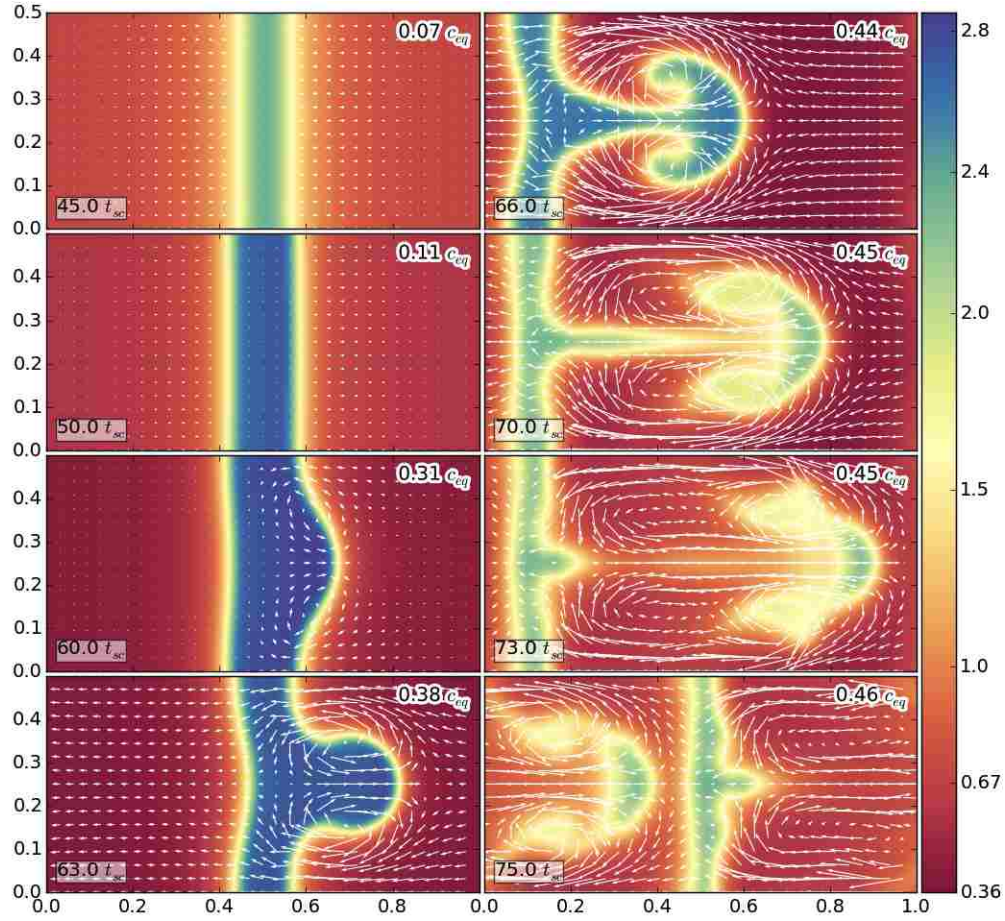


Figure 5.4: Density snapshots of run RFLDX in 2-D in units of ρ_{eq} . The domain size is $[\lambda_x, \lambda_x/2]$ with resolution $[N_x, N_y] = [1024, 512]$. Since the cloud continually advects through the domain boundaries, the images are manually aligned for visual comparison. Velocity arrows are overlaid after subtracting the mean x-velocity of the cloud (displayed in the upper right corner) from v_x , the cloud being defined as gas with $\rho > 1.57\rho_{eq}$. Time is shown in the lower left corner of each panel.

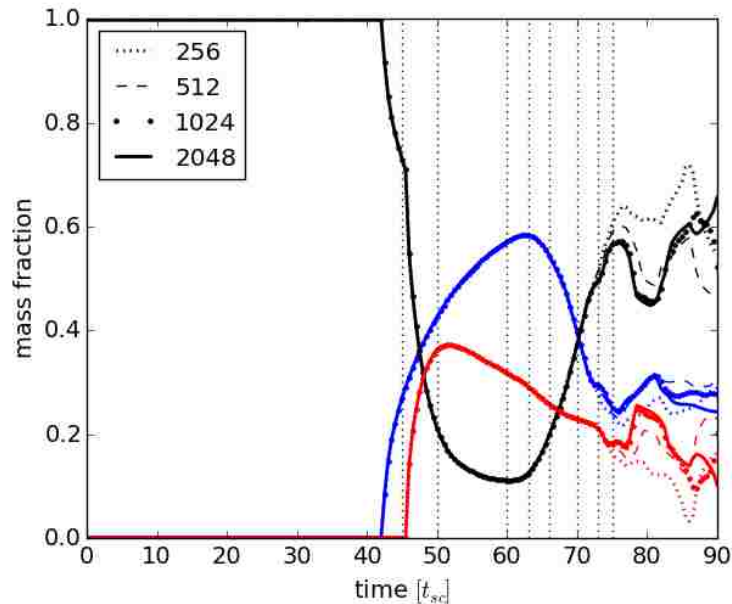


Figure 5.5: Mass fractions for run RFLDX in 2-D at four different resolutions. Blue, black, and red curves track the fraction of the gas contained in the cloud, the interfaces, and the medium, respectively; our method of differentiating these regions is described in §4.4. The dotted vertical lines mark the times corresponding to the snapshots in Figure 5.4. The mass fraction of the cloud monotonically increases until the RT spike becomes fully nonlinear, after which it begins to monotonically decrease until the spike becomes a detached structure. At this point our results become resolution dependent.

formation process, which ends at $t \approx 50t_{sc}$. As mentioned in §4.1, for runs RFLD and RFLDX to be optically thin to UV photons, we require $\tau_{L,\max} < 1$. We estimate $\tau_{L,\max}$ as ²

$$\tau_{L,\max} = \sigma_e \int_0^{\lambda_x} \eta_{\max,90}(x) \rho(x) dx, \quad (5.8)$$

where $\eta_{\max,90}$ denotes only those values of η_{\max} in the range $[0.9\eta_{\max}, \eta_{\max}]$. We use this range to be able to identify gas at a constant opacity in our numerical representation of η_{\max} . The black curves in the top panel of Figure 5.3 show this estimate for $\tau_{L,\max}$ in both 1-D (dashed line) and 2-D (solid line). In the latter calculation, we consider a ray through the center of the cloud at $y = 0.25\lambda_x$. Overall, the cloud can indeed be considered optically thin at all times, except possibly at its center during a very short period of the acceleration phase in 2-D, which as will be made clear below, coincides with when the cloud is significantly lengthened by the onset of disruptive processes.

The bottom panel of Figure 5.3 shows the average velocity of the cloud versus time, where we

²Note that the ‘expanding’ optical depth formula, $\tau_{L,\max} = \sigma_e \eta_{\max} \rho v_{th} |dv/dx|^{-1}$ (see CAK) is not valid here because the Sobolev length $v_{th}/|dv/dx|$ is much greater than the density scale height. That is, the scale over which the velocity changes by the thermal width of the line ($v_{th} \sim 20 \text{ km s}^{-1}$) is much greater than the interface width ($\sim \lambda_F$), the scale over which the density (and hence opacity) changes appreciably.

define the cloud as being the gas to the left of the grey region in Figure 5.1 (i.e. $\xi < 121.2$, which corresponds to $\rho > 1.57\rho_{eq}$). It indicates that significant acceleration only takes place after the cloud formation process has ended, as line opacity is only activated once the cloud forms. While 1-D runs of RFLD and RFLDX uniformly accelerate to supersonic speeds, the acceleration is suddenly halted in 2-D around $t \approx 66t_{sc}$.

In Figure 5.4, we plot snapshots of run RLFDX, to illustrate the very different fate of a rapidly accelerated cloud in 2-D. The first frame shows that the slab formed at $t = 45t_{sc}$. The initial perturbation in the y-direction grows into a slight over-density region in the center of the slab, which then undergoes greater acceleration than its surroundings and causes a small bulge to appear around $t \approx 55t_{sc}$ (not shown). Viewing this bulge as a perturbation along the surface of the slab, the basic criteria for the RT instability is satisfied: heavy fluid is pushing against light fluid. The same conclusion applies to runs RFX and RFLD, although for run RFX it will take much longer (several hundred t_{sc}) for the bulge to grow due to the weak acceleration. Run RF, however, which has a constant acceleration due to Thomson opacity, evolves identically in 1-D and 2-D for all time; any density perturbation in the y-direction receives the same push as any other point in the flow.

The remaining frames in Figure 5.4 reveal how the breakup of the cloud ensues as the RT instability develops and soon becomes accompanied by the KH instability. First the bulge evolves to become mushroom-shaped, forming a structure resembling the classic RT ‘spike’, which features prominent KH ‘rolls’ at $t = 66t_{sc}$ made possible by the increased relative velocity between the cloud and medium. The halting of the acceleration happens around this time. The connecting plume then disperses (i.e. its gas is heated) as the spike separates further from the slab. The slab would likely disperse also, due to the mass lost to the spike, but instead it is somewhat thickened by the approach of the spike from the backside. This collision perspective is shown in the final panel at $t = 75t_{sc}$.

The cloud is eventually either completely dispersed back into the medium, or coexists with it in a disordered manner in what could be called a clumpy flow once the vertical symmetry is lost. The simulations presented here do not let us make any definitive statements because we noticed that our solutions become resolution dependent at about time $73t_{sc}$ for run RFLDX. This loss of convergence is shown in Figure 5.5, where for four different resolutions, we plot the mass fraction of the three components of the gas: (i) the cloud (blue), again defined as gas with $\xi < 121.2$ or $\rho > 1.57\rho_{eq}$ (ii) the interface (black), defined as the portion of the gas in the grey region that is unstable, i.e. the tracks above the dashed line in Figure 5.1 with $121 \leq \xi \leq 278$ or $0.68\rho_{eq} \leq \rho \leq 1.57\rho_{eq}$; (iii) the medium (red), defined as the (stable) gas with $\xi > 278$ or $\rho < 0.68\rho_{eq}$. The mass fraction is defined

as the mass of each component divided by the total mass and is given by $m = (N_x N_y)^{-1} \sum_{ij} \rho_{ij} / \rho_{eq}$, where N_x and N_y are the number of grid zones in the x and y directions and the sum ranges over all zones (i, j) that satisfy one of the criteria (i)-(iii). Once the mass fractions for resolutions $N_x = 1024$ and $N_x = 2048$ differ, we cannot claim to accurately follow the cloud's evolution.

The mass fractions provide a complementary description of the cloud evolution depicted in Figure 5.4. The cloud appears fully formed by $t \approx 50 t_{sc}$, which coincides with the peak mass fraction of the medium, but mass keeps piling on until $t \approx 63 t_{sc}$. Indeed, we observe that the velocity arrows at $t = 50 t_{sc}$ in Figure 5.4 point toward the cloud, indicating continued growth at the expense of the medium. The overall fraction of gas occupying interface regions is a minimum at $t \approx 60 t_{sc}$, and this is despite the overall increase in the size of interface region (due to the bulge) because the interfaces are narrower. The cloud mass fraction reaches a maximum at $t \approx 63 t_{sc}$ when the RT spike has become fully nonlinear, and thereafter monotonically decreases, with the mass being taken up entirely in the interfaces, until the RT spike becomes detached from the slab. During this time, the medium continues losing mass to the interfaces. The loss of convergence is likely due to the appearance of small scale structures as the cloud is disrupted.

5.4 Discussion

As the next planned phase of our ongoing investigation of cloud acceleration initiated in Proga et al. (2014), this chapter considered the cloud formation and acceleration processes simultaneously for the first time. In particular, we have extended the basic theory of the nonlinear outcome of TI by self-consistently solving for the dynamics of optically thin gas in the presence of a strong radiation field. Our resulting simulations have made it possible to study in detail the evolution of the isobaric condensation mode in thermally unstable gas from an initial perturbation to a dense, high velocity cloud. The cloud forms in a radiation pressure dominated environment, but the radiation force has practically no effect on the cloud formation process in either 1-D or 2-D. The reason is simply because there is no momentum transfer from the radiation to the gas unless there is also sufficient opacity, and the sources of opacity are not activated until the cloud is formed.

The initial motivation for this work was simply to demonstrate that the nonlinear phase of TI leads to a natural mechanism to produce fast clouds via acceleration due to lines. In so doing we were led to the inescapable conclusion that accelerated clouds undergo rapid deformation and are ultimately destroyed, thereby confirming long-standing assertions about the inevitability of

cloud destruction (e.g., Mathews 1986; Krolik 1999 and references therein). However, we find that optically thin clouds can survive long enough to be accelerated to relatively high velocities and travel a significant distance of many cloud sizes, in contrast to investigations exploring pre-existing optically thick clouds (Proga et al. 2014 and references therein.) Consequently, the best hope for cloud-based models of AGN is to identify robust mechanisms for continually producing clouds (e.g., in “outflows from inflows” as illustrated in simulations presented by Kurosawa & Proga 2009 or Mościbrodzka & Proga 2013). It is therefore important to thoroughly study how clouds form via TI and how they evolve before disruptive processes take hold.

We found that a rich set of dynamics unfolds during the cloud formation process. For example, for run RFLDX (radiation force due to X-rays and lines) in 1-D, there are three nonlinear phases of the TI: (i) initial growth and saturation ($t \approx 40 - 46 t_{sc}$); (ii) evolution toward a uniformly accelerating solution ($t \approx 46 - 55 t_{sc}$) (iii) evolution toward a thermal equilibrium state ($t \approx 46 - 90 t_{sc}$). Figure 5.4 shows that phases (i) and (ii) have both completed before the RT instability can develop, so these phases also take place in 2-D, while phase (iii) has a different outcome in 2-D and the uniform acceleration cannot be maintained.

More effort is needed to investigate the growth of the RT and KH instabilities. This is an important matter since the appearance of these instabilities governs the end phase of TI and therefore dictates the ultimate fate of the cloud. These instabilities develop after the TI saturates. Therefore, it should be possible to confirm the theoretical linear growth rates by conducting a careful numerical perturbation analysis (e.g., by introducing sinusoidal perturbations along the interfaces of a 2-D planar slab initialized using a 1-D solution). That said, we did not find it possible to make a meaningful comparison of the growth rate of the bulge and the classical RT rate in the present setup. Recalling Figure 5.3, the bulge is already borderline nonlinear by $t = 60 t_{sc}$, implying that the slab is still evolving thermally [i.e. in phase (iii) of nonlinear TI evolution] during the linear RT growth regime. This dynamical complication combined with the simplifying assumptions inherent in the linear theory for RT (such as constant acceleration everywhere) warrant using a more controlled approach for isolating the development of the individual instabilities.

The numerical setup presented here can be used for several different exploratory studies of cloud formation and acceleration. We chose the initial perturbation amplitude $\delta\rho$ in the y-direction to be 10^{-2} that in the x-direction in order to arrive at a slab configuration. With an equal ratio (and equal growth rates), a round cloud will be formed in 2-D instead. Multiple clouds can be formed using higher wavenumber perturbations. Cloud fragmentation can be studied by decreasing the ratio

t_{th}/t_{sc} . ‘Classical’ evaporation (Cowie & McKee 1977; Balbus 1985) can be explored by arranging for the Field length to exceed the size of the cloud. This large range of initial configurations would be difficult or impossible to construct otherwise, which illustrates an obvious advantage of studying cloud acceleration via the formation process, namely that the internal gas dynamics is self-consistently treated. Indeed, we find that pressure equilibrium with the surrounding medium is naturally maintained, cloud interfaces form with a width determined by the conductivity, the radiation and drag forces reach a balance so that hydrostatic equilibrium is established in the reference frame of the cloud, and the cloud reaches a thermal equilibrium state in which heating by conduction is balanced by line cooling, in agreement with Begelman & McKee (1990). Moreover, the equilibrium location on the S-curve largely determines the cloud density, temperature, and opacity before it is accelerated, while plotting the evolutionary tracks on the $T - \xi$ plane has shown itself to be a useful tool both for understanding the time evolution of the cloud and for characterizing the components of the gas.³

Taking into consideration the numerical requirements involved in this study, multi-dimensional simulations will likely be constrained to only explore values of $\xi_3 \lesssim 300$ for the S-curve used here, thereby limiting the overall density contrast of clouds to $\chi \approx 18$. This limitation arises due to the need to resolve interfaces, as simulations of clouds formed via TI will not be converged unless the conductive interfaces are resolved (Koyama & Inutsuka 2004). Previous numerical studies using pre-existing clouds without thermal conduction and with unresolved interfaces were able to explore much higher density contrasts such as $\chi = 50$ (McCourt et al. 2014) and even $\chi \sim 10^4$ (Krause et al. 2012). We found that a realistic $\kappa \propto T^{5/2}$ would require upwards of $N_x = 4,096$ zones (i.e. at least three levels of refinement if adaptive mesh refinement is employed) even for our modest density contrast of $\chi \approx 8$, as would values of $\chi \gtrsim 30$ with continued use of a constant conductivity. This rapid steepening of the interfaces with either increased χ or realistic $\kappa(T)$ results in ever smaller transition regions between the cloud and the medium but does not imply that the role of thermal conductivity becomes less important. As a consequence, the conduction time step would be so small at these resolutions that even STS schemes would become impractically slow, necessitating the use of implicit techniques. Such extensions to this work may be needed to assess, for example, if the timescale for cloud destruction is sensitive to the slope of the interfaces, i.e. if it decreases with steeper density gradients, as was found to be the case when a cloud is disrupted by the passage of a shock (Nakamura et al. 2006).

³Simulations demonstrating this can viewed online at www.physics.unlv.edu/astro/pw15sims.html

Chapter 6

EFFECTS OF FLUX VARIABILITY

6.1 Introduction

Motivated by multi-wavelength observations of rapid variability (on timescales of hours to days) that are overall suggestive of AGN variability being intrinsic rather than absorption driven (see Uttley & Casella 2014 for a review), in this chapter we set out to relax our assumption of a constant flux and show that this can further enhance the coupling between the gas and radiation field. To see that a time-varying flux leads to an additional acceleration mechanism, note the expected asymmetric response of gas that is not fully ionized: during low flux states when the gas can cool, the increase in the radiation pressure force can be substantial because the line opacity is a sensitive function of temperature.

This chapter is organized as follows. In §6.2 we discuss our modifications to the methods developed in the last chapter. We hereafter refer to those methods as PW15 since they were published by Proga & Waters (2015). In §6.3, we present our results, verifying that this acceleration mechanism is realized, even in 2D. In §6.4 we discuss the implications of these results.

6.2 Methods

The equations we solve differ from those in the last Chapter only by the introduction of an oscillating ionizing flux,

$$F_{\text{ion}}(t) = F_X + \Delta F_X(t) = F_X (1 + A_X \sin(2\pi\omega_X t)), \quad (6.1)$$

where A_X and ω_X denote the amplitude and frequency of oscillations. The constant (time-averaged) ionizing flux F_X is set once values for the photoionization parameter and number density characteristic of the AGN environment are chosen, and we explore a slightly modified set of units in this chapter. Namely, we still adopt $\xi_{eq} = 190 \text{ erg cm s}^{-1}$ but we increase the density to $n_{eq} = 10^{14}/T_{eq}$, yielding $n_{eq} = 5.17 \times 10^8 \text{ cm}^{-3}$ and $F_X = 7.82 \times 10^9 \text{ erg s}^{-1} \text{ cm}^{-2}$. This choice leads to an acceleration timescale that are more in agreement with the observational requirements. The the radiation

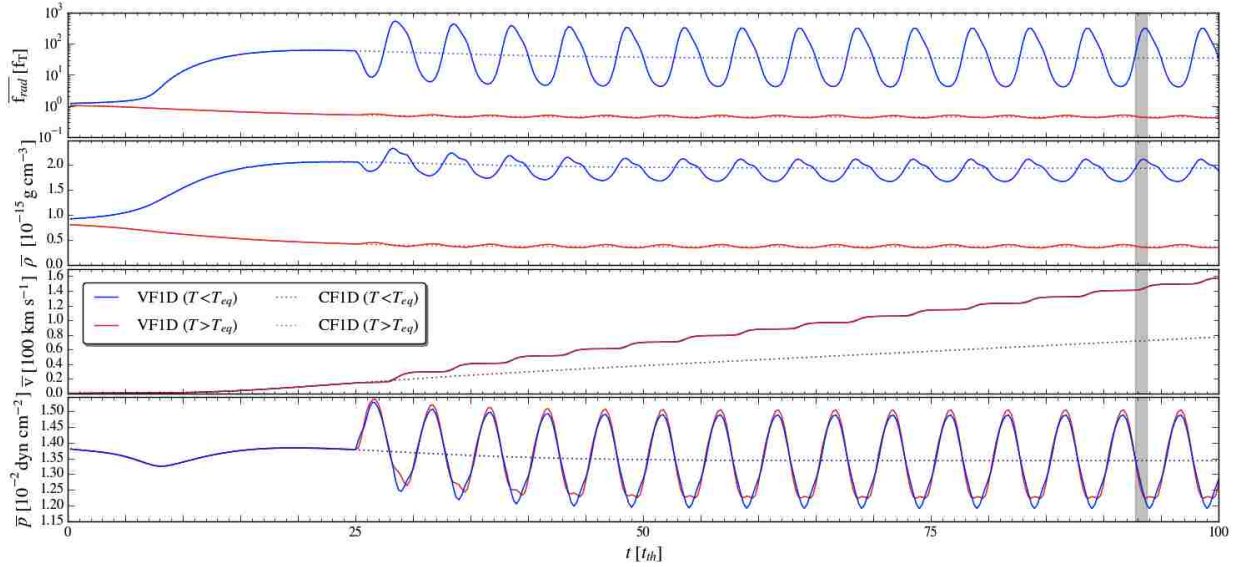


Figure 6.1: Temporal properties of 1D simulations. Solid lines denote the constant flux run VF1D and dotted lines the time-varying flux run CF1D. Red and blue colors denote averages over gas that is above and below, respectively, the equilibrium temperature $T_{eq} = 1.93 \times 10^5$ K. In the top panel, f_{rad} is plotted in units of the force from Thomson scattering for gas with $T = T_{eq}$, namely $f_T = \rho_{eq} \sigma_e (F_{UV} + F_X) / c$ [$\text{g cm}^{-2} \text{s}^{-2}$]. The grey region highlights the quarter cycle corresponding to the solutions plotted in Figure 6.2. The velocity panel shows that a 20% variation in flux increases the net flow acceleration by about 240%.

force becomes, instead of (5.3),

$$\mathbf{f}_{rad} = \frac{\rho \kappa_e}{c} \left[(1 + M_{\max}) F_{UV} + (1 + \sigma_X) F_{\text{ion}}(t) \right] \hat{r}. \quad (6.2)$$

The amplitude of the density perturbation was increased from $\delta\rho/\rho_{eq} = 5 \times 10^{-5}$ to $\delta\rho/\rho_{eq} = 0.1$ in order to shorten the duration of the initial phase of cloud evolution; this had no noticeable effect on subsequent evolution. We use periodic boundary conditions in order to track the acceleration of the cloud over many domain lengths (a domain length is $l_x = 3.11 \times 10^{10}$ cm). Our simulations were performed on a uniform grid with resolution $N_x = 1024$ in 1D and $[N_x, N_y] = [2048, 1024]$ in 2D.

The effects of a time-varying flux would be minimal if clouds evaporated back into the confining medium at a much higher rate than new clouds are created. The results of the previous chapter, however, are suggestive of a scenario in which continuous cloud production can sustain a significant cloud mass fraction despite losses from evaporation. This finding implies that a turbulent flow regime with qualitatively similar properties is reached nearly independent of the initial conditions. Hence, it suffices to simply consider the simulations from PW15 and run them for a longer time.

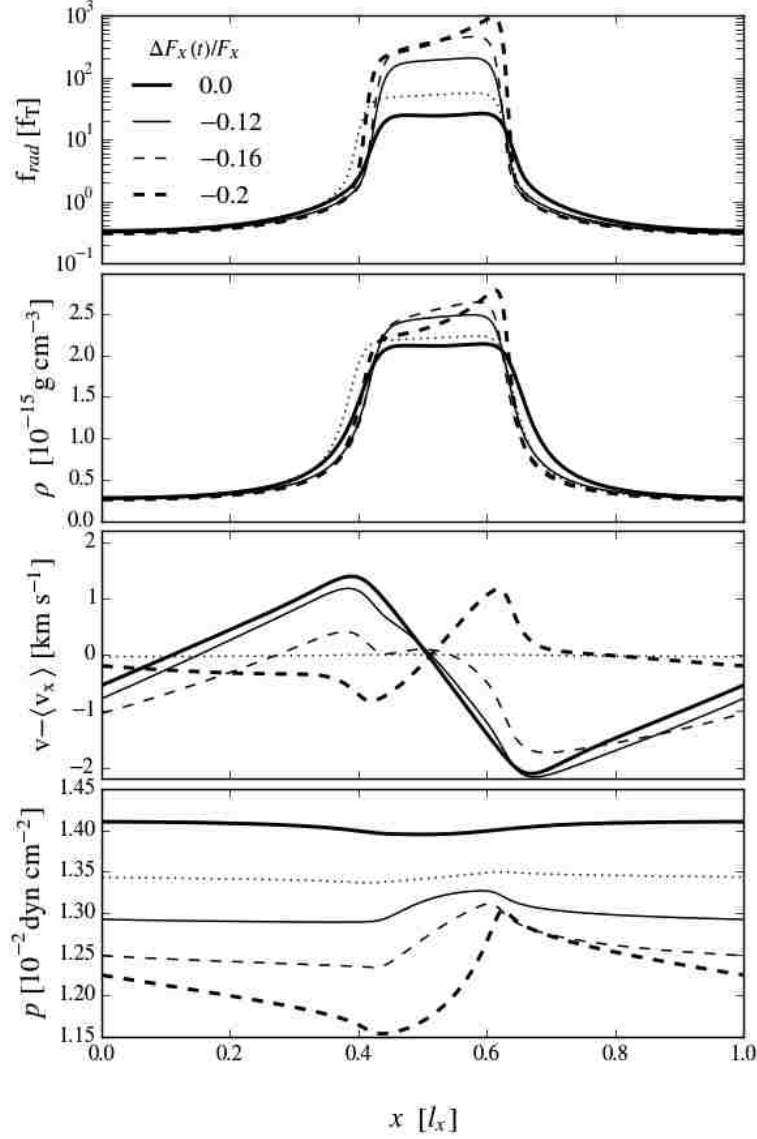


Figure 6.2: Spatial profiles in the comoving frame of the cloud. These profiles are for the quarter cycle (highlighted in grey in Figure 6.1) when the variable flux transitions from its equilibrium ($\Delta F_X = 0$; thick solid line) to its minimum ($\Delta F_X = -0.2 F_X$; thick dashed line) value. The thin solid and dashed lines are intermediate profiles with values of $\Delta F_X/F_X$ shown in the legend. The dotted profiles are the solutions for (constant flux) run CF1D. See the caption of Figure 6.1 for the definition of f_T .

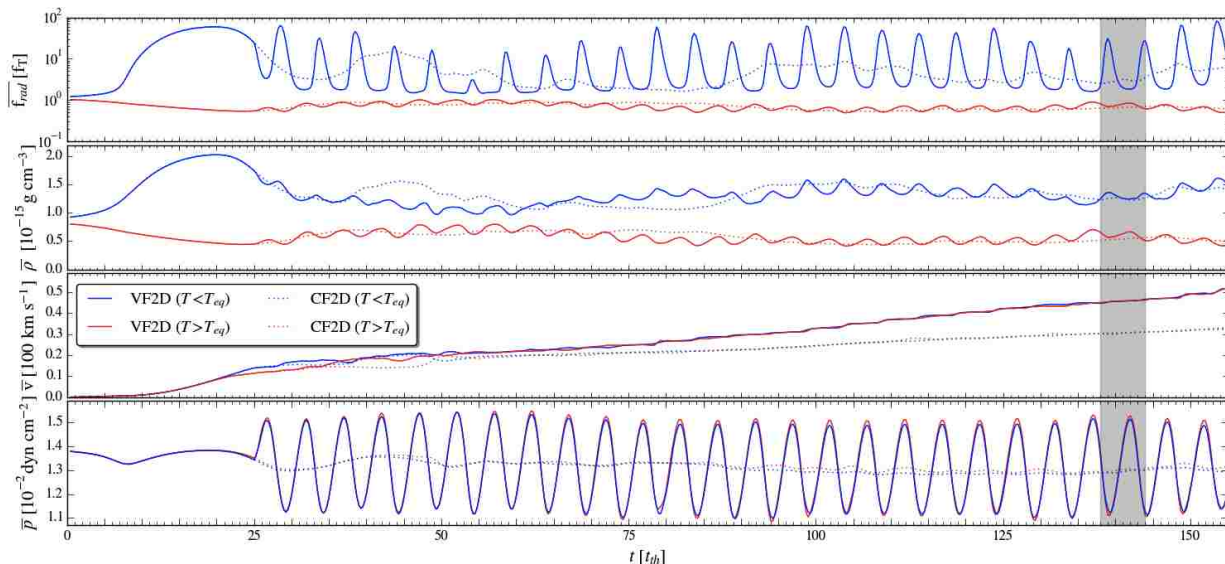


Figure 6.3: Same as Figure 6.1, but for 2D simulations run for 155 thermal times. The grey region now highlights a duration spanning 1.25 cycles; snapshots of each quarter cycle are plotted in Figure 6.4. Once again, the velocity panel shows that a 20% variation in flux increases the net flow acceleration by about 240%.

6.3 Results

We ran over 20 simulations to explore the parameter space (A_X and ω_X) introduced by the time-varying flux. Typical rms variability amplitudes observed in reverberation mapping campaigns are $\lesssim 20\%$ (e.g., De Rosa et al. 2015). For amplitudes this small, we expect there to be a limited range of periods $t_X = 1/\omega_X$ that can significantly affect cloud acceleration. If the flux varies rapidly, such that $t_X \ll t_{\text{th}}$, the gas will not have time to respond. The opposite regime with $t_X \gg t_{\text{th}}$ would likely be very inefficient, as our results show that each low flux state provides a gentle ‘kick’ to the cloud.

Here we present results for two simulations carried out in both 1D and 2D. Runs CF1D and CF2D (CF for ‘constant flux’) are identical to the fiducial runs from PW15; VF1D and VF2D (VF for ‘variable flux’) are new simulations and differ only by the introduction of $\Delta F_X(t)$. We adopted $t_X = 5 t_{\text{th}} \approx 0.35$ days. We do not introduce this time-varying flux until the cloud has fully formed. In practice, we set $A_X = 0$ if $t < 25 t_{\text{th}}$ and $A_X = 0.2$ for $t \geq 25 t_{\text{th}}$.

6.3.1 1D Simulations

In PW15 we showed that equations (1)-(3) reach a simple steady state solution in 1D when the flux is constant. Here the 1D solutions are much more complex and naturally time-dependent, but they

are perfectly cyclic in that profiles of the solution at late times satisfy $q(x, t) = q(x, t + t_X) + q_0$, where q is any variable and q_0 is a constant. This property is most easily shown by plotting spatially averaged quantities over time, as shown in Figure 6.1. Here the instantaneous values of the radiation force and primitive variables are averaged over the hot gas ($T > T_{eq}$; red curves) and cold gas ($T < T_{eq}$; blue curves). Since the density and pressure averages are bounded by the same values for $t \gtrsim 40 t_{th}$, we have $q_0 = 0$ for ρ and p , indicating that a stable configuration permitting cyclic episodes of enhanced cloud acceleration has been reached. For comparison, the dotted lines in Figure 6.1 are these same quantities for run CF1D.

Comparing red and blue curves in Figure 6.1, we see that our basic expectations are confirmed: low flux states lead to decreases in temperature, which for the cold gas results in accompanying increases in density (due to the tendency to maintain pressure equilibrium) as well as corresponding increases in the radiation force. At $t = 25 t_{th}$, the flux oscillations commence, beginning with a high state from $t = 25.0 - 27.5 t_{th}$. The resulting increase in temperature is reflected by the initial rise in pressure in the bottom panel, and the cold and hot gas pressures are closely in sync, explaining the initial drop in the density of cold gas. (The much smaller rise in the density of the hot gas is slightly delayed, indicating that this is a hydrodynamic response to the cold gas.) The ‘kick’ imparted by the radiation force happens in the next quarter cycle from $t = 27.5 - 28.75 t_{th}$. The grey shaded region highlights this interval at a later time, showing that the slope of the velocity is steepest during this quarter cycle.

In Figure 6.2 we investigate the detailed dynamics of the cloud during this acceleration phase of the cycle. The two thick lines are profiles of the solution corresponding to times at the boundaries of the shaded region in Figure 6.1. The top panel shows that a 20% variation in flux leads to more than an order of magnitude increase in the radiation force for run VF1D compared to run CF1D during this phase of the cycle. The cloud responds to this force by dramatically altering its configuration. For the cloud to remain in near pressure equilibrium with the hot medium and yet cool (reflected by the overall decrease in pressure in the bottom panel), its density must increase. This in turn can only occur through a bulk transfer of mass from the hot medium, hence the prominent positive and negative peaks on the velocity profile, which are maintained for about a third of the quarter cycle. This advective mass transport though both interfaces of the cloud suddenly becomes much weaker through the left interface (see the thin dashed line), leading to a marked density increase of the leading edge of the cloud. Meanwhile, the pressure gradient in the core has progressively steepened, indicative of the increasing drag as the radiation force increases.

The final velocity profile (thick dashed line) indicates that the bulk mass transfer opposes continued growth and will instead lead to a net expansion of the cloud. In the next quarter cycle (not shown, but see Figure 6.1), the cloud density drops back to its starting level in Figure 6.2, and then continues to further decrease as the flux increases, causing the temperature to rise and the cloud to expand. The term representing $p dV$ work, $p \nabla \cdot \mathbf{v}$, is critical for mediating the transition between high and low flux states. However, in the steady state $p dV$ work does not play a role since $\nabla \cdot \mathbf{v} = -\rho^{-1} D\rho/Dt$, and $D\rho/Dt$ reaches 0 for run CF1D. When time-varying radiation forces are involved, this term is important.

6.3.2 2D Simulations

The setup for our 2D simulations is the same as in PW15: we arrange for a plane parallel cloud (a slab) to be formed by making the magnitude of the density perturbation in the y -direction 2 orders of magnitude smaller than that of the x -direction: $(\delta\rho)_y/\rho_{eq} = 10^{-3}$. This perturbation triggers the Rayleigh-Taylor instability, as the core of the slab is slightly ‘heavier’ than its surroundings under the effective gravity of the radiation force, and it ‘falls’ into the hot medium. At $t = 25 t_{\text{th}}$ when we apply the variable flux, the Rayleigh-Taylor plume is fully developed (and similar to the configuration shown in the top right panel of Figure 4 in PW15).

Figure 6.3 is the 2D counterpart to Figure 6.1. A two-phase medium clearly exists for the duration of the run, i.e. evaporation does not dominate new cloud production. While the generation of turbulence prevents an orderly cyclic solution, the behavior is qualitatively the same as in 1D. There are substantial quantitative differences: the average density of the cold gas never exceeds its maximum at $t \approx 20 t_{\text{th}}$ and the radiation force is correspondingly weaker; hence, the velocities are greatly reduced. Importantly, however, the ratio of the net accelerations for runs VF2D and CF2D is approximately the same as that for runs VF1D and CF1D — a factor of 2.4. This implies that the effect of a variable flux is quite robust.

The right panels in Figure 6.4 show density maps of run VF2D for five consecutive, quarter-cycle flux states (denoted A-F in the sine-wave sketch), while the left panels are the corresponding density maps for run CF2D. During both of the minimum flux states (panels B and F), the density is noticeably increased, as hydrodynamic effects akin to those depicted in Figure 6.2 are taking place. Velocity arrows are overlaid in the comoving frame in order to portray the local velocity field; they reveal the pronounced *vortical* motions of the clouds, indicative of the large amount of vorticity in

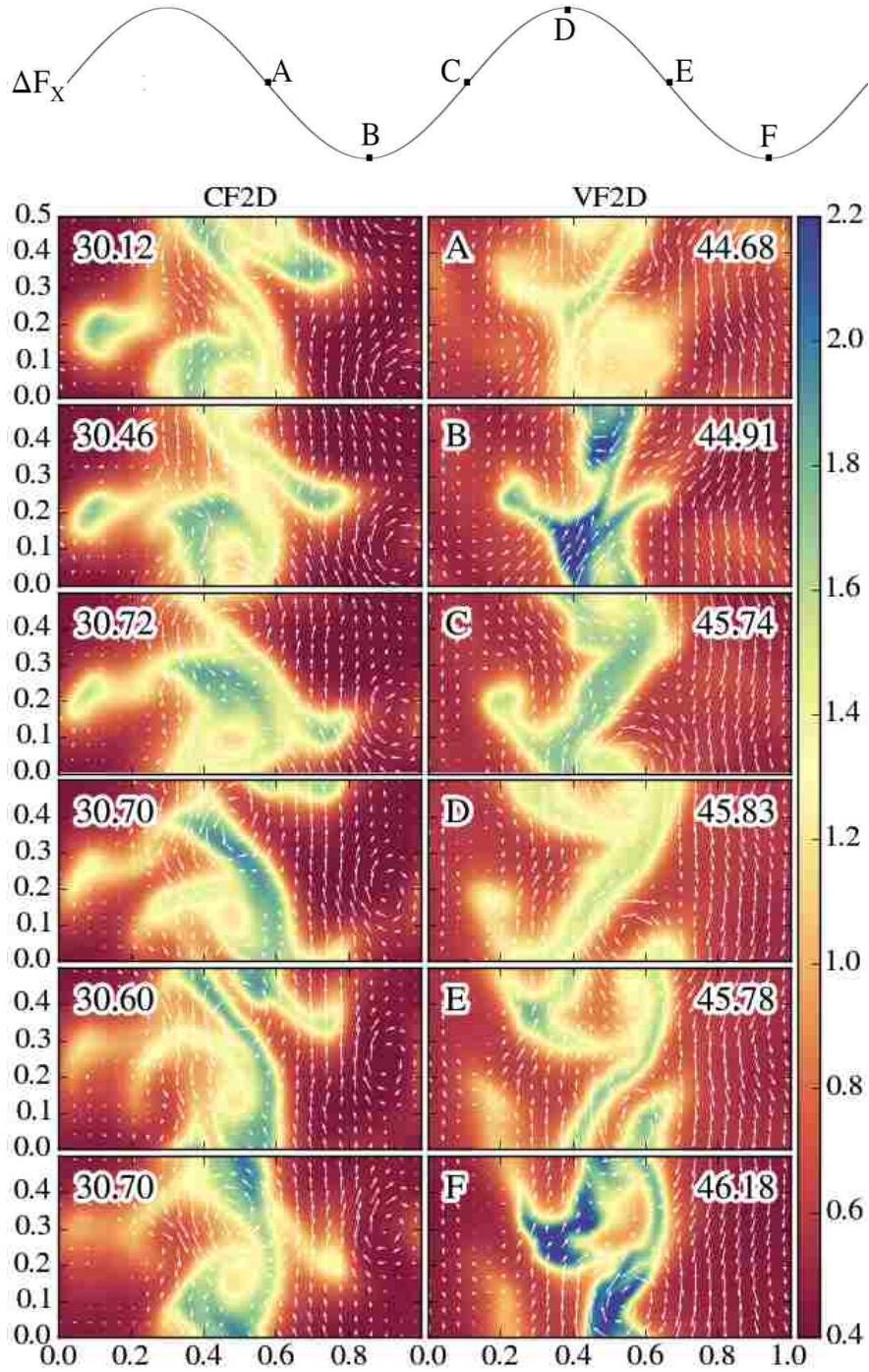


Figure 6.4: Density maps of our 2D runs. The colorbar values are in units of $10^{-15} \text{g cm}^{-3}$. Panels A-F on the right show snapshots of run VF2D every quarter cycle of the flux oscillation, as sketched above. The left maps are for run CF2D at the same times. Velocity vectors are overlaid after subtracting $\langle v_x \rangle$, the mass-weighted mean of v_x . This value is displayed on every panel in km s^{-1} to show the enhanced acceleration during low flux states. (The mass-weighting allows $\langle v_x \rangle$ to decrease.)

the flow. The mass-weighted mean velocity, $\langle v_x \rangle$ (in km s^{-1}), is displayed on the corner of each panel in order to judge the net acceleration. The main noticeable effect is that during the low flux states, there are large increases in velocity compared to run CF2D.¹

6.4 Discussion

As part of our ongoing effort to understand the dynamics of BLR clouds from first principles, we have investigated the dynamical response of a two-phase medium to a time-varying flux. Our main result is that small flux oscillations ($\Delta F_X = 20\%$) can lead to large changes in the net acceleration (240%), even in 2D where the flow becomes highly turbulent. The physics of this process is cleanly revealed in 1D, where a cyclic solution was found. During every low flux state, the gas cools, allowing additional lines to appear that more strongly couples the gas to the radiation field and further accelerates the cloud via line driving.

Crucially, gas pressure effects are very important in mediating the transition between flux states, thereby permitting the density to respond to the changes in temperature. Simply lowering the flux to its minimum value and then holding it fixed does not lead to an increase in acceleration; an explicit calculation revealed that in both 1D and 2D the final velocities were actually 4% smaller than those for runs CF1D and CF2D. In other words, a time-varying flux leads to a gas pressure dominated, time-dependent solution that is qualitatively different from a constant flux solution.

This finding may have interesting observational consequences and important implications for photoionization modeling efforts. For example, the responsivity of the BLR gas (Krolik et al. 1991; Peterson 1993) is a central quantity in reverberation mapping (RM) and transfer functions have been shown to be sensitive to how this quantity scales with radius (Goad et al. 1993). A negative responsivity, i.e. a decrease in line emission in response to an increase in the continuum flux, is readily interpreted as emission from optically thin clouds (Sparke 1993) and has been seen in X-ray RM observations (McHardy et al. 2007; Fabian et al. 2009). Photoionization models have difficulty accounting for this effect and simultaneously reproducing the observed line strengths (Shields et al. 1995; see also Snedden & Gaskell 2007). The hydrodynamic effects associated with our present solutions — significant decreases in density accompanying high flux states — would naturally be expected to give rise to a negative responsivity, although they would complicate the analysis of time-delays in RM as they are a nonlinear response (e.g., Skielboe et al. 2015). To resolve the issue

¹Both 1D and 2D simulations can viewed online at www.physics.unlv.edu/astro/wp16sims.html

with line strengths, photoionization models may need to incorporate results from time-dependent hydrodynamics.

Chapter 7

SYNTHETIC ABSORPTION LINES AND A SPECTRAL SIGNATURE FOR CLOUD ACCELERATION

7.1 Introduction

In this chapter, we set out to calculate synthetic absorption line profiles for the simulations of the previous two chapters, which probe a temperature regime appropriate for modeling warm absorbers. In particular, we sought to answer the following questions: (1) is it possible to differentiate, spectroscopically, between an ideal, comoving cloud (i.e. of planar or round geometry), a cloud being disrupted as it accelerates through its surrounding medium, and a completely chaotic, clumpy flow?; (2) can absorption line variability due to cloud disruption be distinguished from that due to variability in the ionizing flux? (3) can a standard partial covering analysis of our synthetic line profiles adequately reproduce the properties (namely, the velocity-dependent optical depth and covering fraction profiles) of our solutions?

As for the first question, our expectation is that cloud acceleration can in principle leave an absorption signature as the cloud is being disrupted, provided the absorption line is broader than the thermal width of the warm gas alone. Namely, the clumps of gas with the highest opacity end up the fastest moving, so that if absorption from warm gas is overall enshrouded in a broader absorption line formed in the hot inter-cloud gas, there will be systematically more absorption on the blue side of line center. Hence, the expected signature for the acceleration of a newly formed cloud is an initially symmetric line profile that becomes asymmetric with time as a somewhat deeper absorption feature (that tracks the warm cloud material) becomes increasingly blueshifted.

To confirm this expectation and answer the other questions posed, it was necessary to perform photoionization calculations in order to calculate line opacities for the most abundant ions present at the temperature range of our simulations. These calculations are described in §7.2, along with our methods for calculating simulated absorption lines. Our results are presented in §7.3, followed by our discussion in §7.4 and conclusions in §7.5. The methods of the last two chapters will be referred to as PW15 and WP16, after their respective published versions, Proga & Waters (2015)

and Waters & Proga (2016).

7.2 Methods

Time-dependent, 2D hydrodynamical simulations of a two phase medium form the basis for our calculations of absorption line profiles from first principles, as they provide the density, velocity, and temperature fields of the gas. This information is used to determine the opacity (and hence optical depth) of a specific ion by also running a dense grid of photoionization models using XSTAR (Kallman & Bautista 2001) for an assumed set of atomic abundances and spectral energy distribution (SED). The absorption line profiles are calculated by accounting for the attenuation of a uniform background source. Below we describe these methods in detail, emphasizing the underlying physical assumptions made when applying photoionization modeling to dynamical flow solutions. Finally, we discuss our procedure for making a comparison between our synthetic line profiles and a commonly used partial covering model (e.g., Barlow & Sargent 1997; Hamann et al. 1997).

7.2.1 Hydrodynamical simulations

We focus our analysis on two different initial configurations leading to a clumpy medium: (i) a round cloud and (ii) a ‘slab’ configuration, which can be viewed as a local portion of a spherically symmetric shell of cloud material. Both configurations are arrived at by evolving a small isobaric perturbation in a homogenous, periodic box of nearly fully ionized gas that is thermally unstable.

For our purposes here we run new simulations that are basically reruns of those presented in PW15. The main differences are that we use a square domain and for case (i) we take the amplitudes and growth rates of the initial perturbations to be identical in both the x and y directions to promote the formation of a round cloud.

For each configuration, we also carry out an additional simulation that uses a time-varying ionizing flux, $F_{\text{ion}}(t)$, in order to study the effects of variability. This time dependence carries over to the photoionization parameter, $\xi = 4\pi F_{\text{ion}}/n$, where n is the gas number density. As in WP16, we model the variability using a simple sinusoidal flux,

$$F_{\text{ion}}(t) = F_X(1 + A_X \sin(2\pi t/t_X)), \quad (7.1)$$

where A_X and t_X are the amplitude and period of flux oscillations about a mean flux $F_X =$

$n_{eq}\xi_{eq}/4\pi \approx 7.82 \times 10^8 \text{ erg s}^{-1} \text{ cm}^{-2}$. The subscript ‘eq’ denotes values used to define the initial equilibrium state of the gas. As described by PW15, $\xi_{eq} = 190$ is chosen based on numerical requirements to adequately resolve the interfaces between warm and hot gas. The relation $n_{eq}T_{eq} = 10^{13} \text{ cm}^{-3} \text{ K}$ typical of AGN (e.g., Krolik 1999) sets n_{eq} because $T_{eq} = 1.93 \times 10^5 \text{ K}$ is fixed by the radiative equilibrium curve once ξ is chosen (see PW15). We again adopt $A_X = 0.2$ and $t_X = 5t_{th} \approx 3.5 \text{ days}$, where t_{th} is the thermal time, defined as the ratio of the internal energy density of the gas to the net volumetric heating rate on the radiative equilibrium curve at (ξ_{eq}, T_{eq}) .

These simulations explored a parameter regime chosen such that the majority of lines contributing to the line driving are optically thin. The gas is therefore too highly ionized to host an abundance of ions responsible for forming broad absorption lines (BALs) commonly observed in the UV (e.g., Si IV, C IV, O VI). The strongest line, as determined by our photoionization calculations described below, is the X-ray resonance line O VIII Ly α , which is a doublet with transitions at 18.9671 and 18.9725. Our results are therefore confined to calculations for this line, commonly observed in warm absorbers (e.g., Turner & Miller 2009).

Warm absorbers are observed to have outflow velocities exceeding 100 km s^{-1} (e.g., Crenshaw et al. 2003). Our cloud simulations are local, meaning they are performed in the comoving frame of the cloud and therefore apply to warm absorbers formed at any velocity, so long as it is not relativistically large. We calculate line profiles as seen by a distant observer, and at time zero before the cloud is formed, we center the line profiles at zero velocity without loss of generality.

7.2.2 Photoionization calculations

Determining the detailed photoionization structure of our clumpy medium requires solving for, at every location in our domain, the fractional ion abundances and steady state level populations for a given set of elemental abundances. For this, we employ version 2.35 of the public code XSTAR (Kallman & Bautista 2001). XSTAR was run in constant density mode with $n_{xstar} = 10^{10} \text{ cm}^{-3}$. To be consistent with the heating and cooling rates adopted in our cloud simulations, we used a 10 keV Bremsstrahlung SED. We assigned solar elemental abundances from Grevesse, Noels & Sauval (1996).

XSTAR calculates photoionization equilibrium, accounting for over 200,000 lines (Bautista & Kallman 2001), for gas with a given photoionization parameter and temperature. In our simulation domain, every grid cell is characterized by the two parameters (ξ, T) local to this cell. We therefore

ran a grid of models in (ξ, T) -space covering the full parameter space of our solutions. This grid spanned 200 points logarithmically spaced over the range $\log \xi = 0$ to $\log \xi = 8$, and 94 points logarithmically spaced from $T = 5 \times 10^3$ K to 10^8 K. Since ATHENA has already determined the temperature of the gas, XSTAR is run with the option set to keep the input temperature fixed. XSTAR provides, in addition to the ionization structure, quantities such as the opacity, emissivity, excitation and deexcitation rates, and heating/cooling rates due to individual processes.

The relevant value we extract from XSTAR is the comoving frame line center opacity of a resonance line (uncorrected for stimulated emission),

$$\begin{aligned} \kappa_{\nu_0} &= \frac{\pi e^2}{m_e c} \frac{n_1}{\rho} f_{12} \phi(\nu_0) \\ &= \frac{1}{\sqrt{\pi}} \left(\frac{\pi e^2}{m_e c} \frac{A n_{\text{xstar}}}{\nu_0 (v_{th}/c)} f_{12} \eta_{ion} \right) \cdot \frac{1}{\mu m_p n_{\text{xstar}}}. \end{aligned} \quad (7.2)$$

Here, $\rho = \mu m_p n$ is the hydrodynamic density (we set $\mu = 1$ in this work), f_{12} is the oscillator strength of the lower level of the line, n_1 is the level population of the ion's ground state, and $\phi(\nu)$ is the line profile that will be calculated separately (see §7.2.3). The level population is related to the number density from our hydrodynamical solutions through $n_1 = A \eta_{ion} n$, where A is the elemental abundance relative to hydrogen and η_{ion} is the fractional ion abundance. In the second line, $v_{th} = \sqrt{2kT/m_i}$ is the mean thermal velocity of an ion with atomic weight m_i . The term in parenthesis is the attenuation coefficient we extract from XSTAR. In the remaining term, we correct for the constant density assigned to XSTAR, n_{xstar} . By applying the density correction in this way, we assume that the opacity is rather insensitive to n , depending instead on the ratio of the density of photons to the gas number density, i.e. the photoionization parameter. Given ξ and T , we determine the line center opacity from XSTAR output using a lookup table that bilinearly interpolates between the values in our grid.

Most photoionization modeling efforts explicitly assume a static slab configuration, as hydrodynamical effects such as compressional heating and conductive heat fluxes that characterise a dynamical flow are not accounted for by XSTAR. However, it is valid to account for the latter effects independently of XSTAR using time-dependent hydrodynamical simulations provided that photoionization equilibrium is maintained as the flow evolves. That is, our approach is justified when the relevant hydrodynamical time-scales are long compared to timescales governing all of the atomic processes.

The shortest timescale on which clouds can undergo structural changes is the sound crossing

Table 7.1: Characteristic recombination rates and comparison with dynamical timescales for three representative XSTAR models.

Gas regime (T [K], ξ [ergs cm s^{-1}])	Atom/ Ion	$n_e\alpha$ [s^{-1}]	$t_{\text{dyn}}/t_{\text{rec}}$
Warm (7.53×10^4 , 77.0)	H I	1.04×10^{-3}	1.1×10^2
	O VIII	1.21×10^{-1}	1.2×10^4
Evaporating (1.93×10^5 , 190.0)	H I	4.45×10^{-4}	5.0
	O VIII	7.64×10^{-2}	8.6×10^2
Hot (4.77×10^5 , 475.0)	H I	1.87×10^{-4}	8.6
	O VIII	4.56×10^{-2}	2.1×10^3

time across a layer of cloud material. The thinnest cloud layers in our simulations belong to clouds about to undergo evaporation, which occurs on a longer timescale; the length scale for evaporation therefore determines the smallest cloud sound crossing time. This length scale is the Field length, $\lambda_F = 2\pi\sqrt{\kappa T/\rho\Gamma}$ (Begelman & McKee 1990), giving $t_{\text{dyn}} = \lambda_F/c_s = 2\pi\sqrt{\kappa/(\gamma n k \Gamma)} \approx 10^4 n_8^{-1/2}$ s, where n_8 is the number density in units of 10^8 cm^{-3} and we have plugged in fiducial values for the thermal conductivity κ and the volumetric heating rate Γ on our radiative equilibrium curve at $\xi = 190$ (see PW15). Note that this time-scale is still sensitive to temperature since both κ and Γ have implicit temperature dependence. We must compare t_{dyn} with the recombination time-scale, as it is the microphysical process that typically has the longest time-scale (e.g., Ferland 1979).

Recombination rates per ion, $n_e\alpha$ (where n_e is the free electron number density), as well as the ratios $t_{\text{dyn}}/t_{\text{rec}}$ for both hydrogen and O VIII are tabulated for three different temperatures and corresponding photoionization parameters in Table 1. The middle row was calculated for (T_{eq}, ξ_{eq}) , the equilibrium values used to set the initial conditions of the simulations, and these values are characteristic of those for the evaporating gas. The top and bottom rows quote values for T and ξ typical of the warm and hot gas in the domain at any given time as the gas evolves. For this gas, the dynamical time is defined as simply the domain sound crossing time, L_x/c_s (at the appropriate sound speed). We see that the necessary condition $t_{\text{dyn}} > t_{\text{rec}} \equiv (n_e\alpha)^{-1}$ is always satisfied by at least a factor of 5 for hydrogen. Thus, the validity of applying photoionization calculations to calculate the ionization structure of our dynamical flow solutions has been established, even for the most transient, evaporating gas in our simulations.

7.2.3 Absorption line profiles

A formal solution of the radiative transfer equation that holds when the source function for local emission is zero reads

$$L_\nu = \int_0^{L_y} \int_0^{L_x} \mathcal{I}_\nu(x, y) e^{-\tau_\nu(x, y)} dx dy, \quad (7.3)$$

where $\mathcal{I}_\nu(x, y)$ is the monochromatic specific intensity of the background source. This integral is taken over an imaginary plane of the sky (located beyond the absorber) of linear dimensions (L_x, L_y) as viewed by a distant observer, while evaluating the optical depth $\tau_\nu(x, y) = \int \kappa_\nu \rho dz$ requires an integration of the opacity $\kappa_\nu(x, y, z)$ over the line of sight (LOS) coordinate z . Note that by neglecting the source function, we do not account for scattering and remission of the line photons. Therefore, we do not include certain effects such as the net expansion of the medium, which can allow photons to be first absorbed in the blue component, and then reemitted and absorbed by the red component in a different region of the flow (e.g., Castor and Lamers 1979).

The calculation of absorption lines simplifies when there is symmetry along the y -direction of the observer plane, the case for 2D simulations. Integrating over y and measuring x in units of $L_x = 3.1 \times 10^{11}$ cm so that x varies from 0 to 1 gives

$$L_\nu = L_x L_y \int_0^1 \mathcal{I}_\nu(x) e^{-\tau_\nu(x)} dx, \quad (7.4)$$

where now the x -coordinate defines a single LOS in our calculations. We assume that the background intensity is constant. Thus, by defining the normalized absorption line profile $I \equiv L_\nu / (L_x L_y \mathcal{I}_\nu)$, we arrive at

$$I(\nu) = \int_0^1 e^{-\tau_\nu(x)} dx. \quad (7.5)$$

Evaluating the optical depth requires calculating the opacity $\kappa_\nu(x, z) = \kappa_{\nu_0}(x, z) \phi(\nu) / \phi(\nu_0)$ at every location in the domain. As described in §7.2.2, we directly determine κ_{ν_0} from XSTAR. The line profile function $\phi(\nu)$ is evaluated separately using our hydrodynamical variables. Every finite volume cell in our grid-based solution is treated as a parcel of gas that is thermally broadened according to its cell-centered temperature (between about 2×10^5 K and 10^6 K) and Doppler shifted away from line center according to its LOS velocity. Each local line profile is then specified as a Gaussian,

$$\phi(\nu) = \frac{1}{\sqrt{\pi}} \frac{1}{\Delta\nu_0} \exp\left(-\frac{(\nu - \nu_D)^2}{\Delta\nu_0^2}\right), \quad (7.6)$$

where $\Delta\nu_0 = \nu_0 v_{th}/c$ is the thermal linewidth and $\nu_D = \nu_0(1+v_z/c)$ is the Doppler shifted frequency at line center. We note that the width of the resulting net line profile is primarily set by the thermal velocity of the hot gas, $v_{th,hot} \approx 20 - 25 \text{ km s}^{-1}$, but it can also be increased by the z -component of the local velocity field.

We use the trapezoidal rule to evaluate both the optical depth integral and the integral in equation (7.5) numerically. These integrations are performed at 150 different frequencies centered around ν_D . In practice, we work in velocity space, binning the range $[v_c - 50 \text{ km s}^{-1}, v_c + 50 \text{ km s}^{-1}]$, where v_c is the ‘cloud-tracking’ velocity, or the velocity of the comoving frame that is used by ATHENA to keep the cloud centered on the domain.

7.2.4 Doublet lines and the PPC model

As mentioned, we apply the above methods to simulate absorption from O VIII Ly α , a common X-ray doublet line, whose synthetic line profiles will be denoted I_r and I_b . The subscripts ‘r’ and ‘b’ distinguish these doublet components, with I_b having a slightly higher (bluer) frequency. Many doublet lines have the property that the stronger line has an oscillator strength almost exactly twice that of the weaker line (due to relativistic effects, the fractional difference is $\sim 10^{-4}$), and so the ratio of line-center opacities is also almost 2.

Doublet lines produced in a clumpy medium are especially interesting, as revealed by the so-called pure partial covering (PPC) model (Barlow & Sargent 1997; Hamann et al. 1997; de Kool et al. 2002), a widely used model for estimating the ionic column densities of AGN outflows (e.g., Crenshaw et al. 2003). According to this model, the absorption line profiles for the two transitions are

$$\begin{aligned} I_r &= (1 - C_\nu) + C_\nu e^{-\tau_{\nu,r}}; \\ I_b &= (1 - C_\nu) + C_\nu e^{-2\tau_{\nu,r}}. \end{aligned} \tag{7.7}$$

These expressions follow from equation (7.5) when the spatial distribution of optical depth along the LOS consists of some fraction $(1 - C_\nu)$ of purely optically thin gas with $\tau_\nu = 0$, with the remaining gas optically thick with constant $\tau_\nu (= \tau_{\nu,r}$ for I_r), giving an unambiguous definition of the LOS covering fraction, C_ν . The PPC model reveals that any differences between the profiles I_b and I_r^2 are due to partial covering ($C_\nu < 1$), and therefore doublet lines encode information about the distribution and optical depth of clouds. As we will show, they can also be used to infer the

presence of cloud acceleration.

We will invoke the PPC model to help interpret our results, so for consistency we should compare the properties of our simulations to this model’s ‘doublet solution’, i.e. its predictions for C_ν and $\tau_{\nu,r}$ when applied to our synthetic doublet lines, I_r and I_b . We must therefore calculate the covering fraction C_ν and a mean value of the optical depth, $\bar{\tau}_\nu$ from our simulations. To define either quantity, we require an operational definition of obscuration, i.e. a cutoff optical depth value, τ_{cut} , above which the background source is considered ‘covered’. The fraction of sight lines with $\tau_\nu(x) > \tau_{\text{cut}}$ defines C_ν , while the average of $\tau_\nu(x)$ above this cutoff defines $\bar{\tau}_\nu$:

$$\begin{aligned} C_\nu &= \int_0^1 H[\tau_\nu(x) - \tau_{\text{cut}}] dx, \\ \bar{\tau}_\nu &= C_\nu^{-1} \int_0^1 \tau_\nu(x) H[\tau_\nu(x) - \tau_{\text{cut}}] dx. \end{aligned} \tag{7.8}$$

Here, $H(x)$ is the Heaviside step function. Note that these equations demand the profile $\tau_\nu(x)$ to be monotonically increasing. Provided the physical source is unresolved, so that an observer measures the integrated flux, $\tau_\nu(x)$ can always be sorted prior to integration.

7.3 Results

To illustrate our procedure for calculating simulated line doublets, in Figure 7.1 we display the relevant quantities that enter our calculations. The top panel shows a 2D image of the number density along with an adjacent plot displaying the optical depth profiles of the two doublet lines along the x -axis. Here, $\tau_\nu(x)$ has been calculated at line center. We will always take ‘line center’ to mean at $v = -v_c$ in velocity space, corresponding to frequencies near $\nu_D = \nu_0(1 + v_z/c)$ in frequency space. The bottom panel shows sample profiles of $\kappa_{\nu_D}(z)$ for each transition along a horizontal slice through the center of the domain. This profile, in turn, is calculated from the profiles of density and temperature, and density is shown in the middle panel. Notice that for this snapshot, the density only varies by a factor of 4 between warm and hot gas (as does temperature), while the line center opacity varies by a factor of about 60. This indicates that the ion fraction, η_{ion} , is highly sensitive to the physical conditions of the gas.

To compute the emergent flux at this line center frequency, we first attenuate a uniform background source according to these optical depth distributions. A distant observer will measure this attenuated flux integrated over x . To construct the profiles I_r and I_b , we simply perform this

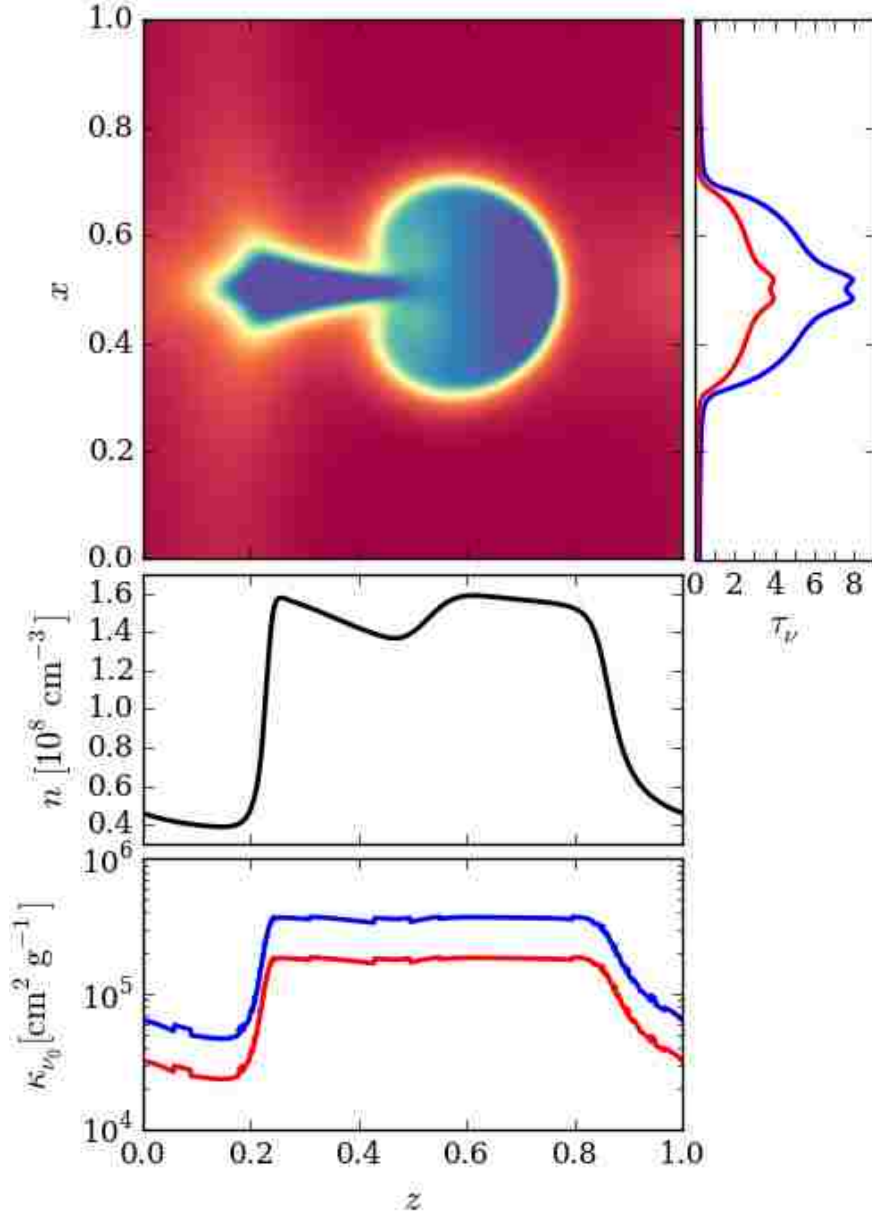


Figure 7.1: Illustrative calculation of the optical depth at line center, $\tau_{\nu_0}(x)$. The top row shows an image of the density field and the resulting spatial profile of $\tau_{\nu_0}(x)$. Both the x and z dimensions are measured in units of $L_x = 3.1 \times 10^{11}$ cm. We plot profiles of $\kappa_{\nu_0}(z)$ through the center of the domain ($x = 0.5$) for each component of the doublet in the bottom panel. This quantity has been extracted from XSTAR using a lookup table based on the values of (ξ, T) , where ξ is calculated from n , plotted in the middle panel.

integration and then repeat this procedure for all frequency bins.

Note that because our domain size, $L_x = 3.1 \times 10^{11}$ cm, is typically much less than the characteristic scale of an X-ray source ($R_X \sim 10^{13}$ cm for a Seyfert galaxy with a black hole mass $10^7 M_\odot$), we are implicitly assuming a global covering fraction of clouds similar to the local covering fraction of warm gas in our domain. That is, in order for our calculations over a single domain to carry over to the full extent of the continuum source, we must envision an ensemble of $\sim (R_X/L_x)^2 \approx 10^3$ individual adjacent domains, each containing an evolving cloud. Interpreted in terms of the cloud formation mechanism described in PW15, such a large number of clouds requires only the existence of an SED that can give rise to a thermally unstable region surrounding the continuum source. Any number of perturbations can grow simply through a large change in ionizing flux triggering cloud formation at a wavenumber, k_{\max} , corresponding to the maximum linear growth rate of the TI; $L_x = 2\pi/k_{\max}$ was assigned based on this characteristic length scale (see PW15). Due to the existence of this length scale, the distributions of resulting cloud sizes and densities are likely to be sharply peaked about some characteristic values that are only a function of the SED and photoionization parameter. We therefore would not expect the basic results presented here to change if this ‘global’ problem were to be directly modeled.

7.3.1 Synthetic absorption lines

The results of our line profile calculations are presented in Figures 2 and 3, where we show the time evolution of our two cloud configurations with and without a time-variable ionizing flux. The leftmost panels in either figure are the same, as the variable flux is not applied before this time. Each frame is separated by a half period ($t_X/2$) of the sinusoidal flux cycle, about 1.8 days (see §7.2.1). The velocity field of the gas is decomposed as $\vec{v}(x, z) = \delta v_x(x, z)\hat{x} + [v_c + \delta v_z(x, z)]\hat{z}$, where v_c is the velocity of the comoving frame that defines ‘line center’ and $(\delta v_x, \delta v_z)$ denotes the local velocity field, whose directionality is depicted by the arrows, with the light grey to black color gradient representing the transition from negative to positive δv_z . We display v_c on the upper left corner of each panel in km s^{-1} , whereas the bracketed numbers in the bottom of each panel summarise the local LOS velocities: the left (right) number is the average over all velocities with $\delta v_z < 0$ ($\delta v_z > 0$). The bottom rows of panels display the corresponding synthetic absorption lines for the O VIII doublet.

Our main result is that the absorption lines are overall smooth and nearly featureless, despite

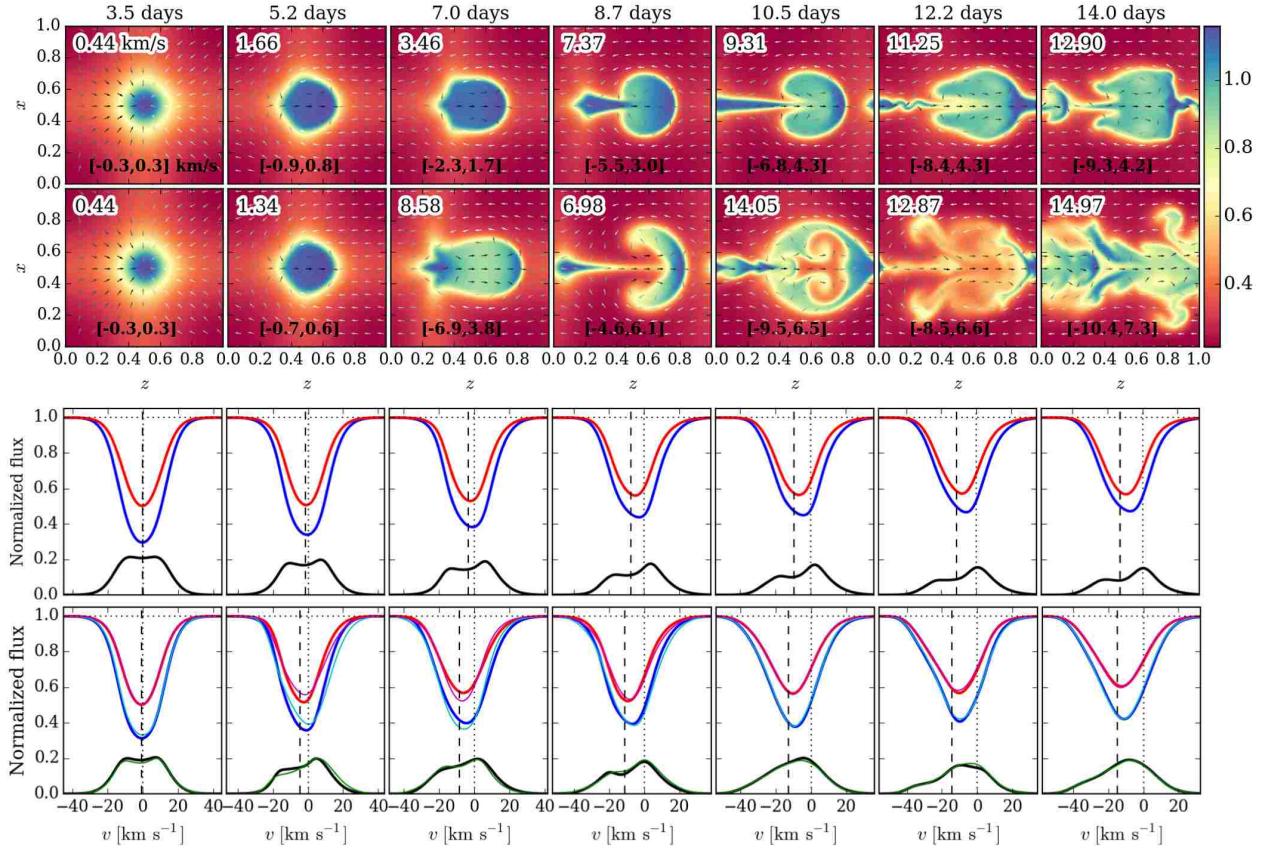


Figure 7.2: Density maps and corresponding synthetic absorption line profiles for a constant flux run (first row of panels) and a variable flux run (second row of panels). The colorbar shows number density, n , in units of 10^8 cm^{-3} . The early cloud formation stage is not shown. The source of radiation is plane parallel and emanates from the left (at $z = -\infty$), while the observer is to the right (at $z = \infty$). The numbers in the top left of every density panel are the comoving velocities of the cloud, v_c , in km s^{-1} and correspond to the vertical dashed lines in the bottom rows. Arrows on the density maps depict the local velocity field, with the gradient in colors from light grey to black representing the transition from negative to positive local LOS velocities, δv_z . The numbers in the brackets denote averages over all $\delta v_z < 0$ and $\delta v_z > 0$. Blue and red lines denote I_b and I_r , the stronger and weaker lines of the O VIII doublet, while the black lines show the difference $I_r - I_b$. To assess the line variability for the variable flux run, we overplot I_b , I_r , and $I_r - I_b$ using cyan, magenta, and green lines, respectively, for line profiles calculated at the later time $t + t_X/4$, which is either a high or low flux state; the density maps are always shown for a mean flux state. A partial covering analysis reveals that $I_r - I_b \approx C_\nu e^{-\tau_\nu}$, so dips in this profile can be caused by gas with higher optical depth, leading to the appearance of humps. The location of the dip tracks the faster moving, more opaque cloud material.

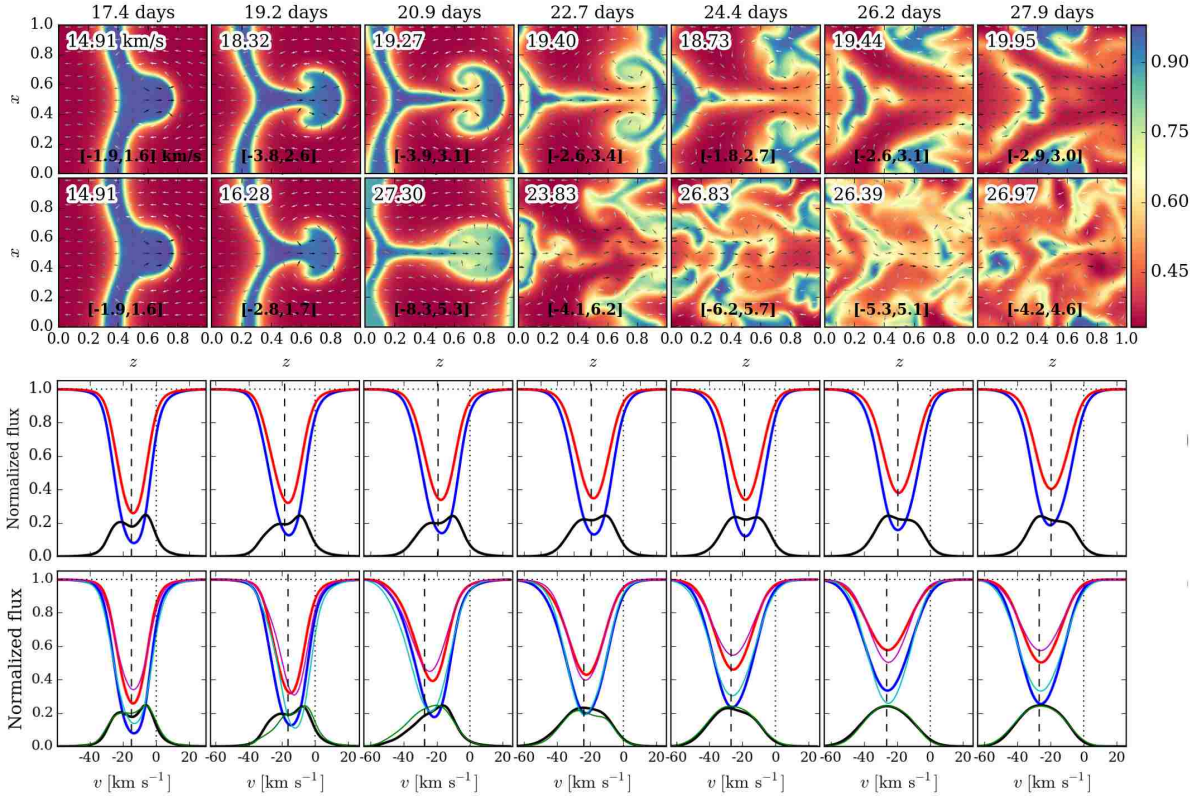


Figure 7.3: Same as Figure 7.2 but for the slab geometry. Compared to the round cloud case, there is less rapid acceleration and therefore the deeper absorption expected on the blue side side of line center is not actually visible on the line profiles. However, the diagnostic $I_r - I_b$ still reveals the presence of large differences in the local velocity field. Notice that in the bottom panels this signature of cloud acceleration gets wiped out as the cloud is disrupted since the velocities of the clumps become randomized.

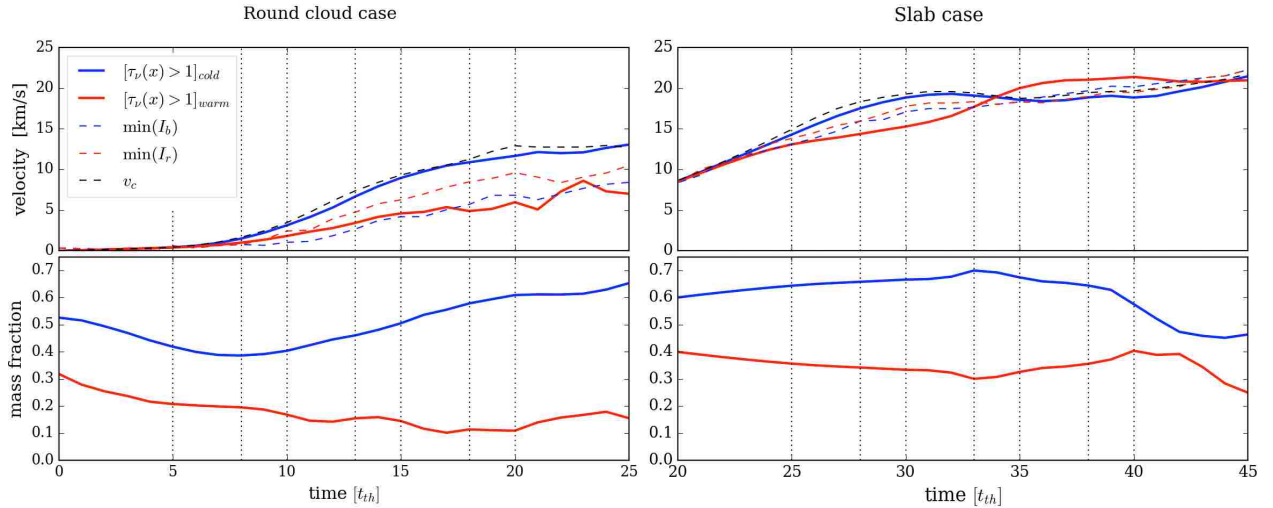


Figure 7.4: Temporal analysis linking cloud acceleration with the expected absorption properties. The dotted vertical lines mark times corresponding to the snapshots in Figures 2 and 3. The thick solid red and blue curves denote the velocity (top panels) and mass fractions (bottom panels) averaged only along sight lines with high optical depth (i.e. only for x with $\tau_\nu(x) > 1$). The dashed red and blue lines trace the locations of line center (the minima of I_r and I_b , respectively). The dashed black line marks v_c , the average velocity all warm gas in the domain, and corresponds to the dashed vertical lines in Figures 2 and 3. Since this curve coincides with the blue one, the dips in $I_r - I_b$ indeed trace the motion of cloud. In Figure 7.3 the center of these dips move to the right of $\min I_r$, which is shown more clearly here as the blue line pass beneath the red in the right panel, indicating that the cloud is moving slower than its surroundings on average.

the dramatic changes in cloud morphology. The reason for this is that the temperature distribution of the gas is the dominant factor in determining line shapes, as cloud acceleration and disruption does not generate enough velocity dispersion to significantly impact the line shapes. As indicated on the density images, the difference between the mean positive and negative LOS velocities increases with time, reaching $10 - 15 \text{ km s}^{-1}$ in Figure 7.2 and $5 - 10 \text{ km s}^{-1}$ in Figure 7.3. These relative velocities do not exceed the thermal velocity for O VIII in the hot gas, which is about 20 km s^{-1} . Thus, Doppler shifts due to the bulk velocities have a sub-dominant effect on the line widths.

However, for the round cloud case the velocity dispersion due to cloud acceleration does exceed the thermal velocity for O VIII in the *warm* gas, which is about 10 km s^{-1} . Such systematic differences in velocity can be viewed as velocity-space inhomogeneities in optical depth and visibly manifest as an asymmetry on the line profiles, as can be seen in Figure 7.2. Beginning with the third panel, the blue line profiles develop an asymmetry, showing deeper absorption to the left of line center, which is the expected signature for cloud acceleration as explained in the introduction.

Nevertheless, this asymmetry is admittedly subtle and moreover its presence is barely apparent for the slab geometry in Figure 7.3. Comparing the velocities from one frame to the next in

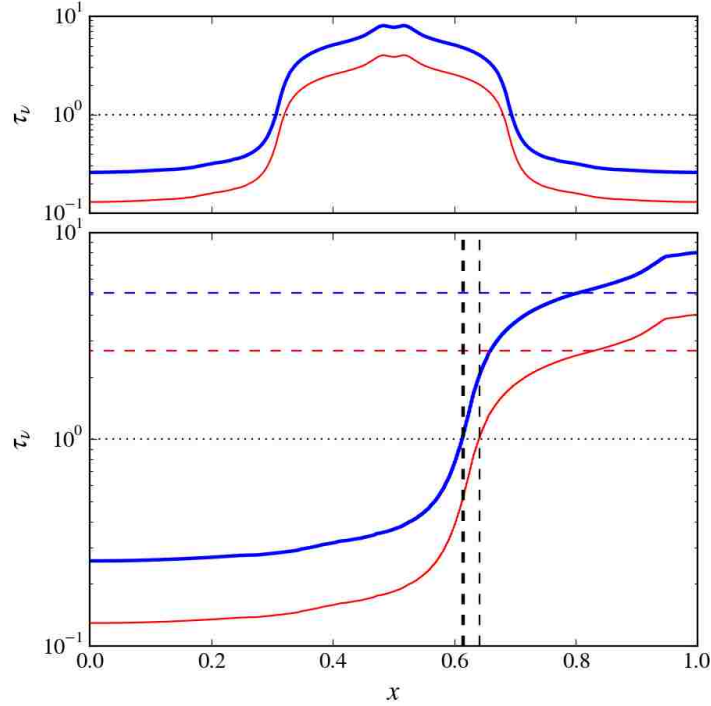


Figure 7.5: Method to calculate representative values of τ_ν and C_ν in order to assess the PPC model. The top panel reproduces the spatial optical depth profiles from Figure 7.1, but on a log-scale. In the bottom panel, we sort these profiles in order of increasing optical depth. We then apply equation (7.8), taking $\tau_{\nu,\text{cut}} = 1$, which is marked by the dotted line. The blue and red horizontal lines show $\bar{\tau}_\nu$ for each transition, which is the average of $\tau_\nu(x)$ to the right of the thick and thin black vertical dashed lines, respectively. The location of these vertical lines define $1 - C_\nu$ at line center. Repeating this procedure at all frequencies, we arrive at the ‘exact’ values plotted as a function of velocity in Figure 7.6.

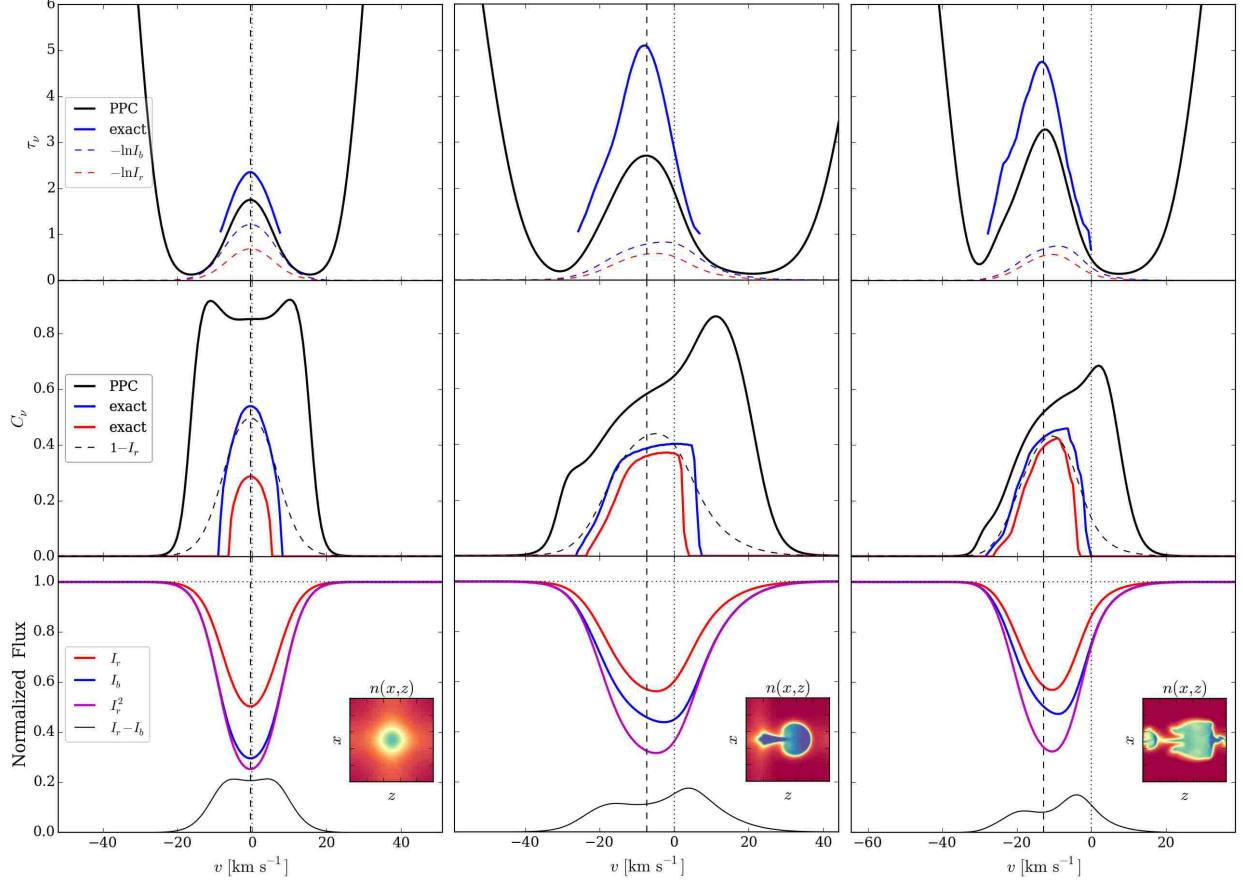


Figure 7.6: Comparison between the doublet solution of the PPC model (thick black curves) and the exact solutions for τ_ν (top panel) and C_ν (middle panel). Vertical dashed lines mark the comoving frame velocity, v_c . The unphysical behavior of $\tau_{\nu,b} = 2\tau_{\nu,r}$ in the line wings is expected (see the discussion below equation (7.10)). Notice that the PPC model’s doublet solution underestimates the true optical depth profiles measured from our simulations, while it overestimates the covering fraction profiles. In the second and third columns, C_ν is almost the same for the red and blue doublet transitions, whereas they significantly differ in the first panel where $\tau_\nu < 3$ at line center. Note that C_ν for the blue component is always close to its theoretical lower bound in the PPC model, $1 - I_r$ (dashed black curve). Along with the line profiles of each doublet component (blue and red), the bottom panel displays I_r^2 (magenta) to assess the importance of partial covering.

Figure 7.3, it is clear that the bulk flow acceleration is substantially less compared to those in Figure 7.2, explaining the lack of a noticeable acceleration signature. It is nevertheless possible to reveal its presence, as we now proceed to show.

7.3.2 A spectral diagnostic for cloud acceleration

Our analysis reveals that the difference $I_r - I_b$ leads to a profile whose shape is a sensitive diagnostic of cloud acceleration. This quantity is plotted in black in the lower panels of Figures 2 and 3. To assess the degree of variability, this quantity is also plotted in green in the bottommost row for a snapshot displaced in time a quarter cycle ($t_X/4$) ahead of that shown in the image, corresponding to a high or low flux state. Notice the overall trend among all cases: the profile for $I_r - I_b$ shows prominent asymmetric double humps when clouds are being accelerated, while the humps are small or altogether absent once the cloud is fully disrupted. Importantly, these features are nearly as prominent in Figure 7.3 as they are in Figure 7.2, despite the line profiles for the slab configuration being visibly symmetric and therefore lacking an obvious signature for cloud acceleration.

To explain these features, we have marked the values of v_c with black dashed vertical lines, showing that they intersect the dips in $I_r - I_b$. Evidently these dips track the accelerating cloud and in turn lead to the appearance of humps. Notice that these vertical lines are to the left of the locations of $\min(I_r)$ in Figure 7.2, implying that there is less residual flux at the blueshifted velocity v_c compared to the same offset to the right of $\min(I_r)$, in agreement with our expectations.

A qualitative understanding of the behavior of $I_r - I_b$ can be gained with the help of the PPC model. From equation (7.7), we have

$$\begin{aligned}
 I_r - I_b &= C_\nu e^{-\tau_{\nu,r}} (1 - e^{-\tau_{\nu,r}}), \\
 &\approx \begin{cases} C_\nu e^{-\tau_{\nu,r}} & \text{(near line center);} \\ \tau_\nu C_\nu e^{-\tau_{\nu,r}} & \text{(in the line wings).} \end{cases} \quad (7.9)
 \end{aligned}$$

We invariably find C_ν to have a flat or mildly increasing slope near line center (see §7.3.3). Hence, the only way for the profile of $I_r - I_b$ to lose monotonicity near line center is if there are velocity-space inhomogeneities in τ_ν . In other words, on the basis of the PPC model, a fast moving clump should indeed carve out a blueshifted dip in the otherwise smooth profile of $I_r - I_b$.

Note, however, that v_c does not always become increasingly blueshifted with time; in Figure 7.3, the vertical dashed lines can lie to the right of the velocity corresponding to $\min(I_r)$, indicative of

locally redshifted cloud motion. To explain this occurrence and verify quantitatively that the dips in $I_r - I_b$ are always tracking the mean cloud motion, we extract gas properties only along sight lines for which $\tau_\nu(x) > 1$ (at a velocity corresponding to $\min(I_b)$) to exclude sight lines with only hot gas. This will eliminate $\sim 1/3 - 1/2$ of all x -values in Figure 7.2 but few or no sight lines in Figure 7.3. Within this subset of our domain, we then determine the average velocity and mass fraction of the warm ($T < T_{eq}$) and hot ($T > T_{eq}$) gas.

In the top panel of Figure 7.4, we plot these quantities versus time as solid blue and red curves, along with v_c (dashed black line) and the velocities corresponding to the locations of $\min(I_r)$ and $\min(I_b)$ (dashed red and blue lines, respectively). For the round cloud case, we find a clear separation in velocities between warm and hot gas, with the average velocity of warm gas at all times exceeding those marking $\min(I_r)$ and $\min(I_b)$. It also nicely traces the curve of v_c , which is a consistency check since v_c was computed using a mass-weighted average over *all* warm gas in ATHENA. For the slab case, on the other hand, there is only a marginal separation in velocities between warm and hot gas until $t = 34t_{th}$, when the cloud material overall reverses direction. That is, it retains a net overall blueshift according to the total LOS velocity $v_z = v_c + \delta v_z$, but the local LOS velocity δv_z becomes (on average) negative. This occurrence corresponds the last 3 panels in Figure 7.3, where it is clear that the clump in the center of the domain still has $\delta v_z > 0$, but the larger clumps at the top and bottom of the domain have $\delta v_z < 0$. This sign change of the local LOS velocity is reflected in the profile of $I_r - I_b$, as the absorption dip tracing the warm gas shifts from the left side of $\min(I_r)$ to the right side.

In the lower panels of Figure 7.4, the higher mass fraction of warm gas indicates that the shape of the line profiles should primarily be controlled by the dynamics of the cloud. We can then ask why, since the warm gas is closely tracked by the speed v_c , are the line profiles not more sharply peaked around the dashed black vertical lines marking v_c ? The answer is that there is significant absorption in both the evaporating gas component (yellow colors in Figures 2 and 3) and the hot gas (red colors), so that the cloud is overall enshrouded in a background absorption profile. We will return to this point below, as it implies that the hot gas has non-negligible optical depth, which is at odds with a basic assumption of the PPC model.

7.3.3 Partial covering analysis

We have already invoked the PPC model to qualitatively explain the behavior of the profile $I_r - I_b$. Here we examine the predictions of this model more closely, by comparing our results against its ‘doublet solution’, obtained by solving equation (7.7) for $\tau_{\nu,r}$ and C_ν :

$$\begin{aligned} \tau_{\nu,r} &= -\ln I_r - \ln \left[\frac{I_r - I_b}{I_r - I_r^2} \right], \\ C_\nu &= \frac{1}{1 + (I_b - I_r^2)/(1 - I_r)^2}. \end{aligned} \quad (7.10)$$

These expressions are equivalent to those quoted in the literature (c.f. Arav, Korista, & de Kool 2002), but the first now explicitly shows the ‘correction’ to $-\ln I_r$, the prediction for $\tau_{\nu,r}$ in the case of no partial covering (when $I_b = I_r^2$). It reveals the upper bound $I_b \leq I_r$, since obviously we must have $I_r > I_r^2$. Meanwhile, the second expression immediately gives the lower bound $I_b \geq I_r^2$, because $C_\nu \leq 1$ by definition, with $C_\nu = 1$ corresponding to $I_b = I_r^2$ as required. Thus, the behavior of these expressions as a function of I_b and I_r is evident: the larger the difference between I_b and I_r^2 , the smaller the covering fraction and the larger the correction for the ‘true’ optical depth of the absorber.

However, whenever $I_b \rightarrow I_r$ the correction term to the optical depth will clearly blow up, and the profile for $\tau_{\nu,r}$ must therefore be truncated in the line wings when $I_r - I_b$ becomes very small. Only near line center is this behavior physical, for in the limiting case of doublets with matching residual intensities ($I_b = I_r$) and $\tau_{\nu,r} = \infty$, we correctly recover $C_\nu = 1 - I_r$, which is a lower bound on the profile for C_ν . In practice, application of the PPC model has typically been limited to the core of the line due to a similar anomalous effect causing unphysical values for C_ν upon attempting to deconvolve the line profiles with the instrument’s line spread function (e.g., Ganguly et al. 1999; Hall et al. 2003).

In the PPC model, the spatial optical depth profile is a step function at each frequency, which entails the following assumptions: (i.) the hot gas has zero optical depth; (ii.) the warm gas has a single optical depth value (equal to $2\tau_{\nu,r}$ in the case of the stronger line of the doublet); and (iii.) the covering fractions of either line in the doublet are the same. We assess these assumptions at line center in Figure 7.5, by taking the spatial optical depth profile from Figure 7.1 as a case in point. In the top panel of Figure 7.5, we plot $\tau_\nu(x)$ on a log-scale, showing that its minimum value is about 0.25 for the blue component, which is hardly negligible. In the bottom panel, we sort $\tau_\nu(x)$

to make it a monotonically increasing profile. We see that it indeed can be crudely approximated as a step function, with $\tau_{\nu,r}$ being represented by $\bar{\tau}_\nu$ (marked with a red dashed line), computed using equation (7.8). Additionally, the separation between the two vertical dashed lines measures the difference in covering fractions of either component (see the caption for details). Since it is relatively small, we conclude that assumption (i) will be the most severe upon comparing the PPC model’s doublet solution with our simulations. This comparison is carried out in the top two rows of Figure 7.6 for times corresponding to the first, middle, and last panels in Figure 7.2. We indeed find that the predictions of the PPC model, the black solid profiles, do not agree well with the exact values measured from our simulations. However, we confirm in Appendix C that the agreement can be improved by accounting for the fact that the hot gas has a non-negligible optical depth.

Effects of partial covering

Notice from Figure 7.6 that the peak of the optical depth profile does not coincide with $\max(C_\nu)$ or $\min(I_b)$ in the second and third panels. This is a partial covering effect: if we were to only calculate line profiles for sight lines in the middle half of the domain, this would not be the case. In other words, the line profile due to the warm gas alone is almost completely saturated, so the residual flux around v_c is coming entirely from the flux transmitted through the hot gas.

The cloud is still in the process of forming in the left panel, and therefore the warm and hot gas only differ in density and temperature by about a factor of 2. This is why I_b is approximately equal to I_r^2 in the bottom left panel, as the effects of partial covering are minimal in the absence of significant optical depth contrasts.

Another partial covering effect is the tail appearing on the blue side of the C_ν profiles in the middle and right panels. Since fast moving clumps tend to have higher C_ν , this is in agreement with expectations. We note that the PPC model’s doublet solution, despite grossly overestimating the red side of C_ν , correctly captures this overall feature on the blue side.

7.3.4 Line profile variability

The blue and red line profiles in the last row of Figures 2 and 3 correspond to times in which the sine function is zero in equation (7.1). Overplotted with these are line profiles corresponding to the nearest high or low flux state (when $\sin(2\pi t/t_X) = \pm 1$) to show the effects of variability in response to changes in the ionizing flux. As shown by WP16, there are significant variations in

temperature and density during these states, yet this evidently only amounts to a moderate level of flux variability. Comparing the strengths of the lines across each row, we see that more variability is caused by cloud disruption than by the response of the gas to the 20% changes in ΔF_X .

Indeed, comparing the cases without variability in the ionizing flux, we see that the time-dependent cloud dynamics alone causes significant absorption line variability. Furthermore, in an environment prone to TI, a large change in ΔF_X (i.e. $A_X \gtrsim 1$ in equation (7.1)) can trigger cloud formation by displacing ξ to unstable regions on the radiative equilibrium curve (PW15), and this original deepening of the line profile (not shown here) can also be a source of variability.

7.4 Discussion

We have combined 2D hydrodynamic simulations of the evolution of irradiated, thermally unstable gas in AGN with a dense grid of XSTAR models in order to calculate the detailed photoionization structure of the gas. This type of calculation represents the state of the art, as several research groups have recently developed interfaces between a hydrodynamic code and either XSTAR (Kinch et al. 2016) or CLOUDY (Salz et al. 2015; Ramírez-Velasquez et al. 2016) in order to self-consistently account for radiation source terms under the assumption that photoionization equilibrium is established on time-scales short compared to all relevant dynamical time-scales (recall §7.2.2). Of these efforts, only Kinch et al. (2016) have also performed 2D simulations. Our approach here is not fully self-consistent, even within this approximation, as the heating and cooling rates and radiation force used in our hydrodynamic simulations are based on analytic fits to earlier photoionization calculations that assumed the same SED (see PW15 for details). Here, XSTAR output is not being coupled to the hydrodynamics, as that first requires a non-trivial calculation of the force multiplier resulting from a given SED, work which is underway in our group (Dannen, Proga, & Kallman 2016, in preparation). While we have yet to explore how different SEDs can affect the acceleration and dynamics of clouds, they are unlikely to change the qualitative outcome of our local cloud simulations, which show that the flow becomes turbulent but remains clumpy.

Several global models of the broad line region (BLR) exist in which cloud formation is attributed to TI. For example, Wang et al. (2012) considered a global model for episodic BLRs in which TI is ultimately responsible for the cloud production, with the origin of the gas being attributed to a Compton heated wind arising from the irradiated ‘skin’ of a self-gravitating accretion disc. Recently, Begelman & Silk (2016) proposed the idea of magnetically elevated accretion discs and showed that

TI should operate in the uppermost layers of the disc, thereby providing a different candidate scenario for a BLR. Note, however, that TI is but one mechanism to produce a multiphase flow. Others that have been considered in the context of AGNs include clouds uplifted from the surface of an accretion disc by the ram pressure of a centrifugally driven MHD wind (e.g., Emmering et al. 1992; Kartje, Kónigl, & Elitzur 1999; Everett, Kónigl, & Kartje 2001), transient density enhancements produced by turbulence (e.g., Bottorff & Ferland 2001) in a radiatively driven wind, and a failed dusty wind (Czerny & Hryniewicz 2011; Czerny et al. 2015).

The absorption line profiles calculated herein can be expected to be representative of those produced by other multiphase flows, provided the clumpy gas is only moderately optically thick ($\tau_\nu \lesssim 5$) and subsonic with respect to its surroundings. Moreover, because these are local hydrodynamical simulations and the governing equations are Galilean invariant, our results apply equally well to clumps embedded in a highly supersonic outflow.

An important result from this work is that a complicated velocity field is not accompanied by a complicated line profile. Quite the contrary, the most chaotic flow regime produces the most symmetric line profiles: in the final two panels of the slab case with a variable flux (see Figure 7.3), the profile $I_r - I_b$ is single peaked and featureless. This is simply because the velocities of the clumps have been randomized and therefore (i.) any local acceleration signature has been lost and (ii.) the width of the absorption lines are set by thermal broadening alone because the local velocity field is subsonic. This result is consistent with several studies that have invoked ‘microturbulence’ to broaden line profiles, as the level of microturbulence required is supersonic (e.g., Horne 1995; Bottorff et al. 2000; Bottorff & Ferland 2002; Baldwin et al. 2004; Kraemer et al. 2007). Since it is unclear how supersonic motions can arise and persist (e.g., Kraemer et al. 2012), it is more likely that broad absorption lines are the result of ion opacity being spread over a wide range of bulk velocities that are naturally present in a large scale outflow.

In addition to line profiles maintaining their smooth shapes before and after the onset of cloud disruption, it is important to point out that they mostly retain their strengths also, aside from a small amount of variability (recall §7.3.4). Evidently, the existence of a morphologically intact cloud is not important; preservation of the mass fraction (or equivalently the filling factor) of warm gas is all that really matters, for then the overall ionization state will be unaffected. In part, this result is due to the fact that the hot gas in our simulations has a non-negligible optical depth, as revealed in §7.3.3, so that significant absorption still takes place in the absence of cloud material. Thus, the maintenance of line strengths may to some degree be a limitation of our simulations,

as the hot gas is only about 5 times hotter than the warm gas and is therefore still cool enough to host O VIII ions. Nevertheless, the relatively high optical depth of the inter-cloud gas in these simulations may mimic the presence of a much larger column of very optically thin gas. Moreover, it is quite possible that cloud formation sites for warm absorbers indeed have low optical depth contrasts since resonance line opacities in the X-ray are typically much smaller than those in the optical or UV (e.g., Kallman 2010).

UV lines in BAL outflows, on the other hand, are more likely to be very optically thick if the absorption sites are produced by clouds (e.g., Arav & Li 1994). More work is required to produce synthetic line profiles for the common UV doublet lines. This requires two advances: (i.) much higher resolution simulations to resolve the high temperature and density contrasts. This will permit the modeling of a clumpy medium in which the hot gas is hot enough to be very optically thin and the warm gas cool enough to host UV lines. (ii.) solving the equations of radiation hydrodynamics using the variable Eddington tensor closure (e.g., Jiang et al. 2012; Proga et al. 2014), as optically thick clouds will cast shadows and this effect must be properly taken into account.

In this work we focused on a doublet line in the soft X-ray simply because O VIII Ly α was found to be the strongest line produced at these temperatures and photoionization parameters. Note that to resolve this doublet in actual spectra, a resolution of $R = \lambda/\Delta\lambda > 3500$ is required; this is beyond the capabilities of the X-ray Integral Field Unit being designed for the Athena+ mission (which has $R \lesssim 2400$ in the soft X-ray band; Barret et al. 2016), but it may be within the reach of Arcus (Smith et al. 2016) or Athena+'s high resolution X-ray grating spectrometer mission. Without resolving the doublet components, the only detectable cloud signature would be an asymmetric line profile: prior to complete cloud disruption, cloud acceleration will produce deeper absorption on the blue side of line center, as in Figure 7.2.

We can speculate that the common UV doublet lines may present even clearer evidence for cloud acceleration using the $I_r - I_b$ diagnostic. According to the PPC model, $I_r - I_b \approx C_\nu e^{-\tau_\nu}$ near line center, and since τ_ν can be very large, the dips in this profile should be very prominent. It is unclear, however, if outflows are sufficiently clumpy in the UV, as continuous disc wind models can explain broad absorption lines (e.g., Sim et al. 2010) and there is growing observational support for the line-driven disc wind scenario (e.g., Filiz Ak et al. 2014). Interestingly, there has been a recent attempt to measure the bulk acceleration of outflows using a large sample of C IV BAL troughs drawn from various Sloan Digital Sky Survey programs (Grier et al. 2016). We note that a local cloud acceleration signature is to be distinguished from such bulk acceleration signatures that arise

on scales spanning the entire outflow. As we mention below, cloud acceleration can likely only be detected in narrow absorption lines.

7.5 Conclusions

Our simulations show that irrespective of the initial cloud geometry, cloud disruption generates vorticity and thus results in a complicated velocity field. Our main conclusion is that this process of mixing has little influence on the line profiles and ultimately makes them more symmetric. Were the warm gas to completely evaporate upon mixing, we would expect the line profile to significantly weaken, but it should still remain smooth since thermal broadening always dominates any bulk velocity broadening from a locally subsonic velocity field.

We confirmed our expectation that cloud acceleration imprints a deeper absorption signature on the blue side of line center before the cloud is completely disrupted. Our most interesting finding is that a sensitive spectral diagnostic for assessing the presence of cloud acceleration can be obtained by examining the difference ($I_r - I_b$) of the absorption line profiles of a doublet line. This quantity appears in the ‘doublet solution’ of the commonly used PPC model (see equation (7.10)), and hence it should be possible to perform this analysis for common UV doublets.

The detection of a cloud acceleration signature can probably only come from narrow lines that are not much broader than a thermal width, as the signature would not be present for BALs, which likely originate from smooth outflows. Repeated detections are needed to infer the presence of cloud acceleration, as the location of the dip in $I_r - I_b$ should become increasingly blueshifted with time. Behavior that would serve as evidence for cloud disruption is if the dip reverses its blueward trend or gradually disappears after being monitored on a regular (perhaps daily) basis. The detection of such a time-scale and the absence or presence of repeated episodes showing this effect would strongly constrain models for the AGN environment.

Finally, we showed that in our simulations, line strengths are more affected by cloud disruption than by changes in ionization in response to a (20%) variation in the ionizing flux. Absorption line variability that is correlated with fluctuations in the continuum light curve has recently been interpreted as evidence that changes in the ionizing continuum drives this variability (e.g., Filiz Ak et al. 2013; Wang et al. 2015; Goad et al. 2016), while the absence of such correlations is instead attributed to the transverse motion of clouds across the line of sight (e.g., Muzahid et al. 2016; Wildy et al. 2016). Cloud formation and subsequent disruption is also uncorrelated with ΔF_X and

can occur entirely along the line of sight without clumps leaving the field of view. Thus, it is an alternative to the two most commonly invoked explanations for absorption line variability.

Chapter 8

APPLICATION TO REVERBERATION MAPPING

8.1 Introduction

Assuming that the BLR is virialized, reverberation mapping can be used to estimate the mass of the central supermassive black hole (SMBH), M_{BH} . A measure of the time delay, $\langle\tau\rangle$, for gas to respond to changes in the continuum determines a characteristic BLR radius $R = c\langle\tau\rangle$ (where c is the speed of light), while the velocity widths of broad emission line profiles are used to assign a characteristic velocity Δv . The actual black hole mass measurement,

$$M_{BH} = f \frac{R(\Delta v)^2}{G}, \quad (8.1)$$

has a potentially major uncertainty associated with the value of f , the so-called virial coefficient that depends on the geometry and kinematics of the BLR. Furthermore, there can be significant uncertainties associated with the measurements of $\langle\tau\rangle$ and Δv (e.g., Krolik 2001), especially if $\langle\tau\rangle$ is determined by first assuming a form for the transfer function (the approach taken in the code JAVELIN, for example; Zu et al. 2011). Hence, even for this least demanding application of reverberation mapping, it is necessary to look to physical models of the BLR that obey observational constraints to better quantify the uncertainties associated with these quantities. Several models have been suggested, including randomly orbiting clouds, inflowing and outflowing gas, rotating disks with thermal or line driven winds, and more (see, for example, the review by Mathews & Capriotti (1985). and a more recent summary in Section 5 of Sulentic et al. (2000).

Although a great deal of work has been done to model the photoionization of the BLR gas, relatively few calculations aimed at deriving line profiles and transfer functions have been performed, especially ones taking into account both hydrodynamics and radiative transfer (e.g., Chiang & Murray 1996). Indeed, the majority of these modeling efforts employ stochastic methods (e.g., Pancoast et al. 2011) that, while sophisticated,¹ cannot easily incorporate the extensive modeling capability offered by performing calculations from first principles using numerical simulations. In

¹We refer specifically to discrete particle, Monte-Carlo based methods that model the BLR by prescribing probability distributions for the particles' emission properties and kinematics.

this work, we therefore adopt the complementary approach of calculating echo images, line profiles and transfer functions by post-processing grid-based hydrodynamical simulation data.

For any BLR model to permit the use of equation (1), the responding gas must be virialized. Hence, in the case of disk winds, the outflow itself must be virialized. A rigorous approach to testing this requirement was taken by Kashi et al. (2013), who analyzed various outflow solutions and found that the *line-driven wind solution* presented by PK04 is indeed virialized out to large distances, owing to the dominance of the rotational component of the wind velocity. Formally, a system is virialized if the sum of the density-weighted, volume-integrated internal energy and kinetic energy is equal to -1/2 the value of the density-weighted, volume-integrated gravitational potential energy (see eqns. 2-3 in Kashi et al. 2013). Importantly, Kashi et al. (2013) found that the outflow in the PK04 solution will be observed as virialized from any line of sight (LoS).

This chapter is structured as follows. In §8.2, we present our formalism to derive the impulse response function², the fundamental quantity in reverberation mapping. In §8.3, we discuss the methods used to evaluate it. In §8.4, we benchmark our methods by recovering the analytic solution of Chiang & Murray (1996).

8.2 Formalism

The classic work of Blandford & McKee (1982; hereafter BM82) was published a year before the appearance of a seminal paper by Rybicki & Hummer (1983; hereafter RH83), who presented the methodology that is now widely used to calculate line profiles in rapidly moving media. Therefore, we first derive the impulse response function using the framework of RH83, showing how it is consistent with the one first derived by BM82.

8.2.1 Derivation of the impulse response function

From RH83, the specific monochromatic luminosity L_ν due to line emission can be calculated by integrating the product of the monochromatic emission coefficient (or emissivity) j_ν and the directional escape probability β_ν over the volume V of the entire emitting region:

$$L_\nu(t) = \int dV j_\nu(\mathbf{r}, t) \beta_\nu(\mathbf{r}, t). \quad (8.2)$$

²What we call the impulse response function is normally termed the 2-D transfer function, an echo image is its digital representation, and we reserve *transfer function* to explicitly denote the frequency-integrated impulse response function.

Here, both j_ν and β_ν depend on the direction of emission, \hat{n} ; only one direction, that pointing toward the distant observer, contributes to $L_\nu(t)$. The product $j_\nu\beta_\nu$ can be considered an effective emissivity, the role of β_ν being to allow a unified treatment of optically thick and thin gas. In particular, as demonstrated by Chiang & Murray (1996), the escape probability formalism permits a straight forward calculation of how optically thick regions *in rapidly moving media* respond to variations in the ionizing continuum (through the effects of velocity shear). In contrast, the response from optically thick regions in static or slowly moving media is much more difficult to calculate on account of the extra time delays associated with multiple scatterings.

To proceed, a distinction must be drawn between steady and variable line profiles (e.g., Krolik et al. 1991). The variable line profile $\Delta L_\nu(t)$ can be defined as the component of the total observed line profile $L_\nu(t)$ that actually varies in response to continuum fluctuations, while the steady line profile $\langle L_\nu \rangle$ is a time-averaged background component (that may or may not correspond to the BLR gas); symbolically,

$$L_\nu(t) = \langle L_\nu \rangle + \Delta L_\nu(t). \quad (8.3)$$

The principle behind reverberation mapping is that the variable line profile, as observed at time t , is caused by small fluctuations of the continuum light curve L_X at some earlier time $t - \tau$ (typical fractional rms variability amplitudes are $\lesssim 20\%$; e.g., De Rosa et al. 2015). Reworded from the standpoint of this paper, this principle implies that given the impulse response function $\Psi(\nu, \tau)$ (i.e. a model of the BLR) and the light curve of continuum fluctuations, $\Delta L_X = L_X - L_0$ (with L_0 a reference continuum level), we can predict the shape of the variable line profile through the convolution

$$\Delta L_\nu(t) = \int_0^\infty \Psi(\nu, \tau) \Delta L_X(t - \tau) d\tau. \quad (8.4)$$

Returning to equation (8.2), consider the response of the gas to a change in ionizing continuum flux ΔF_X as seen *in the rest frame of the source*, i.e. according to an observer located at position $r = 0$ in a spherical coordinate system centered on the BLR. Then the increased continuum flux, $\Delta F_X(t' - r/c) = \Delta L_X(t' - r/c)/4\pi r^2$, received by a gas parcel at time t' and position r is perceived by the observer to have been emitted by the continuum source at the earlier time $t' - r/c$. Here we invoked several of the basic assumptions used in almost all reverberation mapping studies of the BLR: point source continuum emission, straight line propagation from source to gas parcel, and no plasma effects (ensuring the constant propagation speed c). Provided ΔF_X is small relative to

$\langle F_X \rangle$, the emissivity can be expanded as

$$j_\nu(\langle F_X \rangle + \Delta F_X(t' - r/c)) \approx \langle j_\nu \rangle + \frac{\partial j_\nu}{\partial F_X} \Delta F_X(t' - r/c). \quad (8.5)$$

By inserting this relationship into equation (8.2) and making a comparison with equation (8.3), we identify

$$\langle L_\nu \rangle = \int dV \langle j_\nu \rangle \beta_\nu, \quad (8.6)$$

and

$$\Delta L_\nu(t') = \int dV \frac{\partial j_\nu}{\partial F_X} \Delta F_X(t' - r/c) \beta_\nu. \quad (8.7)$$

The first equation just states that the steady line profile is computed as in equation (8.2), but in a time averaged sense, while the second equation reveals that $\partial j_\nu / \partial F_X$, termed the *responsivity*, is fundamental to reverberation mapping.

Since we are after the luminosity seen by a distant observer, we need to account for the additional time delay for emitted photons to travel from r to the observer plane (i.e. an imaginary plane oriented perpendicular to \hat{n} and located beyond the outer edge of the emitting volume). We must further sum over all times t' that contribute to observed emission at the distant observer's time t :

$$\Delta L_\nu(t) = \int dt' \Delta L_\nu(t') \delta \left[t - \left(t' - \frac{\mathbf{r} \cdot \hat{n}}{c} \right) \right]. \quad (8.8)$$

Here, all of the basic assumptions listed above were once again invoked, and we additionally made the (standard) assumption of negligible recombination times (because these times are typically very short). Replacing ΔF_X with $\Delta L_X / 4\pi r^2$ in equation (8.7) and then substituting equation (8.7) into equation (8.8) gives

$$\begin{aligned} \Delta L_\nu(t) &= \int dt' \int dV \frac{\partial j_\nu}{\partial F_X} \frac{\Delta L_X(t' - r/c)}{4\pi r^2} \beta_\nu \\ &\times \delta \left[t - \left(t' - \frac{\mathbf{r} \cdot \hat{n}}{c} \right) \right]. \end{aligned} \quad (8.9)$$

The impulse response function is by definition the ratio of ΔL_ν to ΔL_X for a delta-function continuum fluctuation,

$$\Psi \equiv \frac{\Delta L_\nu}{\Delta L_X} \delta(t' - r/c). \quad (8.10)$$

Making the substitution $\Delta L_X \rightarrow \Delta L_X \delta(t' - r/c)$ in equation (8.9) collapses the dt' integral, thereby

defining the total time delay

$$\tau(\mathbf{r}) = \frac{r}{c} (1 - \hat{\mathbf{r}} \cdot \hat{\mathbf{n}}), \quad (8.11)$$

so that the impulse response function can be written as

$$\Psi(\nu, t) = \int dV \frac{\partial j_\nu}{\partial F_X} \frac{\beta_\nu}{4\pi r^2} \delta[t - \tau]. \quad (8.12)$$

Equation (8.12) is seen to be consistent with BM82's equation (2.15). Specifically, the responsivity (which has units $\text{cm}^{-1} \text{s}$) is analogous to their 'reprocessing coefficient' ε , while their factor g (the projected 1D velocity distribution function) is unity in the hydrodynamic approximation. The only difference is our inclusion of the escape probability β_ν to account for the effects of anisotropy using the formalism of RH83.

8.2.2 Responsivity and opacity distributions

The derivation leading up to equation (8.12) is quite general as far as the radiative transfer is concerned. We now specialize to the Sobolev approximation by following Rybicki & Hummer (1978) and RH83, in which case

$$j_\nu(\mathbf{r}) = k S_\nu \delta \left[\nu - \nu_0 - \frac{\nu_0}{c} v_l \right], \quad (8.13)$$

where $k = (\pi e^2 / m_e c) f_{12} n_1 [\text{cm}^{-1} \text{s}^{-1}]$ is the integrated line opacity of the transition with oscillator strength f_{12} and population number density n_1 , S_ν is the source function, ν_0 is the line center frequency, and $v_l \equiv \hat{\mathbf{n}} \cdot \mathbf{v}$ is the line of sight velocity of the emitting gas which has bulk velocity \mathbf{v} . The delta-function here arises from the use of the Sobolev approximation, for when it holds, locally Gaussian line profiles will effectively behave as delta-functions (see, for example, §8.4 of Lamers & Cassinelli 1999). Note that this statement is not equivalent to our assumption that the intrinsic line profile is much narrower than a Gaussian.

The argument of the delta-function accounts for a non-relativistic Doppler shift only. There will also be a transverse redshift that can be of order $1.5(v_t/c)^2 \times 10^5 \text{ km s}^{-1}$, where v_t is the velocity component perpendicular to the LoS, as well as a gravitational redshift of order $1.5(r_s/r) \times 10^5 \text{ km s}^{-1}$, where $r_s = 2GM_{BH}/c^2$ is the Schwarzschild radius. Since the PK04 domain extends to a minimum radius $r_{\min} \approx 30 r_s$ and the highest velocities in the domain are $\sim 0.1 c$, either effect can potentially lead to shifts $\sim 1500 \text{ km s}^{-1}$ at the base of the profile. While acknowledging that these are important effects, we ignore both relativistic redshifts to first order on the grounds that

these estimates are still small compared to the widths of our calculated line profiles and will apply mainly to the innermost gas, leading to a red wing.

The source function S_ν in equation (8.13) describes all radiative processes responsible for the line emission and in general can be divided into two contributions: (i) local intrinsic emission processes, and (ii) scattered emission. We mention below how to realistically model (i), but in this work we adopt simple scaling relations to account for (i) in a way that will enable us to compare our results with those from prior works. It is known that a proper treatment of (ii) is important when calculating steady line profiles, but it is beyond the scope of this work to investigate the importance of scattering for shaping variable line profiles.

To calculate the variable line profile, we need to specify the responsivity, $\partial j_\nu / \partial F_X$. A self-consistent determination of the responsivity requires detailed photoionization modeling coupled with radiation hydrodynamical simulations. The former type of calculation has been frequently explored without regard to the latter (e.g., Krolik et al. 1991; Goad et al. 1993; Korista & Goad 2004; Goad & Korista 2014). Here we take a first step in performing the latter type of calculation. In §8.3.4 we outline a basic modeling strategy that should be suitable for constraining BLR models upon making a comparison with observations. In essence, the velocity and density fields are found by performing hydrodynamical simulations, and then separately the responsivity and opacity distributions are obtained by carrying out photoionization calculations using the hydrodynamical simulation results as input.

For this initial investigation, we opted for a simpler approach by adopting prescriptions for the responsivity and opacity distributions. To reach a common ground with past investigations, we note that it has been common to adopt a power-law dependence for the responsivity (e.g., Goad et al. 1993, 2012) similar to the one introduced by Krolik et al. (1991), who assumed the power can be radially dependent and takes the form $\eta(r) \equiv \partial \ln S_l / \partial \ln F_X$, where S_l is the local brightness of the line-emitting gas. Phrased in terms of the source function, this is equivalent to the ansatz

$$S_\nu(\mathbf{r}) = AF_X^{\eta(r)}, \quad (8.14)$$

where A is a function of position, specified below, that sets the overall response amplitude. Photoionization modeling indicates that η typically ranges between 0 and 2 (see e.g., Krolik et al. 1991; Goad et al. 1993, 2012). For simplicity, we adopt $\eta = 1$ in this work, which gives A units of seconds

and defines our responsivity as

$$\frac{\partial j_\nu(\mathbf{r})}{\partial F_X} = k A \delta \left[\nu - \nu_0 - \frac{\nu_0}{c} v_l \right]. \quad (8.15)$$

Specifying the magnitude of A is only necessary when making quantitative comparisons with observed spectra. We will use arbitrary flux units, allowing the constant A_0 in our fiducial relation,

$$A(r) = A_0 (r/r_1)^2, \quad (8.16)$$

where r_1 is one light day, to serve as a normalization factor. Our results are calculated using this heuristic prescription for $A(r)$, which we motivate below.

To obtain an expression for the responsivity that involves only hydrodynamical quantities, we estimate the number density of the lower level of the transition in question in terms of the fluid density ρ through

$$n_1(\mathbf{r}) = A_Z \xi_{\text{ion}} \frac{\rho}{\mu m_p}, \quad (8.17)$$

where ξ_{ion} is the ion fraction of the emitting ion with elemental abundance A_Z , and μ and m_p are the mean molecular weight and mass of a proton, respectively. These quantities are assumed to characterize the state of the gas *after* the change in photoionizing flux. We can now define an effective opacity per unit mass as

$$\kappa = \left(\frac{\pi e^2}{m_e c} \right) \frac{A_Z \xi_{\text{ion}} f_{12}}{\mu m_p \nu_0} \quad [\text{cm}^2 \text{g}^{-1}], \quad (8.18)$$

and in our calculations we take κ to be a spatially fixed quantity throughout the domain. Note that in writing equation (8.15) we have assumed that the flux dependence of the emissivity is dominated by that of the source function, i.e. that $k = \kappa \rho \nu_0$ is insensitive to changes in the ionizing flux. This will not be true in general since κ depends on the ion fraction, while hydrodynamic effects can lead to changes in ρ . Ignoring the latter possibility (since it implies a nonlinear response; see §8.3.4) therefore implies that k is independent of F_X when κ is treated as a constant.

As a very simple example of what the above scalings imply, consider a spherically symmetric, *constant*, high-velocity outflow illuminated by an isotropic source at its center. By mass conservation, the density scales as r^{-2} , and therefore so does k . Then $A \propto r^2$ amounts to assuming that the emissivity of the gas is directly proportional to the density, while the responsivity ($\partial j_\nu / \partial F_X \propto \kappa \rho r^2$)

is constant with radius since the emissivity and flux both falloff as r^{-2} . In contrast, taking $A = A_0$ implies $j_\nu \propto r^{-4}$ and $\partial j_\nu / \partial F_X \propto r^{-2}$; this scaling reproduces the results of Chiang & Murray (1996), as shown in §8.4.

8.2.3 The escape probability

In equation (8.12), the escape probability, assuming a single resonant surface, is given by RH83:

$$\beta_\nu(\mathbf{r}) = \frac{1 - e^{-\tau_\nu}}{\tau_\nu}. \quad (8.19)$$

Treating multiple resonant surfaces, which can arise for non-monotonic velocity fields, modifies equation (8.19) by an additional multiplicative factor of $e^{-\tau_\nu}$ for each surface, but we expect equation (8.19) to capture the dominant optical depth effects. In the Sobolev approximation, the optical depth is given by

$$\tau_\nu(\mathbf{r}) = \frac{k}{\nu_0} \frac{c}{|dv_l/dl|}, \quad (8.20)$$

where $dv_l/dl \equiv \hat{n} \cdot \nabla v_l$ is the line of sight velocity gradient, often denoted as Q :

$$\frac{dv_l}{dl} \cong Q(\mathbf{r}) = \sum_{i,j} \frac{1}{2} \left(\frac{\partial v_i}{\partial r_j} + \frac{\partial v_j}{\partial r_i} \right). \quad (8.21)$$

The components of Q in various coordinate systems can be found in Batchelor (1967). Therefore, the product $k \beta_\nu$ present in the integrand of equation (8.12) can be written

$$k(\mathbf{r}) \beta_\nu(\mathbf{r}) = \frac{\nu_0}{c} \left| \frac{dv_l}{dl} \right| (1 - e^{-\tau_\nu}). \quad (8.22)$$

Notice that this product is only dependent on the density and opacity through the optical depth. For $\tau_\nu \gg 1$, this dependence is very weak and the escape of photons is primarily governed by the local LoS velocity gradient. Once $\tau_\nu \lesssim 0.1$, on the other hand, $\beta_\nu \approx 1 - \tau_\nu/2$, and the impulse response function becomes weakly dependent on $|dv_l/dl|$, instead depending primarily on the magnitude of k (i.e. the product of the density and opacity), which must be smaller than $(\nu_0/c)|dv_l/dl|$. Thus, in general, the response will be weaker for reprocessed photons emitted in an optically thin region compared to an optically thick, rapidly moving region.

8.2.4 The resonance condition

Having derived formulae for the quantities appearing in the integrand of equation (8.12), we can express the impulse response function in spherical coordinates as

$$\begin{aligned} \Psi(y, t) = & \frac{1}{4\pi c} \int_{r_{\text{in}}}^{r_{\text{out}}} dr \int_0^\pi \sin \theta d\theta \int_0^{2\pi} d\phi A(r) \\ & \times \left| \frac{dv_l}{dl} \right| (1 - e^{-\tau\nu}) \delta [y - v'_l] \delta [t - \tau], \end{aligned} \quad (8.23)$$

where r_{in} and r_{out} are the inner and outer radii of the reverberating region and we have defined the dimensionless frequency shift $y \equiv (\nu - \nu_0)/\nu_0$ and denoted $v_l/c = v'_l$. The argument of the first delta function defines an iso-frequency surface specifying all physical locations that contribute to a given frequency shift y . Likewise, the argument of the second delta function defines an iso-delay surface, giving all points in the volume with nonzero responses at a given time t . Only the intersection of these two surfaces contribute to the integral at a given (y, t) . We will refer to locations satisfying the combined arguments as resonance points, and to the equation governing these locations as the resonance condition.

For axisymmetric models, to which we confine ourselves to in this work, the resonance condition is used to solve for the resonant azimuthal angles $\tilde{\phi}$ corresponding to each (r, θ) coordinate on the grid. It is clear that dependence on ϕ enters through \hat{n} . Two angles are required to specify \hat{n} , namely the observer's azimuthal and polar coordinates (ϕ_n, θ_n) . Without loss of generality we choose $\phi_n = 0$, while θ_n is the same as the LoS inclination angle, hereafter denoted i . Then the components of \hat{n} are $n_r = \sin \theta \cos \phi \sin i + \cos \theta \cos i$, $n_\theta = \cos \theta \cos \phi \sin i - \sin \theta \cos i$, and $n_\phi = -\sin \phi \sin i$, giving for the resonance condition the coupled algebraic equations

$$\begin{aligned} y &= n_r v'_r(r, \theta) + n_\theta v'_\theta(r, \theta) + n_\phi v'_\phi(r, \theta); \\ t &= (r/c) (1 - n_r). \end{aligned} \quad (8.24)$$

Here the primes on the velocity components indicate that they are in units of c (consistent with our convention for v'_l above). For *analytic* axisymmetric hydrodynamic solutions, equations (8.24) can be easily solved for $\phi = \tilde{\phi}$, given y , t , and i . However, there is a subtlety that arises for discretized solutions, requiring first the solution of an alternate form of the resonance condition, equation (8.25) below. We return to this point and discuss our actual procedure in §8.3.2.

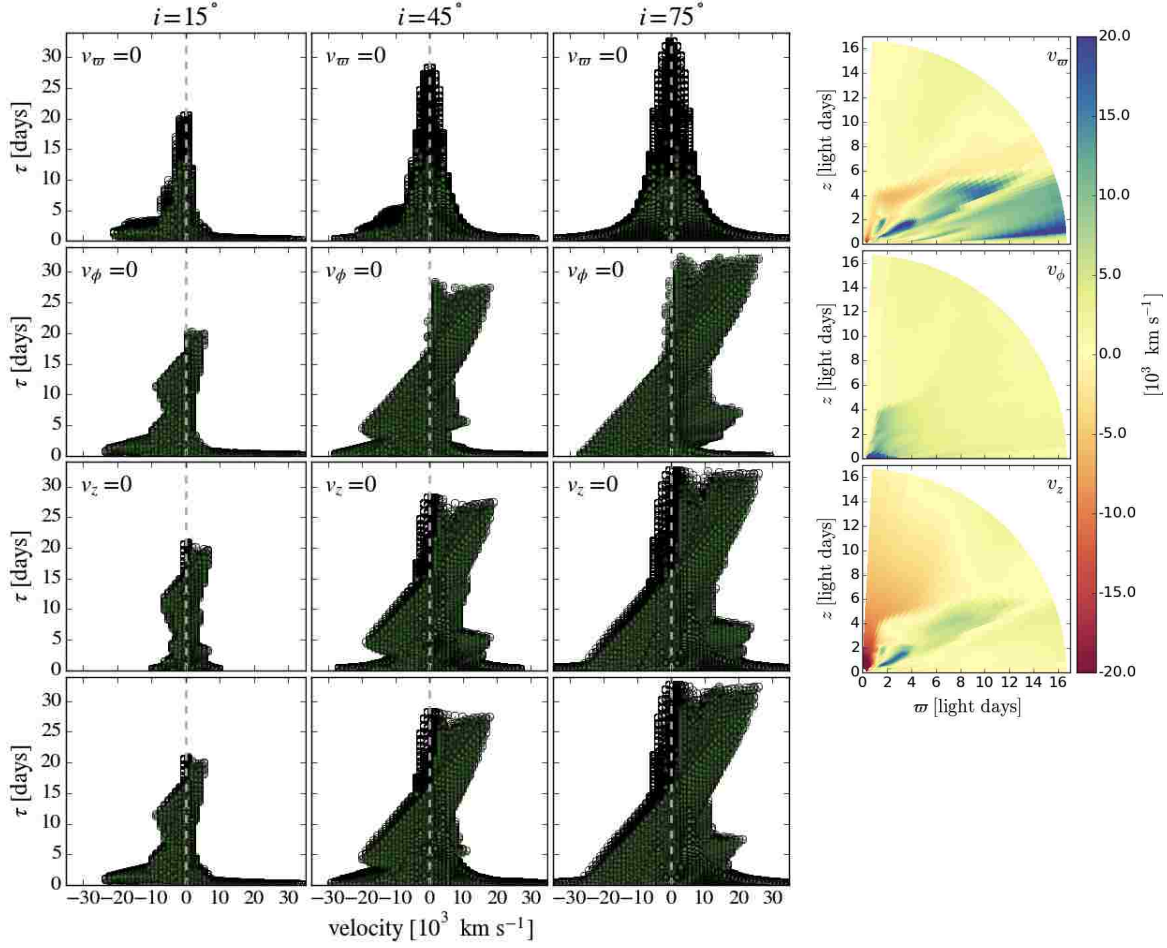


Figure 8.1: Echo image sketches of the PK04 solution. The 1st column is for $i = 15^\circ$, the 2nd for $i = 45^\circ$, and the 3rd for $i = 75^\circ$. These are plots of the two time delays, t_+ and t_- (green and black symbols, respectively, but note $t_+ = t_-$ when $v_\phi = 0$), corresponding to each LoS velocity, found by solving equation (8.25) using the velocity components from the PK04 solution. The last column displays maps of these velocity components. The first three rows of echo image sketches shows the effect of zeroing the (cylindrical) velocity component shown in the corresponding map. For example, the 1st row of sketches has nonzero v_ϕ and v_z . The sketch for $i = 75^\circ$ in this row shows a characteristic ‘virial envelope’, which is due to v_ϕ alone; at lower inclinations contributions from v_z become visible. In the 2nd row of sketches there is no virial envelope, as only the poloidal velocity components are nonzero; comparison with the 1st row reveals that the diagonal features are caused by v_ω . Vertical dashed lines are plotted at line center to highlight an overall blue-shift effect that is absent in the 3rd row, which has $v_z = 0$ and hence lacks any shift caused by $v_z \cos i$ in equation (8.26). This effect is best seen by comparing the bottom row of sketches, which accounts for the full PK04 velocity field, with the 3rd row. We emphasize that these sketches can be used to assess where an echo image *cannot* show a response, but elsewhere they need not resemble the actual image since $\Psi(y, t)$ may be negligible.

8.2.5 Echo image sketches

Welsh & Horne (1991) derived simple equations relating the velocity field and the time delay for specific outflow, inflow, and Keplerian velocity fields, which allowed them to sketch velocity vs. delay and thereby show the *possible outlines* of echo images. A general equation for ‘echo image sketches’ of axisymmetric models is found by eliminating ϕ from equations (8.24); it is simplest to write down using cylindrical velocity components, (v_ϖ, v_ϕ, v_z) :

$$t = \frac{r}{c} \left[1 - \cos \theta \cos i - \frac{\sin \theta}{v_\varpi'^2 + v_\phi'^2} \right. \\ \left. \times v_\varpi' y' \pm v_\phi' \sqrt{(v_\varpi'^2 + v_\phi'^2) \sin^2 i - y'^2} \right], \quad (8.25)$$

where

$$y' \equiv y - v_z' \cos i. \quad (8.26)$$

Equation (8.25) reduces to the simpler ones presented in Welsh & Horne (1991), i.e. the relationship for a spherical inflow/outflow is obtained by setting $\theta = -\pi/2$ and $v_\phi = v_z = 0$, giving

$$t = \frac{r}{c} \left[1 + \frac{y}{v_\varpi'} \right], \quad (8.27)$$

whereas a Keplerian disk satisfies,

$$\left[\frac{t - r/c}{r/c} \right]^2 + \left[\frac{y}{v_\phi'} \right]^2 = \sin^2 i, \quad (8.28)$$

obtained by setting $\theta = \pi/2$ and $v_\varpi = v_z = 0$.

Figure 1 shows echo image sketches for the PK04 solution. From top to bottom, the first three rows show the effect of zeroing each velocity component, maps of which are plotted in the right column. The top row lacks the prominent diagonal feature present in the other rows, indicating that it is due to the v_ϖ component. Note that diagonal features are expected for radial outflows (c.f. Welsh & Horne 1991).

The final row shows sketches with all velocity components nonzero. A comparison with the third row highlights a tendency for echo images of outflows to exhibit blue-shifted excesses. This effect is clearly revealed by equation (8.26): the velocity shift $y = (\nu - \nu_0)/\nu_0$ is offset by a factor of $(v_z/c) \cos i$, so the vertical velocity component causes a blueshift for positive v_z and a redshift for

negative v_z . This will only be significant at small inclinations ($i \lesssim 45^\circ$) due to the factor of $\cos i$. This result is examined more closely in Waters et al. (2016).

The significant differences between the bottom and top rows of sketches hints that it may be possible to infer the presence of a poloidal velocity field through observations of echo images. However, these sketches are mainly useful for visualizing the mapping from physical space to velocity-delay space, thereby showing which regions of an echo image *cannot* show a response. Most of the features outside of the ‘virial envelope’ formed by the rotational velocity component turn out to have much smaller fluxes unless the lines originating in the wind are very optically thick.

8.2.6 Transfer functions and line profiles

Most reverberation mapping studies to date have primarily focused on two quantities derived from the impulse response function. The first is the transfer function, which is the frequency-integrated impulse response function,

$$\Psi(t) = \int_{-\infty}^{\infty} \Psi(y, t) dy. \quad (8.29)$$

In practice, the transfer function is the quantity used to calculate mean time lags, and hence to measure a characteristic radius of the BLR. Similarly, we can also define the line profile by

$$\Phi(y) = \int_0^{\infty} \Psi(y, t) dt, \quad (8.30)$$

where the limits are $(0, \infty)$ since $\Psi(y, t < 0) = 0$. Note that $\Phi(y)$ is not the same as the variable line profile defined in equation (8.4). Rather, it is (to within a normalization factor) the limiting case of a variable line profile found by convolving $\Psi(y, t)$ with a *constant* continuum light curve. As such, the line profiles presented in this paper should be viewed as merely representative of the line shapes expected for our disk wind models. Detailed predictions of variable line profiles are system specific, as they require carrying out the convolution with the observed continuum light curve $\Delta L_X(t)$.

8.3 Methods

Two approaches for calculating impulse response functions from models of the BLR were introduced early on. A stochastic approach was taken by Welsh & Horne (1991) and Pérez et al. (1992), in which a domain was populated with a large number ($\sim 760,000$ and $25,000$, respectively) of points, satisfying some assigned velocity field, spatial distribution, and emissivity. These discrete particle

models continue to provide intuition into the nature of the mapping between physical space and frequency-delay space.

An analytic approach was taken by BM82 and later by Chiang & Murray (1996; hereafter CM96), whose BLR model consisted of an axisymmetric Keplerian disk combined with a simple radial wind prescription. Here we adopt CM96's approach, extending it to allow the exploration of both 2-D analytic and numerical hydrodynamical models.

8.3.1 Formal evaluation of the impulse response function

Simplifying equation (8.23) to its basic functional form and changing integration variables to $\mu \equiv \cos \theta$ gives

$$\Psi(y, t) = \int_{r_{\text{in}}}^{r_{\text{out}}} dr \int_{-1}^1 d\mu \int_0^{2\pi} d\phi I \delta [y - v'_l] \delta [t - \tau], \quad (8.31)$$

where

$$I(\mathbf{r}) = \frac{1}{4\pi c} A(r) \left| \frac{dv_l}{dl} \right| (1 - e^{-\tau_\nu}).$$

To make use of the delta functions, any pair among $(dr, d\mu)$, $(dr, d\phi)$, and $(d\mu, d\phi)$ can be replaced by $(dv'_l, d\tau)$ using a Jacobian. For axisymmetric problems in which the density and velocity fields are independent of ϕ , it is natural to replace either $(dr, d\phi)$ or $(d\mu, d\phi)$, so that the triple integral can be reduced to a single integral over μ or r . To make a clear comparison with CM96, we chose to use $(dr, d\phi)$, so the mapping reads

$$dr d\phi |J| = dv'_l d\tau, \quad (8.32)$$

where

$$|J(\mathbf{r})| = \left| \left(\frac{\partial \tau}{\partial r} \right) \left(\frac{\partial v'_l}{\partial \phi} \right) - \left(\frac{\partial \tau}{\partial \phi} \right) \left(\frac{\partial v'_l}{\partial r} \right) \right|. \quad (8.33)$$

Equation (8.31) becomes

$$\Psi(y, t) = \int_{-1}^1 d\mu \int dv'_l \int d\tau \frac{I}{|J|} \delta [y - v'_l] \delta [t - \tau], \quad (8.34)$$

which evaluates to

$$\Psi(y, t) = \int_{-1}^1 d\mu \left[\frac{I}{|J|} \right]_{(\tilde{r}, \mu, \tilde{\phi})}. \quad (8.35)$$

We use the subscript notation to indicate that for each μ , the integrand is to be evaluated at the resonance point $(\tilde{r}, \tilde{\phi})$ corresponding to a given (y, t) ; geometrically this point will lie somewhere in a conical slice (r, ϕ) through the volume. Its location is determined by the solution to the resonance condition, equation (8.24). Assuming motion purely in the midplane ($\mu = 0$), CM96's result can be obtained with the substitution $I \rightarrow I \delta[\mu - 0]$, as we illustrate in §8.4.

8.3.2 Numerical evaluation of the impulse response function

To numerically evaluate the remaining integral over μ , we employ the trapezoid rule, leading to the discrete form

$$\Psi(y, t) \approx \frac{1}{2} \sum_{k=1}^{N-1} \Delta\mu_k \left[\left. \frac{d\Psi}{d\mu} \right|_{k+1} + \left. \frac{d\Psi}{d\mu} \right|_k \right], \quad (8.36)$$

where we have used the simplifying notation

$$\left. \frac{d\Psi}{d\mu} \right|_{(\tilde{r}, \mu, \tilde{\phi})} = \left[\frac{I}{|J|} \right]_{(\tilde{r}, \mu, \tilde{\phi})}. \quad (8.37)$$

Note that for grid-based simulation data in spherical coordinates, the native grid spacing can be used to arrive directly at $\Delta\mu_k = \mu_{k+1} - \mu_k$. (Otherwise, the discretized solution would need to be interpolated to a spherical grid or a different Jacobian would need to be defined.)

As mentioned in §8.2.4, when applied to simulation data, a subtlety arises in the evaluation of the integrand, equation (8.37). To clarify what is involved, it should first be emphasized that the goal is to arrive at a legitimate digital image to compare with echo images obtained from observations. That is, we need to construct a 2-D array of pixels with the center of each pixel at specified values of (y, t) , and the magnitude of $\Psi(y, t)$ determining the value of the entire pixel. Ideally, we would like to directly evaluate each of the N values of $d\Psi/d\mu$ precisely at (y, t) . However, this cannot be done in practice. The reason is that with discretized data, it is impossible to find resonance points exactly at the center locations of pixels to an acceptable tolerance level. Indeed, as equation (8.25) reveals, there are only certain values of y that satisfy the resonance condition for a given t , and vice versa, *when the grid coordinates (r, μ) and velocity fields are given.*

Our procedure to generate an echo image therefore involves interpolating from the resonant locations nearest the center of each pixel. For every value of y , i.e. for every column of pixels in our image array, we loop through all grid points of our simulation and associate each one with a specific value of t that satisfies equation (8.25). We do the same for each row of pixels, collecting all

y values that correspond to a given t . For each pixel, we then evaluate $d\Psi(y_L, t)/d\mu$, $d\Psi(y_R, t)/d\mu$, $d\Psi(y, t_A)/d\mu$, and $d\Psi(y, t_B)/d\mu$, where (y_L, t) , (y_R, t) , (y, t_A) , and (y, t_B) are the four locations nearest to (i.e. left of, right of, above, and below, respectively) the center of the pixel. Lastly, we bilinearly interpolate the four values of $d\Psi/d\mu$ to arrive at $d\Psi(y, t)/d\mu$. By adding up all such values of $d\Psi(y, t)/d\mu$ in accordance with equation (8.36), we finally arrive at $\Psi(y, t)$, whose magnitude is assigned to that pixel.

8.3.3 Direct vs. indirect calculation of the transfer function and line profile

If provided with an analytic hydrodynamical model (e.g., that of CM96), there is no need to carry out the interpolation procedure just described, since resonance points can be found for any (y, t) . By summing over the rows and columns of resulting echo image with a suitable algorithm such as the trapezoid rule, excellent numerical approximations to the integrals in equations (8.29) and (8.30) can be obtained. We refer to this method of calculating the transfer function and line profile as an indirect one, since it first involves calculating $\Psi(y, t)$.

This summation can also be carried out for discretized solutions, using the non-interpolated values of $d\Psi/d\mu$. However, again a subtlety arises, which is not easily dealt with. The issue is the double-valued nature of the mapping from (r, μ) to (y, t) . From equation (8.25), we see that in general there can be two values of t for every y . Each will have a different resonant $\tilde{\phi}$ coordinate, as they physically correspond to emission regions on opposite sides of the BLR that have the same time delay. However, they manifest as separate branches in a plot of $\Psi(y, t)$ vs. t , and we find that one branch (corresponding to gas on the far side of the BLR) is sampled much less densely than the other (due to the logarithmic grid spacing). Hence, special integration routines are necessary to accurately carry out this indirect method, which will be needed to calculate convolutions with observed light curves; they will be presented in a separate paper focused on making a comparison with observations.

The direct method for calculating line profiles and transfer functions is to carry out the integrals over y and t in equations (8.29) and (8.30) analytically. Using the impulse response function in the

form of equation (8.34), we find, after some manipulation of the Jacobian defined in equation (8.32),

$$\begin{aligned}\Psi(t) &= \int_{r_{\text{in}}}^{r_{\text{out}}} dr \int_{-1}^1 d\mu \sum_{i=1}^2 \left[\frac{I}{|d\tau/d\phi|} \right]_{(r,\mu,\phi_{t_i})}; \\ \Phi(y) &= \int_{r_{\text{in}}}^{r_{\text{out}}} dr \int_{-1}^1 d\mu \sum_{i=1}^2 \left[\frac{I}{|dv_l/d\phi|} \right]_{(r,\mu,\phi_{y_i})}.\end{aligned}\tag{8.38}$$

The subscript notation here indicates that the integrands are to be evaluated at the location where $t = \tau(r, \mu, \phi)$ in the case of $\Psi(t)$ and $y = v_l(r, \mu, \phi)$ in the case of $\Phi(y)$; in general there can be two such locations, ϕ_{t_1} and ϕ_{t_2} for $\Psi(t)$, and ϕ_{y_1} and ϕ_{y_2} for $\Phi(y)$, hence the summations. We numerically evaluate these integrals (again using the trapezoid rule). For the technical reasons described in the previous paragraph, our results only employ this direct method. Nevertheless, we draw attention to the fact that this and the indirect method are completely independent and therefore provided a useful means to benchmark the code used in this work (see below).

8.3.4 Incorporating photoionization modeling results and accounting for time-dependent effects

The simple prescription for the responsivity used in this work is useful for surveying the properties of a particular BLR model as well as for comparing and contrasting different BLR models. Upon making a comparison with observations in order to constrain model parameters, it will be necessary to calculate the responsivity and opacity distributions by separately performing photoionization calculations using the properties of the BLR model (e.g., temperature and photoionization parameter) as input. Although it would not be fully self-consistent, provided the Sobolev approximation applies, we can then evaluate the impulse response function using equation (8.35). The function $I(r)$ appearing in the integrand becomes,

$$I(\mathbf{r}) = \frac{1}{4\pi} \frac{\partial j_\nu}{\partial F_X} \frac{1 - e^{-\tau_\nu}}{\tau_\nu},\tag{8.39}$$

with the understanding that both $\partial j_\nu / \partial F_X$ and κ are independently specified as numerical fits or tabulated functions of position.

Both the responsivity and optical depth depend on the density distribution, which may undergo changes on timescales less than the duration of the observational campaign due to the dynamics of individual clumps within the wind. In principle, there is no difficulty accounting for time-dependent dynamics by using a different output from a time-dependent simulation at every sampled delay time

τ when constructing the impulse response function $\Psi(v_l, \tau)$. Indeed, when computing variable line profiles, this procedure should be performed, as comparing results obtained this way with those calculated using a single or time-averaged output can serve as a useful measure of the uncertainty associated with theoretical line profile predictions.

Difficulties in accounting for time-dependence arise if the flux variability inferred from the observed light curve itself causes significant dynamical changes in the BLR gas, as this violates the assumption of linearity inherent in equation (8.4). In Chapter 6 we demonstrated using local simulations that the density and acceleration of optically thin gas can be appreciably affected by flux variability. If this finding proves true for global calculations as well, then equation (8.4) will formally only apply if the flux variability is implicitly accounted for in the hydrodynamical simulation. In that case, constructing a realistic BLR model will require solving the equations of radiation hydrodynamics.

8.4 Example calculation: the Chiang & Murray disk wind solution

Here we illustrate and benchmark our methods by reproducing the analytic solution presented by CM96. They considered the case of motion purely in a disk in which $v_\varpi = v_z = 0$, $\theta = \pi/2$, and $\varpi = r$. Hence, equations (8.24) read

$$y = -\frac{v_\phi}{c} \sin \phi \sin i;$$

$$t = \frac{r}{c}(1 - \cos \phi \sin i).$$

Keplerian rotation is assumed, so $v_\phi/c = \sqrt{r_s/2r}$, where $r_s = 2GM_{BH}/c^2$. Eliminating ϕ between these two equations, we find that the resonance condition is cubic in r :

$$r^3 + \left(\frac{r_s \cos^2 i}{2y^2}\right) r^2 - \frac{r_s c t}{y^2} r + \frac{r_s (c t)^2}{2y^2} = 0.$$

(For $y = 0$, this equation is only quadratic, revealing resonance points $\tilde{r}_\pm = ct/(1 \mp \sin i)$.) The corresponding values of $\tilde{\phi}$ are those that satisfy *both* the y and t equations above. Thus, for any desired frequency shift and time delay (y, t) , we can algebraically solve for all resonant locations $(\tilde{r}, \tilde{\phi})$ on the disk.

It remains to evaluate the LoS velocity gradient $|dv_l/dl|$ and the Jacobian, which by equation

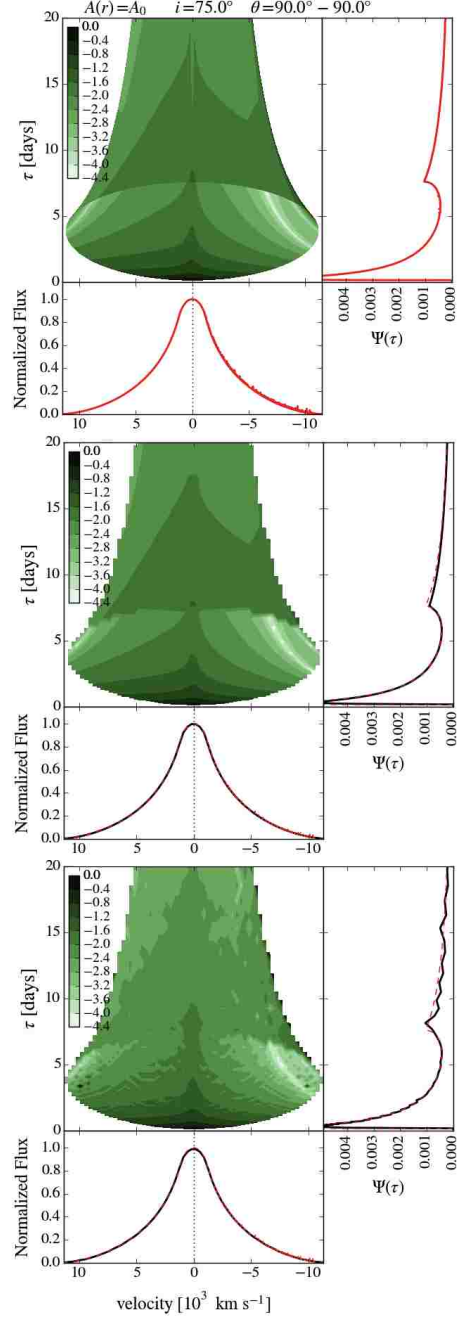


Figure 8.2: A benchmark calculation using the analytic solution from CM96. Top: $[N_\tau, N_{v_l}] = [2048, 2048]$ pixel echo image calculated using the analytic solution. The line profile (LP) and transfer function (TF) are computed by summing over the pixels in the image. Compare with figs. 2 & 4 in CM96. Center: $[N_\tau, N_{v_l}] = [128, 64]$ pixel echo image calculated using the analytic solution. The black solid LP and TF are calculated using our numerical methods on a fine, linearly-spaced radial grid with $N_r = 4,096$. Bottom: $[N_\tau, N_{v_l}] = [128, 64]$ pixel echo image calculated using our numerical methods. The black solid LP and TF are calculated using our numerical methods but using the PK04 logarithmically-spaced radial grid with $N_r = 100$. On the center and bottom plots, the LP and TF from the top plot are over-plotted as dashed red lines. The normalization factor A_0 is set by normalizing the LP in the top plot to unit maximum, and colorbars denote $\log_{10} \Psi(v_l, \tau)$. Note that CM96 use the opposite sign convention than us, so the blue side is on the right.

(8.32) also depends on derivatives of the velocity components. To explore the effects of a wind, CM96 assumed a nonzero value for the derivative dv_r/dr .³ Specifically, it appears they adopted the value $dv_r/dr = 3\sqrt{2}v_\phi/r$. The only other nonzero velocity derivative is $dv_\phi/dr = -(v_\phi/2)/r$, giving

$$\begin{aligned}\frac{dv_l}{dl} &= 3\frac{v_\phi}{r}\sin^2 i \cos\phi \left[\sqrt{2}\cos\phi + \frac{\sin\phi}{2} \right]; \\ J &= -\frac{v_\phi}{c^2}\sin i \left[\frac{(1-3\cos^2\phi)}{2}\sin i + \cos\phi \right].\end{aligned}$$

We can now evaluate the impulse response function, equation (8.37). In our formalism, CM96 consider the optically thick limit ($\tau_\nu \gg 1$) and $A(r) = A_0$. Substituting $I \rightarrow I\delta[\mu - 0]$, we have simply

$$\Psi(y, t) = \frac{I}{|J|} \Big|_{(\bar{r}, \bar{\phi})},$$

where

$$I(\mathbf{r}) = \frac{A_0}{4\pi c} \left| \frac{dv_l}{dl} \right|.$$

The top plot in Figure 8.2 shows that we have reproduced all of the detailed features of the echo image displayed in their Fig. 4, as well as the line profile in their Fig. 2.

We next solve this problem using our numerical methods. We discretize the analytically evaluated velocity components and their derivatives onto the same grid that was used in the PK04 simulation. In velocity-delay space, the PK04 grid spans a width of $[-36, 36] \times 10^3 \text{ km s}^{-1}$ and a height of 33 days, while the CM96 solution spans a width of $[-11.5, 11.5] \times 10^3 \text{ km s}^{-1}$ and a height of 780 days. For the PK04 solution, we found the optimal image resolution to be 128×128 pixels spaced linearly in velocity (i.e. each pixel spans $0.56 \times 10^3 \text{ km s}^{-1}$) and logarithmically in time delay. To make a fair comparison, in the center and right plots of Figure 8.2 we use the same time delay resolution (128 pixels covering 33 days), but we use just half the resolution (i.e. 64 pixels) to cover CM96's smaller velocity range. Analytically evaluating $\Psi(y, t)$ on this grid gives the result shown in the center plot of Figure 8.2, while numerically evaluating $\Psi(y, t)$ yields the bottom plot. The interpolation procedure tends to blur the image patterns somewhat, while for $\tau \gtrsim 7$ days there is also a small reduction in brightness that is likely more due to the logarithmic PK04 grid.

The transfer functions and line profiles plotted in red on the top plot serve as our reference solutions and are calculated using the indirect method (recall §8.3.3), in which we simply sum over

³Note that despite CM96's taking v_r to be 0 for all r on the midplane in their eqn. (2), meaning that dv_r/dr is also 0 there, they envisioned a vertically averaged solution. Hence, this prescription is consistent with a radial wind region residing at very small heights above the disk.

the image using equation (8.36). We employ our direct integration method to calculate the line profiles and transfer functions plotted in black on the center and bottom plots (and we overplot the reference solutions as red dashed lines). For the center plot, we use a fine linearly spaced grid to carry out the numerical integration over radius, while we use the much coarser but logarithmic PK04 grid for the bottom plot. Notice that the logarithmic spacing causes some numerical noise on the transfer function beyond the second peak.

We further benchmarked our code against a spherically symmetric wind model from Welsh & Horne (1991). This test was needed to verify our integration over μ since the CM96 solution does not test this aspect of our code. We again found an exact match at high resolutions, and the echo image, line profile, and transfer function were all sufficiently reproduced upon using the PK04 grid. We conclude from these tests that high resolution simulations will be needed when there are steep gradients in the velocity or density fields in order to obtain smooth line profiles and transfer functions.

Chapter 9

CONCLUSIONS

The goal of this thesis has been to lay the groundwork for a comprehensive theory of the formation and subsequent dynamics of AGN clouds. It is clear that by evolving TI into the nonlinear regime while taking into account the radiation forces that act on the cloud, we arrive at a substantially more complex physical picture than that associated with the well-known cloud physics summarized in Chapter 1. The long-term evolution of a two-phase medium in either the BLR or the NLR is a highly turbulent flow that is conducive to continuous cloud production. The chaotic state is a consequence of vorticity generation, as the requirements to conserve vorticity discussed in §2.1.6 are not close to being met. Once disrupted cloud fragments become small enough that their dimensions approach the length scale for conduction, i.e. the Field length λ_F , they will be subject to classical evaporation (Cowie & McKee 1977; Begelman & McKee 1990) on a thermal timescale. Evaporation can be seen taking place in Figure 6.4, yet we find that cloud production can be maintained because the turbulence supplies perturbations that continually trigger the thermal instability.

Does this picture support a physical model in line with those handed down from orientation-based AGN unification schemes? We think not. The idea of clouds somehow orbiting the central engine is contradictory to our findings, which reveal that the radiation force is significantly stronger than gravity. Rather, we interpret our local simulations as being supportive of a clumpy wind scenario. Specifically, our solutions likely capture the small-scale dynamics that may appear in global simulations with sufficient resolution to resolve cloud interfaces. Such simulations must of course include thermal conduction but are unlikely to radically differ from previous simulations of the AGN environment, which invariably feature large scale outflows upon including radiation forces (e.g., Proga & Kallman 2004). Thus, the existence of highly supersonic clouds in AGN is still uncertain, but if they do exist, they are likely embedded in a disk wind. The challenge is therefore to demonstrate that the clouds within a clumpy wind have the right properties to explain all of the observations. They must be of sufficient number, covering fraction, temperature, and optical depth to account for the line strengths, column densities, ionization levels, and relative fluxes of prominent emission and absorption features.

We can start by asking if the turbulent flow regime we find permits clouds to be accelerated

to the velocities inferred from the width of broad emission/absorption lines? This question can be readily addressed if our simulations are representative of the local dynamics in a global simulation, which may be the case for length scales over which the flux does not falloff substantially, say by more than 10%. This acceleration zone is $\Delta r \approx 0.05 r_0$, where r_0 is the distance where the cloud is formed. For a $10^8 M_\odot$ black hole and luminosity $L_X = 0.1 L_{\text{Edd}}$, we have $r_0 = \sqrt{L_X/4\pi F_X} = 44 \text{ ld}$. Assuming the cloud accelerates from rest, the velocity obtained is $v_f = \sqrt{2\langle a \rangle \Delta r} \approx 2800 \text{ km s}^{-1}$ for $\Delta r = 2.2 \text{ ld}$ and the average acceleration of run VF2D from Chapter 6, $\langle a \rangle = 6.5 \text{ cm s}^{-2}$. (We neglected gravity, as its acceleration is only -1.0 cm s^{-2} at r_0 .) This highly supersonic speed is indeed sufficient to account for the line widths and is reached in about 500 days, which may further complicate the procedure discussed in Chapter 8 to calculate RM predictions. The gas distribution used to calculate the impulse response function that underlies RM observables is assumed to be time-independent, i.e. any dynamical changes should occur on timescales much longer than the duration of observational campaigns. Even if it proves impossible to relax this assumption, a time-averaged clumpy wind solution will probably suffice for calculating RM observables.

Whether or not the turbulent mechanism for cloud regeneration we uncovered can truly lead to prolonged periods of cloud acceleration will depend on a number of factors. Recalling the results of Proga et al. (2014) summarized in Figure 1.4, very optically thick clouds are destroyed on timescales comparable to the sound crossing time within the cloud. The gas in those simulations was not thermally unstable, and therefore it is unclear if optically thick clouds can also be regenerated after being destroyed. The linear theory of TI presented in Chapter 4 only applies to optically thin cooling functions, so all we can really conclude is that optically thin clouds can be regenerated in a thermally unstable environment. Much more theoretical work is needed to understand TI in optically thick regimes.

Global simulations are needed to determine the actual densities of clouds that can be expected to form in AGN, and this will also complicate the linear theory of TI, as the clouds will necessarily form in the presence of an accretion flow or outflow (e.g., Balbus & Soker 1989; Mościbrodzka & Proga 2013). Other complicating factors that may significantly alter cloud formation and regeneration in a global setting include the presence of Coriolis forces and the role of the line-deshadowing instability (Owocki & Rybicki 1984) on the acceleration of clouds. Of course, it is crucial to understand the effects of adding magnetic fields, as they can prevent the gas from condensing in the first place (e.g., Mathews & Doane 1990), they may help accelerate clouds through confinement (e.g., Arav & Li 1994), and they can significantly effect cloud dynamics due to the effects of anisotropic conduction

(Choi & Stone 2012).

Before attacking these issues, interesting followup work can be done to address the properties of AGN clouds using only the basic framework laid out in this thesis. For example, it is important to understand the enhanced role of compression and expansion by running fully 3D simulations. Moreover, it is now possible to use an improved heating and cooling model compared to the one in Appendix A that was calculated for a 10 keV Bremsstrahlung SED. Recently, Dyda et al. (2017) developed a tabular method to incorporate heating and cooling rates (calculated using XSTAR) associated with actual Type I and Type II AGN SEDs into simulations. Additional calculations by Dannen, Proga, & Kallman (in preparation) have been performed to determine the accompanying force multipliers. These SEDs and their corresponding radiative equilibrium curves and force multipliers are shown in Figure 9.1. The bottom panels reveal that a thermally unstable parameter space (shaded regions) accompany these SEDs, and moreover that the force multiplier has a ‘bump’ at high ionization parameters, showing that there exist resonance lines from highly ionized species capable of contributing to the line force.

All of the ingredients necessary to repeat the cloud simulations developed here are therefore in place. Thus, it is possible to determine the expected range of cloud properties (e.g., sizes, optical depths, and formation timescales) associated with both Type I and Type II AGN. The actual distribution of these properties will likely not occupy the entire allowed range. For example, the turbulent regime may result in distributions of clouds sizes that are sharply peaked about the size corresponding to the maximum growth rate. In that case, it would be possible to place tight theoretical constraints on the allowed properties of AGN clouds that could then be used to test this theory of cloud formation and dynamics against observations.

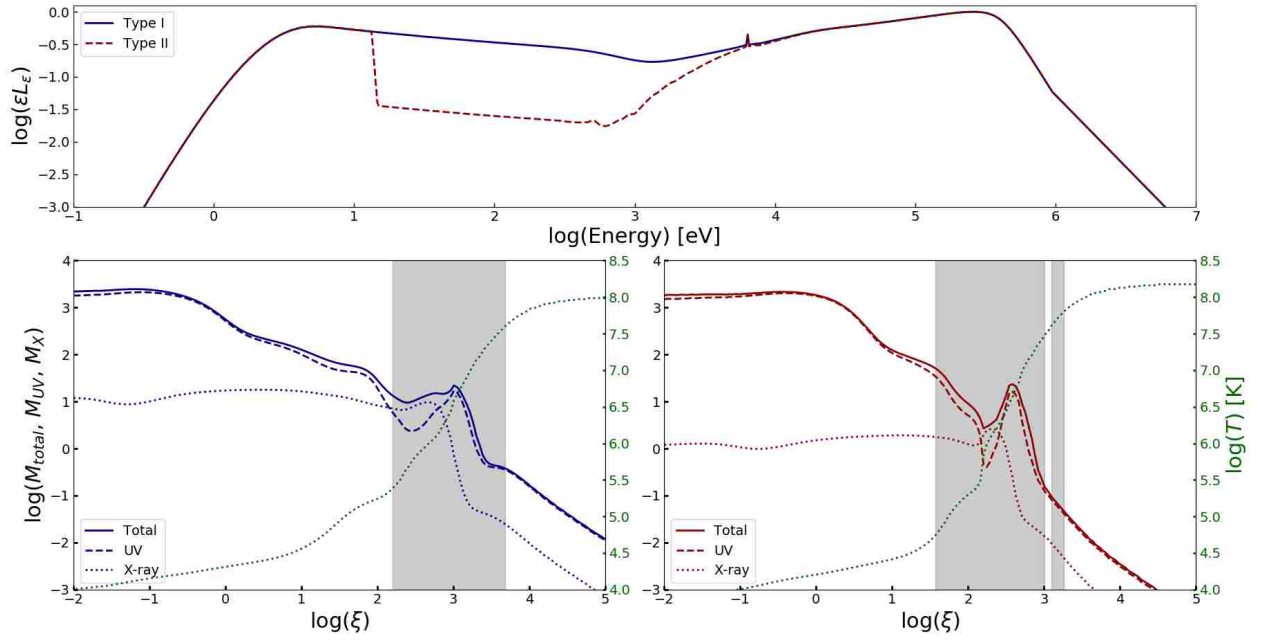


Figure 9.1: SEDs of Type I and Type II AGN, solid blue and dashed red line, respectively. These spectra are the normal and obscured SED versions of a typical Seyfert AGN (NGC 5548; see Mehdipour et al. 2015 for more details). Bottom panels: the left and right panel shows the maximum force multiplier, M_{max} , as a function of photoionization parameter, ξ , in the optically thin case (based on XSTAR calculations from Dannen, Proga & Kallman, in preparation). The left panel is for the type I SED whereas the right panel is for the type II SED. The solid lines correspond to the multiplier due to all lines, M_{total} , while the dashed and dotted lines correspond to the contributions to the multiplier due to the UV and X-ray lines, M_{UV} and M_X , respectively (see the ordinates on the left hand side). The green dashed line shows the radiative equilibrium temperature (see the ordinates on the right hand side). The shaded areas indicate regions that are unstable to isobaric perturbations. Figure courtesy of Randall Dannen.

Appendix A

EXPRESSIONS FOR HEATING AND COOLING

The net cooling function \mathcal{L} that defines the ‘S-curve’ displayed in Figure 5.1 is comprised of four heating and cooling rates. The analytic expressions for L_{ff} and G_C are

$$L_{\text{ff}} = \frac{2^5 \pi e^6}{3 h m_e c^3} \sqrt{\frac{2 \pi k_B T}{3 m_e}} Z^2 \bar{g}_B = 3.3 \times 10^{-27} \sqrt{T} \text{ [erg cm}^3 \text{s}^{-1}\text{]}, \text{ and} \quad (\text{A.1})$$

$$G_C = \frac{k_B \sigma_e}{4 \pi m_e c^2} \xi T_X \left(1 - 4 \frac{T}{T_X}\right) = 8.9 \times 10^{-36} \xi T_X \left(1 - 4 \frac{T}{T_X}\right) \text{ [erg cm}^3 \text{s}^{-1}\text{]}, \quad (\text{A.2})$$

where m_e and e are the mass and charge of an electron, h is Planck’s constant, Z is the ion atomic number, \bar{g}_B is an averaged Gaunt factor, and $T_X = 10 \text{ keV}/k_B$. The analytical fits from Blondin (1994) in our notation read

$$L_{bb} = \delta \left[1.7 \times 10^{-18} \exp\left(-\frac{1.3 \times 10^5}{T}\right) \xi^{-1} T^{-1/2} + 10^{-24} \right] \text{ [erg cm}^3 \text{s}^{-1}\text{]}, \text{ and} \quad (\text{A.3})$$

$$G_X = 1.5 \times 10^{-21} \xi^{1/4} T^{-1/2} \left(1 - \frac{T}{T_X}\right) \text{ [erg cm}^3 \text{s}^{-1}\text{]}. \quad (\text{A.4})$$

Here, δ is a parameter introduced by Blondin (1994); setting $\delta < 1$ mimics reducing the strength of line cooling when relaxing his assumption of optically thin gas. We keep $\delta = 1$ since we assume optically thin clouds. In §5.2, we refer to the heating part of G_X , which is $G_{X,h} = 1.5 \times 10^{-21} \xi^{1/4} T^{-1/2} \text{ [erg cm}^3 \text{s}^{-1}\text{]}$. Finally, it is important to note that Blondin’s photoionization calculations were revisited and independently verified using XSTAR by Dorodnitsyn et al. (2008) for an incident AGN power law spectrum. Their analytical fits differ from the above only by a minor modification to equation (A.3), which Dorodnitsyn et al. (2008) report had no significant dynamical effects on their simulation results.

Appendix B

EXPRESSIONS FOR LINE DRIVING

The simulations presented in Chapters 5-7 used the following prescription to model the line force given by (5.6). For k_{CAK} , we use equation (17) from Proga (2007):

$$\log k_{\text{CAK}} = \begin{cases} -0.383 & \text{for } \log T \leq 4 \\ -0.630 \log T + 2.138 & \text{for } 4 < \log T \leq 4.75 \\ -3.870 \log T + 17.528 & \text{for } \log T > 4.75 \end{cases} \quad (\text{B.1})$$

For η_{max} , we use equation (19) from Stevens & Kallman (1990):

$$\log \eta_{\text{max}} = \begin{cases} 6.9 \exp(0.16 \xi^{0.4}) & \text{for } \log \xi \leq 0.5 \\ 9.1 \exp(-7.96 \times 10^{-3} \xi) & \text{for } \log \xi > 0.5. \end{cases} \quad (\text{B.2})$$

Appendix C

A MODIFIED DOUBLET SOLUTION

Here we modify the PPC model discussed in Chapter 7 to account for the non-negligible optical depth in the hot gas, $\tau_{\nu,\min}$:

$$\begin{aligned} I_r &= (1 - C_\nu)e^{-\tau_{\nu,\min}} + C_\nu e^{-\tau_{\nu,r}}, \\ I_b &= (1 - C_\nu)e^{-2\tau_{\nu,\min}} + C_\nu e^{-2\tau_{\nu,r}}. \end{aligned} \tag{C.1}$$

Dropping the frequency dependence of $\tau_{\nu,\min}$ and treating it as a constant free parameter, the modified doublet solution becomes

$$\begin{aligned} \tau_{\nu,r} &= -\ln I_r - \ln \left[\frac{I_r e^{-\tau_{\min}} - I_b}{I_r e^{-\tau_{\min}} - I_r^2} \right], \\ C_\nu &= \frac{1}{1 + (I_b - I_r^2)/(e^{-\tau_{\min}} - I_r)^2}. \end{aligned} \tag{C.2}$$

The brown dashed lines in Figure C.1 show how the doublet solution changes as τ_{\min} is increased from 0.01 (thin brown line) to 0.1 (thick brown line). For $\tau_{\min} = 0.1$, the discrepancy between the doublet solution and the profiles for τ_ν and C_ν calculated from our simulations is significantly reduced. The agreement is not expected to become excellent since τ_{\min} should be frequency dependent instead of constant.

The modified solutions are truncated at frequencies on either side of line centre where $e^{-\tau_{\min}} = I_r$, since by equation (C.2), C_ν vanishes at these points. Notice that C_ν for the modified solutions with $\tau_{\min} = 0.1$ can lie beneath $1 - I_r$; this lower bound holds only for the original doublet solution. Also, the correction term for the optical depth now demands $I_b \leq I_r e^{-\tau_{\min}}$, and this should be interpreted as placing an upper bound on τ_{\min} , namely $\tau_{\min} \leq -\ln(I_b/I_r)$. Finally, by subtracting the expressions in equation (C.1), an extra term appears that will be negligible for $\tau_{\min} \lesssim 0.1$, so as to retain self-consistency in our application of the PPC model to qualitatively understand the behavior of $I_r - I_b$.

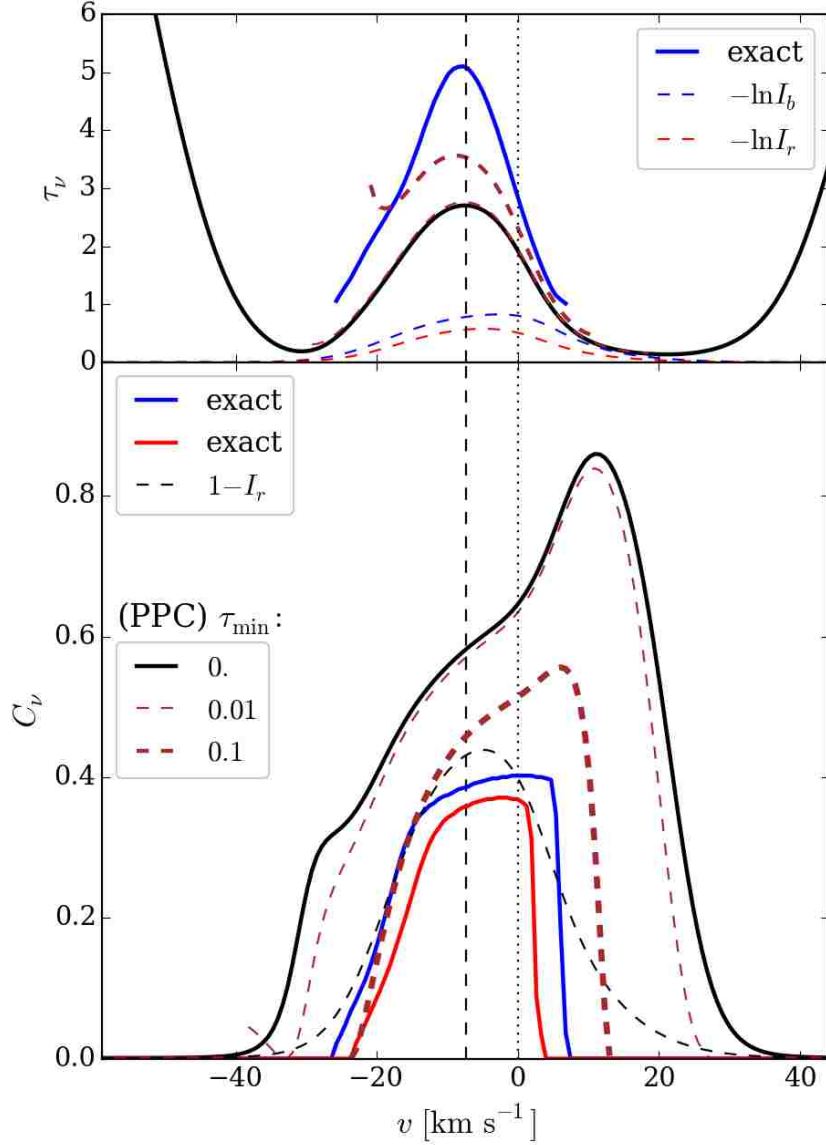


Figure C.1: Modified doublet solutions. This plot is the same as the top two middle panels of Figure 7.6, but in addition showing two modified doublet solutions (dashed brown lines) that account for a nonzero value of τ_{\min} . These modified solutions also show unphysical behavior in the line wings, but we have truncated these curves for clarity. This plot demonstrates that the discrepancy between the PPC model and the exact solutions becomes less with the modified doublet solution.

REFERENCES

- Arav, N., & Li, Z.-Y. 1994, *ApJ*, 427, 700
- Arav, N., Korista, K. T., & de Kool, M. 2002, *ApJ*, 566, 699
- Arny, T. T. 1970, *MNRAS*, 148, 63
- Antonucci, R. 1993, *ARA&A*, 31, 473
- Batchelor, G. 1967, *An Introduction to Fluid Mechanics*, Cambridge: Cambridge Univ. Press
- Bahcall, J. N., & Kozlovsky, B.-Z. 1969, *ApJ*, 155, 1077
- Balbus, S. A. 1985, *ApJ*, 291, 518
- Balbus, S. A. 1988, *ApJ*, 328, 395
- Balbus, S. A., & Soker, N. 1989, *ApJ*, 341, 611
- Balbus, S. A., & Hawley, J. F. 1991, *ApJ*, 376, 214
- Balbus, S. A. 1995, *The Physics of the Interstellar Medium and Intergalactic Medium*, 80, 328
- Balbus, S. A., & Hawley, J. F. 1998, *Reviews of Modern Physics*, 70, 1
- Balbus, S. A., & Potter, W. J. 2016, *Reports on Progress in Physics*, 79, 66901
- Baldwin, J., Ferland, G., Korista, K., & Verner, D. 1995, *ApJ*, 455, L119
- Baldwin, J. A., Ferland, G. J., Korista, K. T., Hamann, F., & LaCluyzé, A. 2004, *ApJ*, 615, 610
- Barai, P., Proga, D., & Nagamine, K. 2012, *MNRAS*, 424, 728
- Barlow, T. A., & Sargent, W. L. W. 1997, *AJ*, 113, 136
- Barret, D., Trong, T. L., den Herder, J.-W., et al. 2016, [arXiv:1608.08105](https://arxiv.org/abs/1608.08105)
- Bautista, M. A., & Kallman, T. R. 2001, *ApJS*, 134, 139
- Beckmann, V., & Shrader, C. R., *Active Galactic Nuclei*, Wiley 2012
- Begelman, M. C., & McKee, C. F. 1990, *ApJ*, 358, 375
- Begelman, M. C., & Silk, J. 2016, *MNRAS*,
- Blandford, R. D. & McKee, C. F. 1982, *ApJ*, 255, 419 (BM82)
- Blondin, J. M. 1994, *ApJ*, 435, 756
- Blumenthal, G. R., & Mathews, W. G. 1975, *ApJ*, 198, 517

Blumenthal, G. R., & Mathews, W. G. 1979, *ApJ*, 233, 479

Bottorff, M., Ferland, G., Baldwin, J., & Korista, K. 2000, *ApJ*, 542, 644

Bottorff, M. C., & Ferland, G. J. 2001, *Bulletin of the American Astronomical Society*, 33, 99.05

Bottorff, M., & Ferland, G. 2002, *ApJ*, 568, 581

Burkert, A., & Lin, D. N. C. 2000, *ApJ*, 537, 270

Castor, J. I., Abbott, D. C., & Klein, R. I. 1975, *ApJ*, 195, 157

Castor, J. I., & Lamers, H. J. G. L. M. 1979, *ApJS*, 39, 481

Castor, J. I., *Radiation Hydrodynamics*, Cambridge University Press, 2004

Chiang, J., & Murray, N. 1996, *ApJ*, 466, 704 (CM96)

Choi, E., & Stone, J. M. 2012, *ApJ*, 747, 86

Conselice, C. J., Wilkinson, A., Duncan, K., & Mortlock, A. 2016, *ApJ*, 830, 83

Cowie, L. L., & McKee, C. F. 1977, *ApJ*, 211, 135

Crenshaw, D. M., Kraemer, S. B., & George, I. M. 2003, *ARA&A*, 41, 117

Czerny, B., & Hryniewicz, K. 2011, *A&A*, 525, L8

Czerny, B., Modzelewska, J., Petrogalli, F., et al. 2015, *Advances in Space Research*, 55, 1806

Czerny, B., Li, Y.-R., Hryniewicz, K., et al. 2017, [arXiv:1706.07958](https://arxiv.org/abs/1706.07958)

de Kool, M., Korista, K. T., & Arav, N. 2002, *ApJ*, 580, 54

Davidson, K. 1972, *ApJ*, 171, 213

Davidson, K., & Netzer, H. 1979, *Reviews of Modern Physics*, 51, 715

Davis, S. W., Stone, J. M., & Jiang, Y.-F. 2012, *ApJS*, 199, 9

De Rosa, G., Peterson, B. M., Ely, J., et al. 2015, *ApJ*, 806, 128

Dyda, S., Dannen, R., Waters, T., & Proga, D. 2017, *MNRAS*, 467, 4161

Dannen, R., Proga, D., & Kallman, T. R. 2017, in preparation

Ebrero, J., Kriss, G. A., Kaastra, J. S., & Ely, J. C. 2016, *A&A*, 586, A72

Emmering, R. T., Blandford, R. D., & Shlosman, I. 1992, *ApJ*, 385, 460

Everett, J. E., Königl, A., & Kartje, J. F. 2001, *Probing the Physics of Active Galactic Nuclei*, 224, 441

Fabian, A. C., & Canizares, C. R. 1988, *Nature*, 333, 829

Fabian, A. C., Zoghbi, A., Ross, R. R., et al. 2009, *Nature*, 459, 540

Ferrarese, L., & Merritt, D. 2000, *ApJ*, 539, L9

Field, G. B. 1965, *ApJ*, 142, 531

Field, G. B., Goldsmith, D. W., & Habing, H. J. 1969, *ApJ*, 155, L149

Filiz Ak, N., Brandt, W. N., Hall, P. B., et al. 2013, *ApJ*, 777, 168

Filiz Ak, N., Brandt, W. N., Hall, P. B., et al. 2014, *ApJ*, 791, 88

Gaspari, M., Ruszkowski, M., & Oh, S. P. 2013, *MNRAS*, 432, 3401

Ganguly, R., Eracleous, M., Charlton, J. C., & Churchill, C. W. 1999, *AJ*, 117, 2594

Gayley, K. G. 1995, *ApJ*, 454, 410

Gebhardt, K., Bender, R., Bower, G., et al. 2000, *ApJ*, 539, L13

Goad, M. R., O'Brien, P. T., & Gondhalekar, P. M. 1993, *MNRAS*, 263, 149

Goad, M. R., Korista, K. T., & Ruff, A. J. 2012, *MNRAS*, 426, 3086

Goad, M. R., & Korista, K. T. 2014, *MNRAS*, 444, 43

Goad, M. R., Korista, K. T., De Rosa, G., et al. 2016, *ApJ*, 824, 11

Grevesse, N., Noels, A., & Sauval, A. J. 1996, *Cosmic Abundances*, 99, 117

Grier, C. J., Brandt, W. N., Hall, P. B., et al. 2016, *ApJ*, 824, 130

Hall, P. B., Hutsemékers, D., Anderson, S. F., et al. 2003, *ApJ*, 593, 189

Hamann, F., Barlow, T. A., Junkkarinen, V., & Burbidge, E. M. 1997, *ApJ*, 478, 80

Ho, L. C. 2008, *ARA&A*, 46, 475

Horne, K., & Marsh, T. R. 1986, *MNRAS*, 218, 761

Horne, K. 1995, *A&A*, 297, 273

Jacquet, E., & Krumholz, M. R. 2011, *ApJ*, 730, 116

Jiang, Y.-F., Stone, J. M., & Davis, S. W. 2012, *ApJS*, 199, 14

Jiang, Y.-F., Davis, S. W., & Stone, J. M. 2013, *ApJ*, 763, 102

Jiang, Y.-F., Stone, J. M., & Davis, S. W. 2012, *ApJS*, 199, 14

Kallman, T., & Mushotzky, R. 1985, *ApJ*, 292, 49

Kaastra, J. S., Detmers, R. G., Mehdipour, M., et al. 2012, *A&A*, 539, A117

Kaastra, J. S., Ebrero, J., Arav, N., et al. 2014, *A&A*, 570, A73

Kallman, T., & Bautista, M. 2001, *ApJS*, 133, 221

Kallman, T. R. 2010, *Space Sci. Rev.*, 157, 177

Kartje, J. F., Königl, A., & Elitzur, M. 1999, *ApJ*, 513, 180

Kashi, A., Proga, D., Nagamine, K., Greene, J., & Barth, A. J. 2013, *ApJ*, 778, 50

Kim, W.-T., & Narayan, R. 2003, *ApJ*, 596, 889

Kinch, B. E., Schnittman, J. D., Kallman, T. R., & Krolik, J. H. 2016, *ApJ*, 826, 52

Korista, K. T., et al. 1995, *ApJS*, 97, 285

Korista, K. T. & Goad, M. R. 2004, *ApJ*, 606, 749

Kraemer, S. B., Bottorff, M. C., & Crenshaw, D. M. 2007, *ApJ*, 668, 730

Kraemer, S. B., Crenshaw, D. M., Bottorff, M. C., Turner, T. J., & Miller, L. 2012, *AGN Winds in Charleston*, 460, 57

Krause, M., Schartmann, M., & Burkert, A. 2012, *MNRAS*, 425, 3172

Krolik, J. H. 1977, *Physics of Fluids*, 20, 364

Krolik, J. H. 1979, *ApJ*, 228, 13

Krolik, J. H., McKee, C. F., & Tarter, C. B. 1981, *ApJ*, 249, 422

Krolik, J. H. 1988, *ApJ*, 325, 148

Krolik, J. H., Horne, K., Kallman, T. R., et al. 1991, *ApJ*, 371, 541

Krolik, J. H., *Active galactic nuclei : from the central black hole to the galactic environment*, NJ: Princeton University Press 1999

Krolik, J. H. 2001, *ApJ*, 551, 72

Koyama, H., & Inutsuka, S.-i. 2004, *ApJ*, 602, L25

Kurosawa, R., & Proga, D. 2008, *ApJ*, 674, 97-110

Kurosawa, R., & Proga, D. 2009, *ApJ*, 693, 1929

Lamers, H. J. G. L. M., & Cassinelli, J. P. 1999, *Introduction to Stellar Winds*, Cambridge, UK: Cambridge University Press

- Laor, A., Fiore, F., Elvis, M., Wilkes, B. J., & McDowell, J. C. 1997, *ApJ*, 477, 93
- Lepp, S., McCray, R., Shull, J. M., Woods, D. T., & Kallman, T. 1985, *ApJ*, 288, 58
- Lynden-Bell, D., & Ostriker, J. P. 1967, *MNRAS*, 136, 293
- Magorrian, J., Tremaine, S., Richstone, D., et al. 1998, *AJ*, 115, 2285
- Mathews, W. G. 1974, *ApJ*, 189, 23
- Mathews, W. G., & Blumenthal, G. R. 1977, *ApJ*, 214, 10
- Mathews, W. G. & Capriotti, E. R. 1985, in *Astrophysics of Active Galaxies and Quasi-Stellar Objects*, ed. J. S. Miller (Mill Valley, CA: University Science Books), 185
- Mathews, W. G., & Doane, J. S. 1990, *ApJ*, 352, 423
- McCourt, M., O'Leary, R. M., Madigan, A.-M., & Quataert, E. 2014, arXiv:1409.6719
- McCourt, M., Oh, S. P., O'Leary, R. M., & Madigan, A.-M. 2016, arXiv:1610.01164
- McHardy, I. M., Arévalo, P., Uttley, P., et al. 2007, *MNRAS*, 382, 985
- McKee, C. F., & Tarter, C. B. 1975, *ApJ*, 202, 306
- Mehdipour, M., Kaastra, J. S., Kriss, G. A., et al. 2015, *A&A*, 575, A22
- Mehdipour, M., Kaastra, J. S., Kriss, G. A., et al. 2017, arXiv:1707.04671
- Meyer, C. D., Balsara, D. S., & Aslam, T. D. 2012, *MNRAS*, 422, 2102
- Mihalas, D., & Weibel Mihalas, B., New York: Oxford University Press, 1984
- Mizumoto, M., & Ebisawa, K. 2017, *MNRAS*, 466, 3259
- Mościbrodzka, M., & Proga, D. 2013, *ApJ*, 767, 156
- Mushotzky, R. F., Solomon, P. M., & Strittmatter, P. A. 1972, *ApJ*, 174, 7
- Muzahid, S., Srianand, R., Charlton, J., & Eracleous, M. 2016, *MNRAS*, 457, 2665
- Nakamura, F., McKee, C. F., Klein, R. I., & Fisher, R. T. 2006, *ApJS*, 164, 477
- Nayakshin, S., & Zubovas, K. 2012, *MNRAS*, 427, 372
- Nayakshin, S. 2014, *MNRAS*, 437, 2404
- Netzer, H. 2008, *New Astron. Rev.*, 52, 257
- Netzer, H., *The Physics and Evolution of Active Galactic Nuclei*, Cambridge, UK: Cambridge University Press 2013

Netzer, H. 2015, *ARA&A*, 53, 365

O’Sullivan, S., & Downes, T. P. 2006, *MNRAS*, 366, 1329

Osterbrock, D. E., & Mathews, W. G. 1986, *ARA&A*, 24, 171

Osterbrock, D. E., & Ferland, G. J., *Astrophysics of gaseous nebulae and active galactic nuclei*, 2nd. ed., University Science Books, CA, 2006

Owocki, S. P., & Rybicki, G. B. 1984, *ApJ*, 284, 337

Owocki, S. P., Castor, J. I., & Rybicki, G. B. 1988, *ApJ*, 335, 914

Padovani, P. 2017, *Nature Astronomy*, 1, 0194

Padovani, P., Alexander, D. M., Assef, R. J., et al. 2017, [arXiv:1707.07134](https://arxiv.org/abs/1707.07134)

Pancoast, A., Brewer, B. J., & Treu, T. 2011, *ApJ*, 730, 139

Parker, E. N. 1953, *ApJ*, 117, 431

Perez, E., Robinson, A., & de La Fuente, L. 1992, *MNRAS*, 256, 103

Peterson, B. M. 1993, *PASP*, 105, 247

Peterson, B. M., *An introduction to active galactic nuclei*, Cambridge, NY: Cambridge University Press, 1997

Poisson, E., & Will, C. M., *Gravity*, Cambridge, UK: Cambridge University Press, 2014,

Proga, D., Stone, J. M., & Drew, J. E. 1998, *MNRAS*, 295, 595

Proga, D., Stone, J. M., & Kallman, T. R. 2000, *ApJ*, 543, 686

Proga, D., & Kallman, T. R. 2004, *ApJ*, 616, 688

Proga, D. 2007, *ApJ*, 661, 693

Proga, D., Ostriker, J. P., & Kurosawa, R. 2008, *ApJ*, 676, 101-112

Proga, D., Jiang, Y.-F., Davis, S. W., Stone, J. M., & Smith, D. 2014, *ApJ*, 780, 51

Proga, D., & Waters, T. 2015, *ApJ*, 804, 137

Ramirez-Velasquez, J. M., Klapp, J., Gabbasov, R., Cruz, F., & Sigalotti, L. D. G. 2016, [arXiv:1607.07785](https://arxiv.org/abs/1607.07785)

Rees, M. J., Netzer, H., & Ferland, G. J. 1989, *ApJ*, 347, 640

Reeves, J. N., O’Brien, P. T., Braitto, V., et al. 2009, *ApJ*, 701, 493

Rezzolla, L., & Zanotti, O., *Relativistic Hydrodynamics*, Oxford University Press, 2013

Richards, G. T., Myers, A. D., Gray, A. G., et al. 2009, ApJS, 180, 67

Rybicki, G. B., & Hummer, D. G. 1978, ApJ, 219, 654

Rybicki, G. B., & Hummer, D. G. 1983, ApJ, 274, 380 (RH83)

Salz, M., Banerjee, R., Mignone, A., et al. 2015, A&A, 576, A21

Schurch, N. J., Done, C., & Proga, D. 2009, ApJ, 694, 1

Shin, M.-S., Stone, J. M., & Snyder, G. F. 2008, ApJ, 680, 336-348

Shields, J. C., Ferland, G. J., & Peterson, B. M. 1995, ApJ, 441, 507

Shu, F. H., Milione, V., Gebel, W., et al. 1972, ApJ, 173, 557

Shu, F., Physics of Astrophysics Vol II: Gas Dynamics, New York, NY: University Science Books, 1991

Sim, S. A., Proga, D., Miller, L., Long, K. S., & Turner, T. J. 2010, MNRAS, 408, 1396

Skjelboe, A., Pancoast, A., Treu, T., et al. 2015, MNRAS, 454, 144

Smith, R. K., Ackermann, M., Allured, R., et al. 2016, Proc. SPIE, to appear

Snedden, S. A., & Gaskell, C. M. 2007, ApJ, 669, 126

Sparke, L. S. 1993, ApJ, 404, 570

Spitzer, L. 1962, Physics of Fully Ionized Gases, (NY: Interscience, 2nd edition)

Stevens, I. R., & Kallman, T. R. 1990, ApJ, 365, 321

Stone, J. M., Gardiner, T. A., Teuben, P., Hawley, J. F., & Simon, J. B. 2008, ApJS, 178, 137

Sulentic, J. W., Marziani, P., & Dultzin-Hacyan, D. 2000, ARA&A, 38, 521

Tarter, C. B., & McKee, C. F. 1973, ApJ, 186, L63

Toro, E. F., Riemann Solvers and Numerical Methods for Fluid Dynamics, Springer 2009

Turner, T. J., & Miller, L. 2009, A&ARv, 17, 47

Urry, C. M., & Padovani, P. 1995, PASP, 107, 803

Uttley, P., & Casella, P. 2014, Space Sci. Rev., 183, 453

Wang, J.-M., Du, P., Baldwin, J. A., et al. 2012, ApJ, 746, 137

Wang, T., Yang, C., Wang, H., & Ferland, G. 2015, ApJ, 814, 150

Waters, T., Kashi, A., Proga, D., et al. 2016, ApJ, 827, 53

Waters, T., & Proga, D. 2016, MNRAS, 460, L79

Waters, T., Proga, D., Dannen, R., & Kallman, T. R. 2017, MNRAS, 467, 3160

Welsh, W. F., & Horne, K. 1991, ApJ, 379, 586

Weymann, R. 1976, ApJ, 208, 286

Wildy, C., Landt, H., Goad, M. R., Ward, M., & Collinson, J. S. 2016, MNRAS, 461, 2085

Williams, R. E. 1972, ApJ, 178, 105

Wolfe, A. M. 1974, ApJ, 188, 243

Zanstra, H. 1955, Vistas in Astronomy, 1, 256

Zeldovich, Y. B., & Raizer, Y. P., New York: Academic Press, 1966, edited by Hayes, W.D.;
Probstein, Ronald F.

Zhang, D., & Davis, S. W. 2017, ApJ, 839, 54

Zheng, W., Kriss, G. A., Telfer, R. C., Grimes, J. P., & Davidsen, A. F. 1997, ApJ, 475, 469

Zu, Y., Kochanek, C. S., & Peterson, B. M. 2011, ApJ, 735, 80

CURRICULUM VITAE

NAME: Tim Waters

EMAIL: waters@lanl.gov

EDUCATION SUMMARY:

08/2013-08/2017: PhD, Physics, University of Nevada Las Vegas (UNLV), advisor: Daniel Proga

Thesis: The formation and dynamics of clouds in the environment of active galactic nuclei

08/2009-05/2012: MS, Physics, UNLV

Thesis: Parker winds revisited: an extension to disk winds

08/2007-05/2009: MS, Applied Mathematics, UNLV

08/2002-05/2006: BA, Physics, Occidental College, Los Angeles, CA

EXPERIENCE IN SCIENTIFIC COMPUTING:

Preferred languages: Python, C++, C

Scientific codes: Athena, Athena++, XSTAR

Visualization software: VisIt, yt, Glue

Developer tools: bash scripting, git, f2py

HPC clusters: UNLV's Cherry Creek (extensive usage), TACC Stampede, LANL's Wolf

WORK EXPERIENCE:

06/2017 – Present: **Student**, Los Alamos National Laboratory

- Working on relativistic magnetohydrodynamical (GRMHD) simulations under Josh Dolence in CCS-2

06/2013 – 08/2017: **PhD Candidate**, Physics Department, University of Nevada Las Vegas

- Returned to UNLV to finish my PhD under Daniel Proga
- Successfully defended dissertation 08/2017

06/2015 – 08/2015: **Summer student**, Los Alamos National Laboratory

- Undertook a research project on supernovae under Wes Even in Chris Fryer's group

07/2014 – 08/2014: **Summer student**, Los Alamos National Laboratory

- Worked on a research project in plasma physics (under Sean Fu and Misa Cowee) as part of a 5 week "Space Weather Summer School" in ISR division

06/2012 – 05/2013: **Math Developer**, Gaming Laboratories International, Las Vegas, NV

- Wrote Monte Carlo programs to simulate game play and certify slot machine game statistics.

01/2012 – 06/2012: **Intern Engineer**, Telesecurity Sciences, Las Vegas, NV

- Developed threat detection algorithms for large-scale X-ray devices used for scanning cargo shipment containers.

08/2009 – 05/2012: **Graduate Assistant**, Physics Department, University of Nevada, Las Vegas

- PhD student working with Professor Daniel Proga.
- Lab instructor: taught intro physics labs.

08/2007 – 05/2009: **Graduate Assistant**, Math Department, University of Nevada, Las Vegas

- Course instructor: taught many first year math courses.

HONORS & AWARDS:

Fellowship Recipient, Los Alamos Space Weather Summer School, Summer 2014

Nevada NASA Space Grant Consortium Fellowship, Spring – Fall 2011

Inducted to Sigma Pi Sigma Physics Honor Society, Spring 2006

President's Scholarship, Occidental College, Fall 2002 - Spring 2006

SERVICE & OUTREACH:

Mentor to an undergraduate student, UNLV Research And Mentoring Program (RAMP), Fall 2016 – Spring 2017

Built the current UNLV Physics & Astronomy Dept. website, Spring 2015

Organizer for the UNLV Astronomy weekly Journal Club, Fall 2013–Spring 2014

Secretary/Treasurer, Southern Nevada American Association of Physics Teachers (AAPPT) Section, Spring 2011–2012

2010 NASA Student Ambassador

PROFESSIONAL SERVICE:

Referee for both The Astrophysical Journal (ApJ) and Monthly Notices of the Royal Astronomical Society (MNRAS).

PUBLICATIONS:

Journal Articles

1. Waters, Proga, Dannen, & Kallman, Synthetic Absorption Lines for a Clumpy Medium: a spectral signature for cloud acceleration in AGN?, MNRAS (in press), arxiv:1611.00407
2. Dyda, Dannen, Waters, & Proga, Irradiation of Astrophysical Objects: efficiency of thermally driven winds on SED and flux, submitted to MNRAS, arxiv: 1610.04292
3. Waters & Proga, On the Efficient Acceleration of Clouds in Active Galactic Nuclei, MNRAS Letters, 460, L79, 2016
4. Waters, Proga, Kashi, Eracleous, Barth, & Greene, Reverberation Mapping of the Broad Line Region: Application to a Hydrodynamical Line Driven Disk Wind Solution, ApJ, 827, 53, 2016
5. Proga & Waters, Cloud Formation and Acceleration in a Radiative Environment, 2015, ApJ, 804, 137
6. Waters & Proga, Parker Winds Revisited: An Extension to Disk Winds, 2012, MNRAS, 426, 2239

Non-Peer Reviewed

1. Waters & Fu, An accurate scheme to evaluate the linear dispersion relation for magnetized plasmas with arbitrary parallel distribution functions, 2014 Los Alamos Space Weather Summer School Research Reports, LANL, 2014.

Conference Proceedings

1. Waters & Proga, 2012, Parker winds revisited: an extension to disk winds, AGN Winds in Charleston, 460, 229

PRESENTATIONS:

1. "Properties, Dynamics, and Spectral Signatures of Clouds in AGN", Invited talk, AGN Winds on the Georgia Coast, Jekyll Island, GA, Summer 2017
2. "Calculation of echo images from 1st principles: self-consistently combining photoionization modeling and astrophysical fluid dynamical simulations", Invited talk, Reverberation Mapping workshop, Lijiang, China, October 2016
3. "Local cloud simulations: gas dynamics in the AGN environment", Talk given to Jim Stone's Athena group meeting, Princeton, NJ, October 2015
4. "On Solving the Hot Plasma Dispersion Function given an arbitrary Velocity Distribution", Los Alamos Space Weather Summer School Final Presentation, LANL, Summer 2014
5. "Our galaxy's supermassive black hole", Invited Talk, Chapter Meeting of Southern Nevada AAPT, UNLV Campus, Fall 2014
6. "Flowtube Dynamics with Athena", Lunch Talk, KIAA-Peking University, Winter 2013
7. "Parker Winds Revisited: An Extension to Disk Winds", MS Thesis Defense, UNLV, April 2011

CONFERENCES, WORKSHOPS, & SUMMER SCHOOLS ATTENDED:

1. [Talk] AGN Winds on the Georgia Coast, Jekyll Island, GA, Summer 2017
2. [Talk] AGN Reverberation Mapping: the pc scale garden of massive black holes, Lijiang, China, October 2016
3. PiTP 2016: Computational Plasma Astrophysics Summer School, Institute for Advanced Study, Princeton, NJ, July 2016
4. [Poster] Great Lakes Quasar Symposium, London, Ontario, May 2016
5. [Poster] JSI Workshop: the physics of supermassive black hole formation and feedback, Annapolis, MD, October 2015
6. [Poster] Exploring the Hot and Energetic Universe: The first scientific conference dedicated to the Athena X-ray observatory, ESAC, Madrid, Spain, September 2015
7. 4th Los Alamos Space Weather Summer School, LANL, June – July 2014
8. [Poster] AGN Winds in Charleston, Charleston, SC, Fall 2011
9. [Poster] Understanding Relativistic Jets, Krakow, Poland, Summer 2011
10. [Poster] Accretion Processes in X-Rays, Boston, MA, Summer 2010
11. 4th Gravitational Wave Summer School, South Padre Island, TX, Summer 2007